

Polymer Integrated Optics: Device Architectures and Fabrication Methods

Thesis by
George T. Paloczi

In Partial Fulfillment of the Requirements
for the Degree of
Doctor of Philosophy



California Institute of Technology
Pasadena, California

2005

(Defended April 27, 2005)

© 2005

George T. Paloczi

All Rights Reserved

Acknowledgements

Many successes during my long journey at Caltech are due in large part to others – those without whose support my accomplishments would not be possible.

First, I would like to thank my advisor, Professor Amnon Yariv, for providing an open environment, enabling me to learn each aspect of research and to grow through independent research. An irreplaceable fixture in our group every summer, Professor Bruno Crosignani was an important model of one who has a true zeal for the physical fundamentals of optics. Ali Ghaffari provided exceptional training on a wide variety of laboratory apparatus, and plentiful laughter when it was especially needed. Connie Rodriguez, beyond organizing practically everything for our group, was always happy to give out a snack with a bit of gossip. Irene Loera could be counted on daily for a morning smile and, as a one-person purchasing department, made our work much easier.

The post-docs and older students were valuable mentors and collaborators. Dr. Reg Lee was a source of advice and helpful suggestions from the beginning, and served as one of my first examples of a fine engineer. My first office-mates, Dr. Dan Provenzano and Dr. Roger Koumans, maintained in me a well-rounded perspective and provided immediate friendship and support. My first collaborator, Professor Avishay Eyal, exhibited a natural curiosity and passion for answers that compelled me to follow his example. Dr. Koby Scheuer showed me what it meant to have a full and deep understanding of each problem one works on. Dr. Yanyi Huang, my foremost collaborator in graduate school, displayed an energy and dedication worthy of emulation.

My fellow students were instrumental in my work at Caltech and, as brethren, we helped each other in maintaining sanity throughout the journey. John Choi displayed an extraordinary strength of character, and commendably maintained his ideals about scientific research throughout. Will Green's attention to experimental detail and thoroughness were my envy, and his fabrication skills were the best I had seen. Professor Shayan Mookherjea, whose scientific vigor and com-

mitment inspired me, was able to decipher my cryptic, disconnected jokes. Joyce Poon always provided a balanced view in fleshing out the truth, and she reminded everyone of coolness and calm in moments of agitation.

Friends, I will always cherish our many coffee breaks, lunch-time discussions, and good times together.

Most importantly, I would like to extend the deepest possible gratitude to my family. My brothers, sisters, and parents, both by blood and by marriage, provided many times of fun and peace apart from graduate school, along with plenty of patience and advice. My mother especially encouraged me during the low points and compelled me to be strong and unwavering. Finally, I thank my immeasurably patient wife, Christie, for being counselor, friend, booster, critic, confidant, base of reality, source of joy, and much more.

Polymer Integrated Optics: Device Architectures and Fabrication Methods

by

George T. Paloczi

In Partial Fulfillment of the
Requirements for the Degree of
Doctor of Philosophy

Abstract

Polymer materials are becoming increasingly important for integrated photonic circuits in optical communications networks. The optical and mechanical properties of polymers for integrated optics are explored in this thesis and it is shown that the manipulation of these properties leads to developments that in other optical materials could not be achieved as quickly or as easily, or not achieved at all.

So that the benefits of a large range of operating wavelengths due to low material dispersion in polymers, are not lost to the wavelength dependence of optical couplers, we design wavelength-invariant couplers using a geometrical representation of coupled mode theory. Simulations of the resulting couplers confirm a virtually constant response over a large range of input wavelengths.

The direct-write ability of electron beam sensitive polymers enables rapid fabrication of high-precision optical devices. Microring resonator optical filters and a compact microring-based inline reflector are fabricated by this method and characterized. Chaining multiple rings together results in the coupled resonator optical waveguide (CROW). A CROW-Mach-Zehnder interferometer is fabricated and the measured response corresponds well with the predictions based on the matrix theory.

Polymer materials can be patterned by a variety of methods not possible with traditional optical materials. Soft-stamp replica molding presents a means to fur-

ther reduce the costs of implementing polymer materials. Demonstrating the potential of the method, microring resonators are fabricated, with excellent agreement between the responses of the original and the replica. To further demonstrate the effectiveness of the process, it is applied in the fabrication of Mach-Zehnder modulators. The modulators exhibit excellent properties, with single-arm modulation voltages of 8 V and extinction ratios better than 19 dB. Successive repetition of the molding process allows for multilayer polymer optical devices. Finally, the flexible properties of polymers are exploited for pliable, all-polymer freestanding optical circuits.

Contents

1	Introduction	1
1.1	Background and Motivation	1
1.2	Thesis Outline	3
2	Coupled Mode Theory and Its Geometrical Representation	6
2.1	Introduction	6
2.2	Fundamental Theory of Optical Waveguides	7
2.2.1	The Wave Equation and Plane Waves	7
2.2.2	The Slab Waveguide	8
2.2.3	The Effective Index Method	11
2.3	Coupled Mode Theory	14
2.4	The Geometrical Representation of Coupled Mode Theory	18
2.5	Symmetric and Mode Evolution Optical Couplers	21
2.5.1	Symmetric Optical Couplers	21
2.5.2	Adiabatic Mode Evolution Optical Couplers	23
2.5.3	Non-Adiabatic Mode Evolution Optical Couplers	24
2.5.4	Coupler Index Profiles and Simulations	26
2.6	Wavelength-Invariant and Fabrication Error Tolerant Optical Couplers	28
3	Polymer Microring Resonator Optical Filters	35
3.1	Introduction	35
3.2	Fundamental Theory of Microring Resonators	36

3.2.1	The Spectral Response and Related Quantities	36
3.2.2	Radiation Loss in Bent Waveguides	43
3.2.3	Waveguide Surface Scattering Loss	46
3.3	Passive Polymer Planar Optics Using SU-8	48
3.4	Polymer Microring Resonators	53
3.5	Freestanding All-Polymer Optical Devices	56
3.5.1	Fabrication	57
3.5.2	Measurement Results and Discussion	61
3.5.3	Potential Applications of Freestanding All-Polymer Optical Circuits	66
3.6	Microring Resonator Based Reflector	68
3.6.1	Theory	69
3.6.2	Demonstration	71
3.6.3	Discussion	71
4	Coupled Resonator Optical Waveguides	75
4.1	Introduction	75
4.2	Fundamental Theory of Coupled Resonator Optical Waveguides . .	77
4.2.1	Tight Binding Model	77
4.2.2	Matrix Method for CROW Analysis	80
4.3	CROW Mach-Zehnder Interferometer	82
4.3.1	Fabrication and Measurement	83
4.3.2	Results and Discussion	85
4.4	Potential Applications of Polymer CROWs	88
5	Soft-Stamp Replica Molded Polymer Integrated Optical Devices	91
5.1	Introduction	91
5.2	Soft-Stamp Replica Molding	92
5.2.1	The Technique	92
5.2.2	The Background Residue	95
5.3	Polymer Microring Resonators Fabricated by Replica Molding . . .	106

5.3.1	Fabrication and Measurement	107
5.3.2	Results and Discussion	110
5.4	Multilayer Molding	111
5.4.1	Fabrication and Measurement	112
5.4.2	Results and Discussion	117
6	Electro-Optic Polymer Mach-Zehnder Modulators	118
6.1	Introduction	118
6.2	Electro-Optic Polymers	119
6.2.1	Poling of Guest-Host Electro-Optic Polymers	121
6.3	Prototype Polymer Electro-Optic Modulator Fabricated by Soft-Stamp Replica Molding Using the CLD-1 Chromophore	125
6.3.1	Fabrication and Measurement	125
6.3.2	Results and Discussion	127
6.4	Low-Voltage Polymer Electro-Optic Modulator Fabricated by Soft-Stamp Replica Molding Using AJL8 Chromophore	128
6.4.1	Fabrication and Measurement	128
6.4.2	Results and Discussion	133
7	Conclusions	135
7.1	Synopsis	135
7.2	Outlook	139
A	Beam Propagation Method	142
A.1	Conceptual Underpinnings	142
A.2	Practical Application	145
B	Finite Difference Mode Solver	147
B.1	Conceptual Underpinnings	147
B.2	Practical Application	148
C	List of Publications	152

List of Figures

2.1	The slab waveguide structure. The waveguide core with index n_1 and thickness t is surrounded by the upper cladding with index n_3 and lower cladding with index n_2	9
2.2	A schematic of the field distribution of the lowest order TE mode of the slab waveguide structure described in Figure 2.1.	10
2.3	Cross sections of three typical waveguide geometries: (a) the raised strip, (b) the buried channel, and (c) the rib guide.	11
2.4	Illustration of the effective index method. The upper drawing shows the actual rib waveguide cross section and the lower drawing shows the reduced slab waveguide structure.	12
2.5	Illustration of the refractive index terms used in coupled mode theory calculations. The spatial integration in $\kappa_{12,21}$ are only over the areas shown in the bottom two drawings.	16
2.6	The Poincaré sphere base states. A state vector \mathbf{s} on any of the axes represents the two-waveguide state as shown. The numbers represent the relative amplitudes and phases in each waveguide for the corresponding base states.	20
2.7	Geometrical representation of a 3-dB stationary mode coupler. The rotation vector, $\mathbf{\Omega}$, (filled circle) remains statically collinear with the s_2 axis, while the magnitude of the rotation vector dictates the rotation of the state vector, \mathbf{s} , (unfilled circles) from the s_1 -axis to the s_2 -axis.	22

- 2.8 Geometrical representation of a 3-dB adiabatic mode evolution coupler. The rotation vector (filled circles) itself rotates from the s_1 -axis, corresponding to the individual waveguide modes, to the s_2 -axis, representing modes of equal amplitude and phase. The magnitude of the rotation vector is large so that the state vector (unfilled circles) closely follows the trajectory of the rotation vector. 24
- 2.9 Geometrical representation of a 3-dB non-adiabatic mode evolution coupler. The rotation vector (filled circles) rotates from the s_1 -axis to the s_2 -axis and back. However, the magnitude of the rotation vector is smaller than in the adiabatic case (Figure 2.8), so that the state vector (unfilled circles) cannot closely follow the rotation vector. In this way, the state vector is transported from its initial state on the s_1 -axis to the meridian representing equal amplitude. 25
- 2.10 Refractive index profiles for the three types of couplers described above. In (a) the symmetric directional coupler, in (b) the adiabatic coupler, and in (c) the non-adiabatic mode evolution coupler. 27
- 2.11 Beam propagation simulations for the three refractive index profiles shown in Figure 2.10. In each case, light is input into one waveguide and the resultant output is that of equal power between the two waveguide outputs. In (a) the symmetric directional coupler, in (b) the adiabatic coupler, and in (c) the non-adiabatic mode evolution coupler. 28
- 2.12 Power output ratio as a function of $|\Omega|$ for the raised cosine shape function. Points A, B, and C represent couplers with the desired 3-dB power output ratio. 29

2.13	Geometrical representation of the eigenstate (o) and system state (×) trajectories. The system states begin occupying one eigenmode, that is, light is injected into waveguide 1, and end in the eigenmode given by equal output power and phase. Figures 2.13 (a), (b), and (c) depict trajectories as calculated for $ \mathbf{\Omega} $ given by points A, B, and C, respectively, for Figure 2.12. In (d) we show the coincident system state and eigenstate trajectories of a long-length adiabatic coupler for comparison.	31
2.14	Power output ratios and relative output phases as a function of wavelength (a,b) and width scaling factor (c,d). The dash-dot (- · -) line represents a symmetric directional coupler for comparison. The dashed (- - -) and solid (—) lines give the output ratios and relative phases corresponding to couplers designed with $ \mathbf{\Omega} $ as given by points (a) and (b) in Figure 2.12, respectively.	32
3.1	Microring resonators side coupled to one waveguide in (a), and side coupled to two waveguides in (b).	36
3.2	The output power of a single ring resonator coupled to a waveguide. Each plot shows the spectra with $t = 0.1, 0.3, 0.5, 0.7$ and 0.9 . The upper, middle, and lower plots represent spectra with $\alpha = 0.3, 0.5$ and 0.7 , respectively.	39
3.3	A curved waveguide section with the first order mode illustrated. The radiated field is on the constant phase line beyond the radiation caustic.	43
3.4	Slab waveguide refractive index profile $n(x)$ and corresponding equivalent refractive index profile $n_{equ}(x)$	44
3.5	Typical “elbow” curves of bend loss for several cladding refractive indexes ($n_{clad}=1.45, 1.50, 1.53$) and fixed core index ($n_{core}=1.60$).	46
3.6	The chemical structure of the SU-8 molecule showing the eight epoxy groups.	48

3.7	Scanning electron microscope images of SU-8 waveguides fabricated by direct electron beam exposure of the core.	51
3.8	A waveguide grating fabricated by direct electron beam exposure of SU-8.	52
3.9	An early example of a microring resonator optical filter fabricated in SU-8 by direct electron beam writing.	54
3.10	The measured output spectrum for the microring resonator depicted in Figure 3.9.	56
3.11	Schematic fabrication procedure for freestanding polymer integrated optical devices. For clarity, the thicknesses are not drawn in proportion to the real device.	58
3.12	Preparation of freestanding all-polymer optical device end-facets using scalpel blades.	59
3.13	Optical microscopic images of polymeric model structures. All structures are made with SU-8 core layers on UV15 lower cladding using electron beam lithography. (a) Microring with 200 μm diameter. (b) Microdisk with 200 μm diameter with 2 μm wide waveguides. (c) Freestanding all-polymer film with a microring array, illuminated with a HeNe laser. The bright wedge is the fine tip of the tweezers used to hold the film. (d) Curved freestanding polymer film with microring array (5 by 5) and microdisk array (3 by 3). (e) and (f) All-polymer microring array on curved surface. The structures are peeled off of the substrate and reattached on a glass capillary tube (2 mm diameter) by heating.	60

- 3.14 Freestanding all-polymer microring resonator optical filter. (a) Schematic diagram of a microring resonator optical filter. (b) SEM image of freestanding microring resonator optical filter, purposely curled to show the excellent flexibility. (c) SEM image of a waveguide (SU-8) and lower cladding layer (UV15). The end-facet of device is prepared by scalpel blade cutting method. (d) Polymer microring resonator optical filters on a curved surface. The devices are peeled off of the substrate and heated to adhere to small glass capillary tube (0.8 mm diameter). 62
- 3.15 Schematic diagram of measurement setup for the microring resonator optical filter. TE-polarized laser light is coupled into the input end of polymer device via a tapered fiber, and the output optical signal was collected by an IR-CCD camera or IR photodetector (PD). The two IR-CCD images of the output light are at different wavelengths, with the arrows indicating the position of the output end of the device. In (a), the wavelength of the light is off-resonance for the microring and in (b), on-resonance. 64
- 3.16 Spectral transfer function of a freestanding air-clad critically coupled microring resonator optical filter. The open square is experimental data and the line is theoretical calculation. The inset is a higher resolution measurement (open circle) around 1550 nm and theoretical calculation (line). 65
- 3.17 The integration of freestanding all-polymer waveguide devices with CMOS drive or trimming circuitry. 66
- 3.18 The creation of a three-dimensional densely integrated optical waveguide circuit by stacking several freestanding all-polymer waveguide devices. 67

3.19	A scanning electron microscope perspective image of a device similar to that measured here. The input, reflected, and transmitted signals are labeled i, r and t , respectively. Two sets of fields, a, b, c and the corresponding primes, obey Equations 3.34 and 3.35.	69
3.20	Normalized transmission (upper) and reflection (lower) signals for the microring-based inline reflector. For the calculation, the microring radius is 108.25 microns, the effective refractive index is 1.515, t is 0.85, and the loss parameter α is taken to be 1.	70
3.21	Measurement results showing the normalized transmission (upper) and reflection (lower) signals. The extinction ratios for the nulls in the transmission signal are better than 10 dB.	72
3.22	In (a): a reflector employing three microring resonators to exhibit a special spectral response (e.g., a wavelength-flattened reflection band). In (b): a reflector employing the Vernier effect with resonators of different radii.	73
4.1	Three types of waveguiding structures. In (a), a conventional dielectric waveguide using total internal reflection for confinement. In (b), light is guided by Bragg reflection at the waveguide boundaries. In (c), light propagates by coupling from each resonator to the subsequent resonator.	76
4.2	Left: Dispersion diagram showing plots of (4.7) with $\kappa = 0.1$ and 0.2 . The frequency ω_K is normalized to Ω . The wave vector is represented on the horizontal axis as KR/π . Right: Group velocity as a function of normalized wave vector for $\kappa = 0.1$ and 0.2	79
4.3	Coupled resonator optical waveguide with N rings (N odd for the output direction as shown). The arrows signify the direction of light propagation. The matrix \mathbf{P} represents the coupling segments and \mathbf{Q} accounts for the phase and loss accumulated in the resonators.	80

4.4	Schematic diagram of a CROW-MZI with one arm as a ridge waveguide of length L , with propagation constant β , and the other arm consisting of coupled microresonators, spaced by a distance d , with propagation constant β_{CROW} . Y-branches divide and add the optical field equally between the two arms. Adiabatic tapers act as impedance matched terminations after the field couples to the first resonator, ensuring no back reflected fields.	83
4.5	Optical microscope image of the CROW-MZI showing a total device width of approximately 1.2 mm. The identical racetrack microresonators had 50 micron straight coupling sections and 100 micron bend radii in the curved sections.	84
4.6	Normalized measured output power of the polymer CROW-MZI ranging over a spectral bandwidth of 50 nanometers, approximately 22 single resonator free spectral ranges.	85
4.7	Experimental data (thin line with filled circles) and the theoretical fit (solid thick line) based on (4.18). The fitting parameters used for the fit were: polarization 93% TE and 7% TM, effective indices 1.48475 for TE and 1.48555 for TM, power coupling coefficients 0.46 for TE and 0.85 for TM, and waveguide loss of 30 dB/cm.	87
4.8	An example of a CROW delay line consisting of 27 microring resonators, each with radius 50 μm and separated by 200 nm, fabricated in SU-8 by direct electron-beam exposure.	89

5.1	Schematic diagram of the replica molding process for polymer waveguide devices. (a) The master device is fabricated in SU-8 resist by ultraviolet or electron beam exposure. (b) PDMS is poured atop the master device and thermally cured. (c) Once cured, the PDMS mold is peeled from the master device. (d) A drop of the core polymer solution is placed on an appropriate substrate. (e) The PDMS mold is depressed. (f) Once cured, the PDMS mold is peeled to expose the molded replica.	94
5.2	Photograph of the molding setup.	95
5.3	Molding of polymer waveguide structures directly on electrical circuitry.	96
5.4	Scanning electron microscope image of a molded waveguide, and the surrounding residue, overhanging a cleaved silicon substrate.	97
5.5	Effective indices of the first, second and third order mode as a function of residue thickness.	98
5.6	Output ratio of a directional coupler as a function of residue thickness.	99
5.7	Bend loss as a function of residue thickness.	100
5.8	Waveguide and residue thickness for various solution concentrations.	102
5.9	Waveguide and residue thickness for various forces applied to the mold.	103
5.10	Formation of background residue. In (a) the PDMS mold and polymer solution before molding. In (b) the mold is pressed atop the solution/substrate, forming the waveguide structures, but leaving a polymer residue layer surrounding the waveguides. In (c), optical microscope image showing a waveguide (black) surrounded by thin residue (white) that gets thicker farther from the waveguide (gray). The measured thicknesses correspond to the gray areas, the areas of thickest residue.	105

5.11	Schematic diagram of fabrication processes. Generally, the ultraviolet curable polymer can be either the same material used for electron beam lithography or different ones.	107
5.12	Optical setup for transmission measurement.	108
5.13	Optical microscope image of microring optical resonator fabricated by soft lithography. The inset shows the detail of coupling region. The ring diameter is designed to be 200 μm and the waveguide width is 2 μm . Light from a He-Ne laser is input into the device for illustration only.	109
5.14	Schematic geometry for waveguide ring resonator coupling. The color plot is a finite-difference time-domain simulation of the coupling between the straight waveguide and the ring.	109
5.15	Comparison of transmission spectra of the master (blue) to molded (red) ring resonator.	111
5.16	Schematic flowchart of the fabrication of 3D integrated optical microchips.	112
5.17	Optical microscope images of multilayer devices. A three-layer microchip and its schematic structure are shown in (a). Each layer consists of a different polymer material. A two-layer microchip containing a microring resonator optical filter in each layer is shown in (b). (c) and (d) are infrared camera images of the outputs of the microring resonator filters in the upper layer (input/output 1) and in the lower layer (input/output 2), respectively. The squares in (c) and (d) are the positions of the end facets of the other output. . .	114
5.18	Transmission spectra of the microring resonator optical filters in the two layers of the microchip, as shown in Figure 5.17(b). The experimental data are shown as solid circles (lower layer) and solid squares (upper layer). The solid line and dashed line are the fitting curves of experimental data of the upper layer and the lower layer, respectively. The inset shows detailed spectra around 1550 nm. . .	116

6.1	The chemical structure of AJL8 chromophore.	120
6.2	Schematic diagram of the corona poling method for alignment of the chromophores in guest-host electro-optic polymers.	122
6.3	The corona current versus the tip-to-sample voltage in both nitrogen and ambient environments, with and without the sample present.	124
6.4	The structure of the polymeric Mach-Zehnder interferometer modulator: (a) Top view, (b) Side view.	126
6.5	Halfwave voltage measurement from a 2 mm soft lithographic Mach-Zehnder interferometer modulator device.	127
6.6	Fabrication of the PDMS stamp. A master MZI device (a) is patterned by photolithography of SU-8. PDMS is poured on the master device (b), cured, peeled, and diced (c).	129
6.7	Procedure for making the replica from the mold. A drop of electro-optic core solution is placed on the appropriate substrate (a). The PDMS stamp is depressed (b) until the core polymer is cured. The stamp is peeled to reveal the high-fidelity replicated device (c).	129
6.8	Cross sectional view of the electro-optic waveguide structure. The core electro-optic polymer is AJL8/APC and the upper and lower cladding materials are low refractive index epoxy WR-513.	131
6.9	Measured modulator output as a function of applied voltage. An applied voltage of $V_{\pi}=8.4$ V renders the input 1600 nm light null.	132
A.1	3-dimensional BPM simulation of a straight waveguide side-coupled to a microring resonator.	146
B.1	Outline of waveguide cross-section, with power contours of the first order mode as calculated for a quasi-TE mode using the semivectorial finite difference method.	151

Chapter 1

Introduction

1.1 Background and Motivation

Devices used in high speed optical communications networks comprise a wide array of material systems [1]. Among the key material systems are silica (both fiber and silica-on-silicon), silicon oxynitride, sol-gel, dielectric thin film, lithium niobate, gallium arsenide, indium phosphide, magneto-optic materials, birefringent crystals, and polymer. Such a wide array of material systems is necessary because of the unique requirements of the constituent passive or active componentry [2]. Passive devices in integrated optics include simple waveguides, arrayed waveguide gratings, Bragg gratings, thin film filters, and microring resonator filters. Important active integrated optical devices include modulators (using electro-optic, acousto-optic, or electro-absorption effects), amplifiers (using heterostructures, quantum wells, or rare-earth doping), and switches (using electro-optic, thermo-optic, electro-absorption, or micro-electro-mechanical means). These building-block passive and active components are fundamental in higher-function devices such as optical add/drop multiplexers, interleavers, routers, variable optical attenuators, gain flattening filters, sources, receivers, and detectors.

While semiconductor and other inorganic materials have been extensively investigated and developed during the past decades to meet the demands of high-speed optical communications and large-scale integrated optical circuits [3], the stringent

requirements of next-generation optical communications networks are pushing the limits of conventional materials. As a new material available for optical integrated optics, polymer materials remain among the lesser studied and developed materials despite having properties amenable to future requirements. Recently, however, more attention has been given to polymeric materials for use in integrated optical devices because of several advantageous features [4]. These features, and manipulation of these features to accomplish feats impossible or not easily achieved with traditional inorganic materials, are the subject of this thesis.

With several important recent advances, polymers are fast becoming important materials for optoelectronics. Significant examples include mechanically flexible “electronic paper” [5] and high efficiency light-emitting diodes based on electroluminescent conjugated polymers [6]. Similar promise is being presented for polymers in telecommunications-related integrated optical devices due to several favorable material features [7]. For instance, as required by the application, polymer materials can be made functional in several ways. Otherwise passive polymers that are not intrinsically functional can be doped with numerous optically active dopants such as organic laser dyes [8], rare-earth light-amplifying complexes [9], or electro-optic chromophores [10]. The “soft” nature of the materials differs from crystalline materials, enabling, for example, flexible free-standing electro-optic modulators [11]. Perhaps most significantly, the low material costs are the motivation towards mass production of polymer optoelectronic devices. In contrast to semiconductor materials that require several successive growths with complicated equipment to make the raw material, polymer waveguide and cladding layers are simply sequentially spun-cast onto a rigid substrate. Thus far, the fabrication techniques for polymeric integrated optical devices have been mostly limited to standard semiconductor fabrication techniques such as ultraviolet photo-, electron beam, or interference lithography, reactive ion etching, and/or wet etching. Novel fabrication techniques that reduce both the cost and time required for fabricating integrated optical components must be employed to fully take advantage of the low material costs and distinctive intrinsic properties of polymers.

A major effort in the recent development of polymers for communications-based integrated optics has been related to their use for electro-optic modulators. Since passive polymers can be doped with chromophore molecules chemically engineered to have very high nonlinearities, the likelihood of low switching voltage Mach-Zehnder modulators has served as the impetus for much of the work. Toward this end, modulators with switching voltages of less than 1 V have been demonstrated [12]. Further, using the exceptional material bandwidth of polymer, polymer modulators have been demonstrated with modulation rates far beyond what traditional materials are capable of, as high as 1.6 THz [13]. With respect to passive polymers for integrated optics, the development has been limited mostly to simple waveguide structures, such as couplers, interconnects or Bragg wavelength filters, with few examples of complex passive optical structures demonstrated in polymer [4, 7].

In my research, the undertaking was to develop and characterize integrated optical devices, specifically fabricated of polymer materials. There was no infrastructure in polymer devices, nor specific experience to enable competing with other research groups as far as electro-optic polymer modulator switching voltage or bandwidth were concerned. Both for passive and active polymer devices, I could not afford to simply improve upon what was previously demonstrated, as the engineering would have been far too time consuming and comparatively fruitless. Instead, the motivation was to creatively make use of the material properties of polymer – distinct from those of traditional integrated optical materials – in applying polymers to integrated optical devices. The goal was to determine truly what differentiated polymer materials from common inorganic optical materials, and to exploit these properties in new ways for integrated optics.

1.2 Thesis Outline

In Chapter 2, the theory of optical waveguides and couplers upon which much of this thesis relies is established. Based on the theory of optical couplers, a geomet-

rical representation is presented, with an emphasis on the design of new types of couplers. Espousing this geometrical representation, a new class of coupler – the non-adiabatic mode evolution coupler – is developed and characterized through optical simulations [14]. The results of the simulations clearly demonstrate that these couplers have a wide operating bandwidth and a high degree of tolerance to fabrication error.

Chapter 3 deals with aspects of microring resonators in polymer integrated optics. The basic theory of microring resonators is put forth, as well as the theories of waveguide loss mechanisms for straight and curved waveguides. The properties of passive polymers are demonstrated in the fabrication and measurement of a polymer microring resonator optical filter. Using the flexible, plastic nature of polymer materials, freestanding all-polymer microring resonator optical devices [15, 16] are presented. Based on the filtering properties of a single microring resonator, an inline optical reflector is presented theoretically and experimentally verified in passive polymer [17].

The subject of Chapter 4 is the coupled resonator optical waveguide (CROW). Both the matrix analysis and the tight-binding method of analysis are presented, en route to an experimental demonstration of a CROW in passive polymer. A Mach-Zehnder interferometer, with a conventional waveguide in one interferometer arm and a CROW in the other, is fabricated and characterized [18]. Good agreement is found between the measurement and the theoretical expectations. The possibility of polymer CROWs as delay lines is briefly proposed.

In Chapter 5, the development of a soft stamp replica molding fabrication procedure for polymer integrated optical devices is presented. The basic technique and the effects of a background residue of polymer material are presented and analyzed [19]. The high fidelity of this fabrication process is demonstrated in the replication of a polymer microring resonator and comparison of the optical spectrum of the molded microring resonator with the original [20]. Taking the technique a step further, subsequent repetition of the basic replica molding technique enables fabrication of three-dimensional multilayer polymer optical circuits [21].

Chapter 6 concerns further demonstration of the utility of the replica molding process, specifically as applied to electro-optic polymers. The definition and properties of electro-optic polymers are explored, as well as the poling of these materials. A short, proof-of-concept prototype electro-optic Mach-Zehnder modulator is fabricated by the soft stamp replica molding process and characterized [22]. Application of the fabrication procedure to a much larger, and thus lower switching voltage, Mach-Zehnder modulator is demonstrated with very good results [23].

In Chapter 7, a synopsis of the thesis work is given. The long term outlook for polymers for integrated telecommunications optics are considered.

Appendix A and B describe two of the numerical simulation methods used throughout this thesis: the beam propagation method and the finite difference mode solver, respectively.

Chapter 2

Coupled Mode Theory and Its Geometrical Representation

2.1 Introduction

Polymer waveguide materials have very little material dispersion (i.e., $dn/d\lambda$ is small), in the same range as SiO₂ [4]. This feature suggests their use in devices with a wide range of operating wavelengths since the change in refractive index with wavelength variations often ruins the intended performance and activity of the constituent elements in integrated optical devices. An obvious place to start the study of wavelength dependent components is the directional coupler. The directional coupler consists of two waveguides in close proximity to each other, such that light is transferred from one waveguide to another through optical coupling. The coupled mode theory of optical waveguides reveals that these devices are wavelength dependent through the wavelength dependent coupling coefficient. This sensitivity often undermines any attempt to produce wide-bandwidth integrated optical devices, for which couplers are fundamental building blocks. It would be useful to have a design method for optical couplers that allows for tailoring of the waveguide coupling to render changes in wavelength ineffective in the response of the coupler. This type of wavelength invariant coupler would form the cornerstone of complex wide-bandwidth integrated optical devices.

In this chapter, the theory of wavelength and fabrication-error tolerant optical

couplers is developed. The fundamental theory of optical waveguides is presented, including waveguide mode profile and propagation constant determination. The basic theory of coupled waveguide modes is examined. Following this, a geometrical representation of coupled mode theory is established, and demonstrated with the analysis of directional, adiabatic, and non-adiabatic mode evolution couplers in the geometrical framework. Using this geometrical method as a design tool, optical couplers with wavelength and fabrication-error insensitivity are set forth and are compared to standard directional couplers using numerical simulations.

2.2 Fundamental Theory of Optical Waveguides

2.2.1 The Wave Equation and Plane Waves

The equations that form the basis for all of electromagnetic theory and the experiments in this thesis are, of course, the fundamental equations of electromagnetism accredited to Maxwell [24]:

$$\nabla \cdot \vec{\mathbf{D}} = \rho \quad (2.1)$$

$$\nabla \cdot \vec{\mathbf{B}} = 0 \quad (2.2)$$

$$\nabla \times \vec{\mathbf{H}} = \vec{\mathbf{J}} + \frac{\partial \vec{\mathbf{D}}}{\partial t} \quad (2.3)$$

$$\nabla \times \vec{\mathbf{E}} = -\frac{\partial \vec{\mathbf{B}}}{\partial t} \quad (2.4)$$

where $\vec{\mathbf{E}}$ is the electric field vector, $\vec{\mathbf{B}}$ is the magnetic flux density vector, $\vec{\mathbf{D}}$ is the electric flux density vector, and $\vec{\mathbf{H}}$ is the magnetic field vector. The remaining quantities are $\vec{\mathbf{J}}$, the free current density vector, and ρ , the density of free charge. The equations relating the field vectors and the flux density vectors in some medium are the constitutive relations:

$$\vec{\mathbf{D}} = \epsilon \vec{\mathbf{E}} \quad (2.5)$$

$$\vec{\mathbf{H}} = \frac{1}{\mu} \vec{\mathbf{B}} \quad (2.6)$$

where ϵ and μ are the electric and magnetic susceptibilities, respectively, of the medium.

For what follows, we consider a special case of the Maxwell equations appropriate for most guided wave optical systems. First, we assume that the fields are present in a linear medium, that is, one for which the susceptibilities are independent of the fields. Second, we assume that the medium has sufficiently small variations of the susceptibilities in both space ($\nabla\epsilon=0$) and time ($\nabla\times\frac{\partial\mu\vec{\mathbf{H}}}{\partial t}=\mu\frac{\partial}{\partial t}\nabla\times\vec{\mathbf{H}}$). Third, we assume that there are no free charges ($\rho=0$) and no free currents ($\vec{\mathbf{J}}=0$). Taking the curl of (2.4), using (2.6) and (2.3), as well as the aforementioned assumptions, we obtain the familiar wave equation

$$\nabla^2\vec{\mathbf{E}}-\mu\epsilon\frac{\partial^2\vec{\mathbf{E}}}{\partial t^2}=0 \quad (2.7)$$

Taking the case of a single frequency solution, we separate the time dependence of the electric field from its magnitude in the product $\vec{\mathbf{E}}(\vec{r},t)=\vec{\mathbf{E}}(\vec{r})e^{i\omega t}$. Equation (2.7) then becomes

$$\nabla^2\vec{\mathbf{E}}(\vec{r})+k_0^2n^2\vec{\mathbf{E}}(\vec{r})=0 \quad (2.8)$$

where $k_0^2n^2=\omega^2\mu\epsilon$, with $k_0=\frac{2\pi\lambda}{c}$, and n is the refractive index of the medium.

The solutions to (2.8) propagating in the $+r$ direction are of the form

$$\vec{\mathbf{E}}=\vec{\mathbf{E}}_0e^{i(\omega t-k_0n\vec{r})} \quad (2.9)$$

Such waves are referred to as plane waves because for each plane (i.e., for which $\vec{r}=\text{const.}$) the phase is a constant in space.

2.2.2 The Slab Waveguide

The most basic form of a dielectric guide for electromagnetic radiation is the slab waveguide as shown in Figure 2.1. We assume propagation in the $+z$ direction. There is no variation in the y direction, but in the x dimension, there are three dielectric layers with refractive indices n_1 , n_2 , and n_3 . To guide light, the core

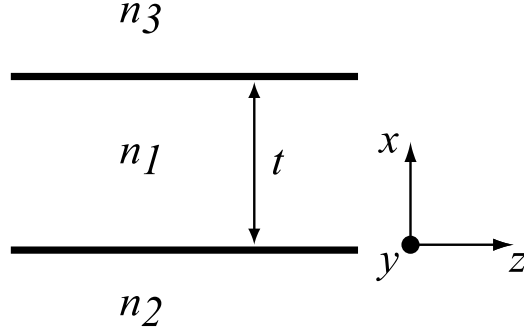


Figure 2.1: The slab waveguide structure. The waveguide core with index n_1 and thickness t is surrounded by the upper cladding with index n_3 and lower cladding with index n_2 .

refractive index n_1 must be of a larger value than the others [1].

The general plane wave solution (2.9) for the case of a plane wave with phase fronts normal to the z direction becomes

$$\vec{\mathbf{E}}(x, y, z) = \vec{\mathbf{E}}_0(x, y)e^{-i\beta z} \quad (2.10)$$

where β is referred to as the propagation constant.

Since there is no variation in the y direction, we can set $\frac{\partial}{\partial y} = 0$, and thus rewrite (2.8) and insert (2.10), to yield

$$\frac{\partial^2}{\partial x^2} E(x, y) + (k_0^2 n_i^2 - \beta^2) E(x, y) = 0 \quad (2.11)$$

which is valid for each of the dielectric layers $i = 1, 2, 3$, and for both of the components $E(x, y)$ of the vector $\vec{\mathbf{E}}(x, y)$.

In this thesis, we are concerned primarily with waveguides that support only a single mode as shown in Figure 2.2. For a full description of higher order modes and the conditions required for these higher order modes to exist, one can consult, for instance, reference [1].

There exist two possible polarizations for the slab waveguide. The first, in which the electric field vector points in the y direction, with field components E_y ,

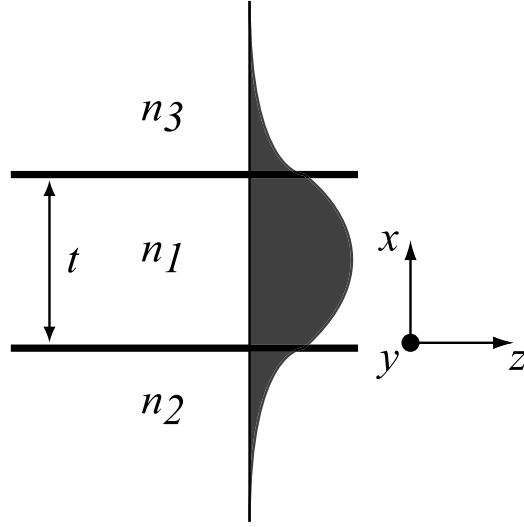


Figure 2.2: A schematic of the field distribution of the lowest order TE mode of the slab waveguide structure described in Figure 2.1.

H_x , and H_z , is referred to as transverse electric (TE). The second is characterized by the electric field confined to the $x - z$ plane, with field components E_x , E_z , and H_y , and is called transverse magnetic (TM).

As mentioned earlier, a condition for guiding was that the core refractive index n_1 be larger than the cladding indices. Let us assume that $n_1 > n_2 > n_3$. For the slab waveguide to have a single guided mode, the propagation constant must obey $k_0 n_2 < \beta < k_0 n_1$ [1]. This guarantees an electric field solution that is sinusoidal in the region of $n = n_1$ and decaying exponentials elsewhere. The TE solution for the electric field in the three sections of the slab waveguide are given by

$$E_{TE}(x) = A \cos(hx - \phi) \quad \text{where } n = n_1 \quad (2.12)$$

$$E_{TE}(x) = B e^{qx} \quad \text{where } n = n_2 \quad (2.13)$$

$$E_{TE}(x) = C e^{-p(x-t)} \quad \text{where } n = n_3 \quad (2.14)$$

where the amplitude coefficients A , B , and C are determined by normalization

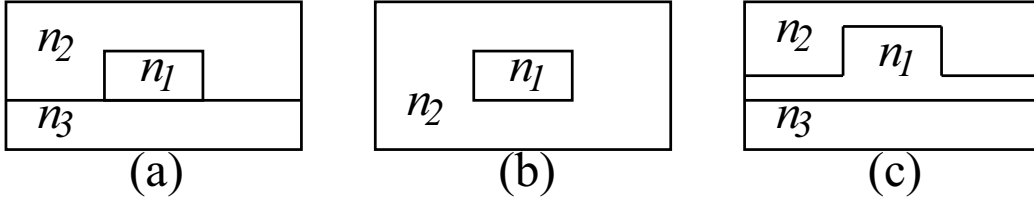


Figure 2.3: Cross sections of three typical waveguide geometries: (a) the raised strip, (b) the buried channel, and (c) the rib guide.

and h , q , and p are

$$h = \sqrt{k_0^2 n_1^2 - \beta^2} \quad (2.15)$$

$$q = \sqrt{\beta^2 - k_0^2 n_2^2} \quad (2.16)$$

$$p = \sqrt{\beta^2 - k_0^2 n_3^2} \quad (2.17)$$

These latter constants are determined by ensuring continuity of the field solutions at the interfaces. A numerical solution of the resulting eigenvalue equation determines the value of β , the propagation constant. The propagation constant is not only important for determining the phase accumulated in propagation in the z direction, but its frequency derivative is also related to the group velocity by

$$v_g = \frac{1}{\frac{d\beta}{d\omega}} \quad (2.18)$$

2.2.3 The Effective Index Method

In the preceding section, the waveguides provided confinement within a plane. In reality, however, waveguides are rarely of this form. In integrated optics, another dimension of confinement is used to further limit the spatial location of the light. As shown in Figure 2.3, the most common waveguides in integrated optics can be categorized in the following forms: the raised strip, the buried channel, or the rib form. For the raised strip, a waveguide of refractive index n_1 is fabricated on a substrate with index n_3 , and the upper cladding of index n_2 can be air or some

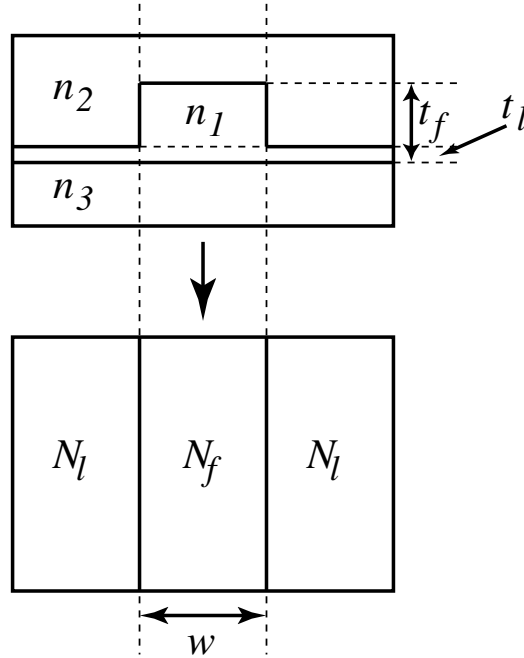


Figure 2.4: Illustration of the effective index method. The upper drawing shows the actual rib waveguide cross section and the lower drawing shows the reduced slab waveguide structure.

other material. For the buried channel guide, the core index n_1 is surrounded by a substrate and clad material of the same refractive index n_2 . The rib guide is similar to the raised strip except that there is some residual core material between the cladding and the substrate covering the extent of the substrate.

These waveguides are difficult to analyze without invoking numerical tools to predict their optical properties. One such method, called the *effective index method* [25], reduces three dimensional guided wave geometries to two dimensions. This greatly reduces the complexity of such problems and allows the routine analysis of the slab waveguide to be used to determine the optical properties of these waveguides.

To illustrate the method by example, the rib waveguide shown in Figure 2.4 will be analyzed using the effective index method. The general concept is to

regard the three sections of the waveguide cross-section (left, center, and right) as three separate slab waveguides. The steps to calculate the modal properties are as follows, closely following [25]. The procedure is the same for the channel and the lateral sections, given by subscripts f and l , respectively. First, the normalized thicknesses for channel (V_f) and lateral (V_l) regions are defined as

$$V_{f,l} = kt_{f,l}\sqrt{n_1^2 - n_3^2} \quad (2.19)$$

where $t_{f,l}$ are the thicknesses of the channel (t_f) and the lateral (t_l) sections, as shown in Figure 2.4, and k is the free space wavenumber. Next, the asymmetry parameter is defined:

$$a = \frac{(n_2^2 - n_3^2)}{(n_1^2 - n_2^2)} \quad (2.20)$$

Numerical solutions for $b_{f,l}$, the normalized guide index, are found using the equation (valid for TE modes):

$$V_{f,l}\sqrt{1 - b_{f,l}} = \nu\pi + \arctan\sqrt{\frac{b_{f,l}}{1 - b_{f,l}}} + \arctan\sqrt{\frac{b_{f,l} + a}{1 - b_{f,l}}} \quad (2.21)$$

where ν gives the mode number, i.e., $\nu = 0, 1, 2$ gives the appropriate value of the normalized guide index for the zeroth-, first-, and second-order modes. The equivalent effective indices $N_{f,l}$ of the three regions, are given by:

$$(N_{f,l})^2 \simeq n_3^2 + b_{f,l}(n_1^2 - n_3^2) \quad (2.22)$$

At this point, we have an equivalent slab waveguide with equivalent indices N_f and N_l . Now, for any two-dimensional slab waveguide simulations, we use the value of N_f for the core refractive index and N_l for the cladding refractive index. The three dimensional structure has been reduced by one dimension, allowing for simple analysis and simulation.

To determine the propagation constants of the modes in the waveguide, we repeat the previous steps that we used to solve each individual slab to calculate

the effective index of the equivalent slab. First, find the normalized thickness

$$V_{eq} = kw\sqrt{N_f^2 - N_l^2} \quad (2.23)$$

Again solve for the normalized guide index b_{eq} :

$$V_{eq}\sqrt{1 - b_{eq}} = \nu\pi + \arctan\sqrt{\frac{b_{eq}}{1 - b_{eq}}} + \arctan\sqrt{\frac{b_{eq} + a_{eq}}{1 - b_{eq}}} \quad (2.24)$$

Finally, solve for the effective index of the waveguide

$$n_{eff} \equiv N_{eq} = N_l^2 + b_{eq} (N_f^2 - N_l^2) \quad (2.25)$$

which gives the propagation constant through the relation $\beta = kn_{eff}$. This simple procedure allows a rapid analysis of the three dimensional structures shown in Figure 2.3.

2.3 Coupled Mode Theory

Coupled mode theory [1] presents the basic analytic tool to determine the features of light tunneling between two (or several) waveguides in close physical proximity. Consider two isolated waveguides, each with z -propagating fields given by

$$\vec{\mathbf{E}}_{1,2}(x, y, z) = \vec{\mathbf{E}}_{1,2}(x, y)e^{-i\beta_{1,2}z} \quad (2.26)$$

which are solutions to the individual wave equations

$$\frac{\partial^2}{\partial x^2} E_{1,2}(x, y) + \frac{\partial^2}{\partial y^2} E_{1,2}(x, y) + (k_0^2 n_{1,2}^2 - \beta_{1,2}^2) E_{1,2}(x, y) = 0 \quad (2.27)$$

The fields, refractive indices and propagation constants of the two waveguides are denoted by the subscript 1, 2. Assuming two waveguides are in close proximity to

each other, the overall field is taken to be the superposition of the individual fields

$$\vec{\mathbf{E}}(x, y, z) = \tilde{C}_1(z)\vec{\mathbf{E}}_1(x, y)e^{-i\beta_1 z} + \tilde{C}_2(z)\vec{\mathbf{E}}_2(x, y)e^{-i\beta_2 z} \quad (2.28)$$

This crucial assumption, the so-called weak coupling condition, requires that the proximity of a second waveguide does not perturb the field in the other significantly, and thus take (2.28) to be a solution of

$$\nabla^2 \vec{\mathbf{E}} + k_0^2 n^2(x, y) \vec{\mathbf{E}} = 0 \quad (2.29)$$

where, here, $n(x, y)$ is the composite refractive index profile of the two-waveguide system. Inserting the ansatz (2.28) into (2.29) and assuming that the field amplitudes do not vary rapidly while propagating (the slowly-varying approximation, i.e., taking $\frac{\delta^2 \tilde{C}_1}{\delta z^2} = 0$ and $\frac{\delta^2 \tilde{C}_2}{\delta z^2} = 0$) the result is

$$\left(-2i\beta_1 \frac{\delta \tilde{C}_1}{\delta z} + k_0^2 (n^2 - n_1^2)\right) \vec{\mathbf{E}}_1(x, y)e^{-i\beta_1 z} + \left(-2i\beta_2 \frac{\delta \tilde{C}_2}{\delta z} + k_0^2 (n^2 - n_2^2)\right) \vec{\mathbf{E}}_2(x, y)e^{-i\beta_2 z} = 0 \quad (2.30)$$

Multiplying (2.30) by $\vec{\mathbf{E}}_1^*(x, y)$ and integrating over all x and y yields the first coupled mode equation. Repeating this step but multiplying by $\vec{\mathbf{E}}_2^*(x, y)$ instead yields the second coupled mode equation. Together, the coupled mode equations are

$$\frac{d\tilde{C}_1}{dz} + ie^{-i(\beta_2 - \beta_1)z} \kappa_{12} \tilde{C}_2 = 0 \quad (2.31)$$

$$\frac{d\tilde{C}_2}{dz} + ie^{-i(\beta_1 - \beta_2)z} \kappa_{21} \tilde{C}_1 = 0 \quad (2.32)$$

with the coupling coefficients given by

$$\kappa_{12} = \frac{k_0^2 \iint (n^2 - n_1^2) \vec{\mathbf{E}}_2 \vec{\mathbf{E}}_1^* dx dy}{2\beta_1 \iint \vec{\mathbf{E}}_1 \vec{\mathbf{E}}_1^* dx dy} \quad (2.33)$$

$$\kappa_{21} = \frac{k_0^2 \iint (n^2 - n_2^2) \vec{\mathbf{E}}_1 \vec{\mathbf{E}}_2^* dx dy}{2\beta_2 \iint \vec{\mathbf{E}}_2 \vec{\mathbf{E}}_2^* dx dy} \quad (2.34)$$

The coupling coefficients determine the strength of coupling from one wave-

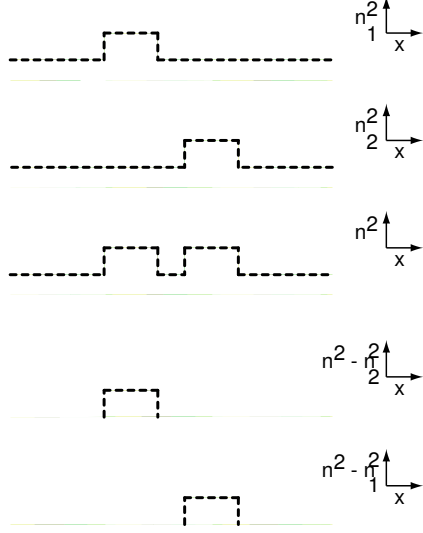


Figure 2.5: Illustration of the refractive index terms used in coupled mode theory calculations. The spatial integration in $\kappa_{12,21}$ are only over the areas shown in the bottom two drawings.

guide to another. The term $(n^2 - n_{1,2}^2)$ represents the difference between the composite refractive index profile and the refractive index profile of the individual waveguides, as illustrated in Figure 2.5.

To rewrite the coupled mode equations in a more manageable form, we substitute $\tilde{C}_{1,2} = C_{1,2}e^{i\beta_{1,2}z}$. For waveguides similar in cross-section, a stipulation to be tested for each case, one can observe that $\kappa_{12} \approx \kappa_{21}$ by inspecting (2.33) and (2.34). Defining $\kappa \equiv -i\kappa_{21}$, we finally have

$$\frac{d}{dz} \begin{pmatrix} C_1 \\ C_2 \end{pmatrix} = \begin{pmatrix} -i\beta_1 & -\kappa^* \\ \kappa & -i\beta_2 \end{pmatrix} \begin{pmatrix} C_1 \\ C_2 \end{pmatrix} = \mathbf{M} \begin{pmatrix} C_1 \\ C_2 \end{pmatrix} \quad (2.35)$$

It should be noted that typically κ_{21} in (2.34) is a real number, so κ in (2.35) is a negative, purely imaginary number.

For a z -independent coupling matrix \mathbf{M} represented in (2.35), a solution of the coupled mode equations $\vec{C}(z) = [C_1(z) \ C_2(z)]^T$ is found by direct integration.

The result is

$$\vec{C}(z) = e^{\mathbf{M}z} \vec{C}(0) \quad (2.36)$$

Using the definition for the exponential of a matrix, the solution (2.36) is explicitly

$$\vec{C}(z) = \mathbf{T} \vec{C}(0) \quad (2.37)$$

where

$$\mathbf{T} = e^{-i\bar{\beta}z} \begin{bmatrix} \cos(\sigma z) - i\frac{\delta}{\sigma} \sin(\sigma z) & -i\frac{|\kappa|}{\sigma} \sin(\sigma z) \\ -i\frac{|\kappa|}{\sigma} \sin(\sigma z) & \cos(\sigma z) + i\frac{\delta}{\sigma} \sin(\sigma z) \end{bmatrix} \quad (2.38)$$

and

$$\bar{\beta} \equiv \frac{\beta_1 + \beta_2}{2} \quad \delta \equiv \frac{\beta_1 - \beta_2}{2} \quad \sigma \equiv \sqrt{\delta^2 + |\kappa|^2} \quad (2.39)$$

The term $e^{-i\bar{\beta}z}$ is typically ignored as a common phase that disappears upon calculating the power.

For similar waveguides, i.e., for which $\beta_1 = \beta_2 \equiv \beta$, (2.38) reduces to a more tractable form. This type of waveguide structure is called the *directional coupler* and has the transfer matrix given by

$$\mathbf{T} = e^{-i\beta z} \begin{bmatrix} \cos(|\kappa|z) & -i \sin(|\kappa|z) \\ -i \sin(|\kappa|z) & \cos(|\kappa|z) \end{bmatrix} \quad (2.40)$$

Thus, for light input to waveguide one, $\vec{C}(0) = [1 \ 0]^T$, the output is

$$C_1(z) = e^{-i\beta z} \cos(|\kappa|z), \quad C_2(z) = -ie^{-i\beta z} \sin(|\kappa|z) \quad (2.41)$$

Physically, the input power “sloshes” back and forth in a sinusoidal manner, with the final output power ratio being precisely determined by the distance z over which the waveguides are coupled. The coupling coefficient (2.33) for two similar waveguides of a directional coupler is [1]

$$\kappa = \frac{2h^2 p e^{-ps}}{\beta(w + 2/p)(h^2 + p^2)} \quad (2.42)$$

where h and p are defined in (2.15) and (2.17), w is the waveguide width, and β is the propagation constant.

For all but the most simple systems, (2.38) is quite formidable. It is often written in shorthand as

$$\mathbf{T} = \begin{bmatrix} t & -\kappa^* \\ \kappa & t^* \end{bmatrix} \quad (2.43)$$

It should be made abundantly clear that κ in (2.43) is not the same coupling coefficient as that of (2.42), but is rather a shorthand notation for the off-diagonal elements in (2.38).

2.4 The Geometrical Representation of Coupled Mode Theory

Optical couplers are of obvious importance in optical electronics and have been analyzed by various formulations of coupled mode theory (CMT) for many years [1, 26]. Whereas CMT excels in analysis, other tools may prove more useful in design. A useful geometrical representation of CMT would yield intuition into the nature of various couplers and would facilitate design as well as analysis. The geometrical representation employed in what follows is not in itself new. Feynman et al., originally formulated a similar geometrical representation for the two dimensional Schrödinger equation in solving maser problems [27]. Ulrich first cast CMT into an analogous geometrical representation [28] that was later extended and generalized in References [29, 30]. Besides the original examples of the geometrical representation, little work has been done to explore its worth as a design implement.

Using the geometrical representation as a guide, we classify optical couplers into three groups: (1) stationary mode, (2) adiabatic mode evolution, and (3) non-adiabatic mode evolution. Stationary mode couplers are standard symmetric directional couplers, for which the system eigenmodes remain the same throughout the length of the coupler. A mode evolution coupler, as in Reference [31], has con-

tinuously changing refractive index profile throughout the length of the coupler, resulting in continuous evolution of the system eigenmodes. Such a coupler is adiabatic when the change in shape is gradual enough to satisfy the adiabatic criteria [32], so the actual states closely follow the evolving eigenmodes. For non-adiabatic mode evolution couplers, changes in refractive index profile are fast enough such that the actual states of the guided beam do not closely follow the changing eigenmodes, but we assume are slow enough so as not to introduce excessive loss.

A viable design and characterization tool for the general non-adiabatic mode evolution type coupler has yet to be devised, as was pointed out by Li and Henry [33]: “In general, a coupler can be neither symmetrical nor adiabatic. . . There is currently no simple and general method for visualizing the physical process and predicting the transmission properties of such general couplers.” The geometrical representation that follows succeeds in this endeavor.

From Section 2.3, specifically (2.35), the complex optical field amplitudes \vec{C} evolve in a coupler according to the equations

$$\frac{d\vec{C}}{dz} = \mathbf{M}\vec{C} \quad (2.44)$$

where \mathbf{M} is the coupling matrix given in (2.35), with diagonal elements $M_{11} = -i\beta_1$, $M_{22} = -i\beta_2$ and off-diagonal elements $M_{12} = -\kappa^*$, $M_{21} = \kappa$.

A normalized state $\hat{c} = \frac{\vec{C}}{\sqrt{\vec{C}\vec{C}^*}}$ is depicted in the geometrical representation of CMT as a unit vector delineating a point in a real three dimensional space using the relations [29, 34]

$$s_k = \hat{c}^\dagger \sigma_k \hat{c} \quad (2.45)$$

where the σ_k are the Pauli spin matrices (cyclically permuted from the standard order)

$$\sigma_1 = \begin{pmatrix} 1 & 0 \\ 0 & -1 \end{pmatrix} \quad \sigma_2 = \begin{pmatrix} 0 & 1 \\ 1 & 0 \end{pmatrix} \quad \sigma_3 = \begin{pmatrix} 0 & -i \\ i & 0 \end{pmatrix} \quad (2.46)$$

The state vector base states and the corresponding waveguide states are shown in

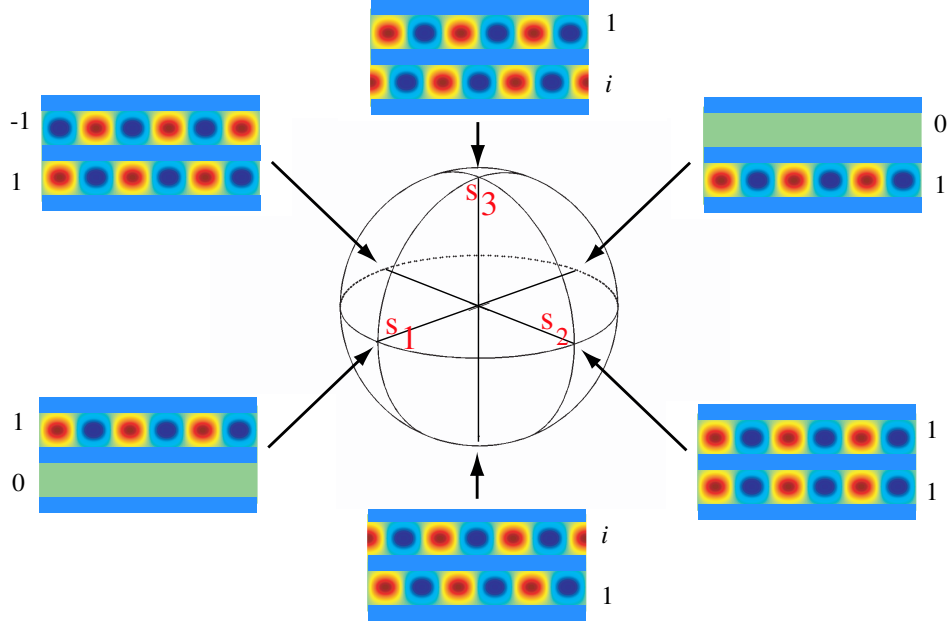


Figure 2.6: The Poincaré sphere base states. A state vector \mathbf{s} on any of the axes represents the two-waveguide state as shown. The numbers represent the relative amplitudes and phases in each waveguide for the corresponding base states.

Figure 2.6.

The coupling operator, \mathbf{M} , similarly transforms in this representation into a real three-element rotation vector according to

$$\Omega_k = i\text{Tr}(\mathbf{M}\sigma_k) \quad (2.47)$$

Using (2.45) and (2.47) in conjunction with (2.44), the transformed coupled mode equations become

$$\frac{d\vec{s}}{dz} = \vec{\Omega} \times \vec{s} \quad (2.48)$$

The coupled mode equations are now regarded dynamically as sequential infinitesimal rotations of the instantaneous state vector $\mathbf{s}(z_0)$ on the unit sphere around the instantaneous rotation axis $\mathbf{\Omega}(z_0)$. As seen from (2.48), a state vector is stationary when collinear with the rotation vector. Thus the antipodal points $\pm\hat{\mathbf{\Omega}}$

represent the two local eigenstates of the waveguide system. For non-constant $\mathbf{\Omega}(z)$, a solution of (2.48) is obtained by direct numerical integration. This pictorial representation of a two-state system is analogous to the Poincaré sphere of polarization optics [34].

Specifically, for the coupled mode equations above, the instantaneous rotation vector (2.47) becomes

$$\vec{\Omega} = \begin{pmatrix} 2\Delta\beta \\ 2\text{Im}(\kappa) \\ -2\text{Re}(\kappa) \end{pmatrix} \quad (2.49)$$

where $\kappa = \text{Re}(\kappa) + i\text{Im}(\kappa)$ and $2\Delta\beta = (\beta_2 - \beta_1)$. As we noted in Section 2.3, the coupling coefficient is typically taken as purely imaginary. However, in general, it may be complex (e.g., when there is gain or loss, or when one accounts for the effect of non-parallel waveguides). Here we assume the convention that κ is purely imaginary. Consequently for the remainder of this chapter, we consider only rotation vectors that lie on the equator of the sphere, in the plane given by the first two components of (2.49), with magnitude of rotation $|\Omega| = \sqrt{(|\kappa|)^2 + (\Delta\beta)^2}$. While the rotation vector is confined to the equator, the state vector can take any position on the sphere. Consistent with this restriction on $\vec{\Omega}$, we design the evolution of the rotation vector to produce a state vector trajectory exhibiting desired properties. In the following section, we describe three design examples utilizing this approach.

2.5 Symmetric and Mode Evolution Optical Couplers

2.5.1 Symmetric Optical Couplers

A stationary mode coupler is defined as having eigenmodes that do not change with z and so the rotation axes, $\pm\hat{\Omega}$, are stationary. The magnitude of $\vec{\Omega}$, on the other hand, may vary. Starting at some initial state \vec{s}_0 , the state vector $\vec{s}(z)$ performs a rotation around the diameter connecting $\pm\hat{\Omega}$ at a varying rate $|\mathbf{\Omega}(z)|$. As an example let us consider a standard symmetric 3-dB directional coupler with

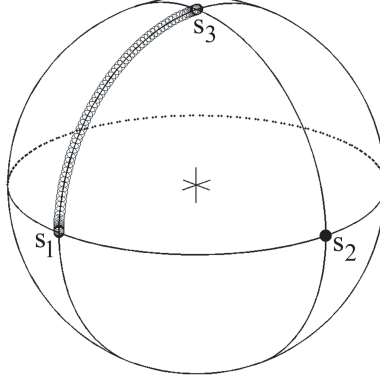


Figure 2.7: Geometrical representation of a 3-dB stationary mode coupler. The rotation vector, Ω , (filled circle) remains statically collinear with the s_2 axis, while the magnitude of the rotation vector dictates the rotation of the state vector, \mathbf{s} , (unfilled circles) from the s_1 -axis to the s_2 -axis.

identical waveguides whose geometrical representation is given in Figure 2.7.

Since $\Delta\beta = 0$ and κ is purely imaginary, using (2.49), we obtain the rotation vector $\vec{\Omega} = 2|\kappa|[0 \ 1 \ 0]^T$. In this case $\pm\hat{\Omega}$ corresponds to the well-known symmetric and antisymmetric eigenmodes (also referred to as supermodes), $\hat{c}^\pm = \frac{1}{\sqrt{2}}[1 \ \pm 1]^T$. Assuming that light is launched into waveguide 1, the initial amplitude state is $\hat{c}^i = [1 \ 0]^T$, with corresponding state vector $\vec{s}^i = [1 \ 0 \ 0]^T$ on the sphere. We obtain 3-dB coupling ($\hat{c}^f = \frac{1}{\sqrt{2}}[1 \ i]^T$) by controlling the magnitude of the rotation vector $|\vec{\Omega}| = 2|\kappa|$ in the following way:

At the input of the coupler $|\vec{\Omega}|$ is very small where the waveguides are far apart. The magnitude is then increased to the maximum value in the coupling region where it remains for the prescribed length, at which point the waveguides diverge and $|\vec{\Omega}|$ again becomes small. The total trajectory of the state vector is simply the quarter rotation of the initial state vector to the final state vector $\vec{s}^f = [0 \ 0 \ 1]^T$ around the rotation axis.

2.5.2 Adiabatic Mode Evolution Optical Couplers

In adiabatic mode evolution couplers, the changes in the direction of the rotation vector are slow enough so that system states closely follow the evolving eigenmodes. The requirement for the ‘slowness’ of change is determined by an adiabaticity condition. Typically, one requires that any change in the waveguide structure occurs over a distance much longer than the beat length between the two local eigenmodes [35]. In our notation, this beat length is $\frac{2\pi}{|\vec{\Omega}|}$. If this condition is satisfied, an input state vector aligned with one of the eigenmodes will remain so for the entire span of the coupler.

An intuitive adiabaticity condition for optical couplers can be derived in the geometrical representation. As previously described, a state vector circulates on the sphere around the diameter connecting the eigenstates, with a rotational velocity equal to $|\vec{\Omega}|$. Let ρ be the radius of rotation, given by the sine of the angle between the actual state of the optical beam and the local eigenmode. For the actual state to remain ‘near’ the eigenmode for the duration of the coupler, the tangential velocity of the state vector must be larger than, or at least equal to, the tangential velocity of the eigenmodes on the sphere:

$$\rho|\vec{\Omega}| \geq \left| \frac{d\hat{\Omega}}{dz} \right| \quad (2.50)$$

For the strictly adiabatic case, the states would ideally occupy the local eigenmodes for all z , that is, $\rho = 0$, but it is evident from (2.50) that for finite $|\vec{\Omega}|$, any change in the eigenmodes would require infinite distance in z . The choice of the allowed range of ρ presents a design trade-off between long coupler length and the deviation from the desired output ratio.

As an example we consider a 3-dB adiabatic coupler whose geometrical representation is given in Figure 2.8. As before, light is launched in waveguide 1, corresponding to normalized field amplitude $\hat{c}^i = [1 \ 0]^T$ and state vector $\vec{s}^i = [1 \ 0 \ 0]^T$. The initial eigenmode ideally would be the same as the initial state vector. However, this requires $\kappa = 0$ and therefore, infinite separation between the wave-

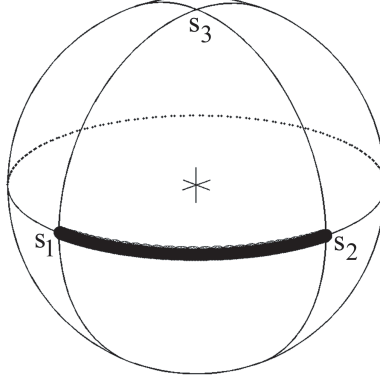


Figure 2.8: Geometrical representation of a 3-dB adiabatic mode evolution coupler. The rotation vector (filled circles) itself rotates from the s_1 -axis, corresponding to the individual waveguide modes, to the s_2 -axis, representing modes of equal amplitude and phase. The magnitude of the rotation vector is large so that the state vector (unfilled circles) closely follows the trajectory of the rotation vector.

uides. Thus, we choose as our initial eigenmode $\hat{\Omega} = [\sqrt{1-\delta^2} \ \delta \ 0]^T$, where δ is the small deviation from the actual state. The final eigenmode for 3-dB coupling is $\hat{\Omega} = [0 \ 1 \ 0]^T$. Between its endpoint values, many choices for the rotation vector $\hat{\Omega} = [\cos(\Theta(z)) \ \sin(\Theta(z)) \ 0]^T$ are available. One such choice, used for this example, is

$$\Theta(z) = \left\{ \begin{array}{ll} \left(\frac{\Theta_0}{2} - \frac{\pi}{2} \right) \left(\cos\left(\frac{\pi z}{l} - 1\right) \right) + \Theta_0 & 0 < z < l \\ \frac{\pi}{2} & l < z < L \end{array} \right\} \quad (2.51)$$

The magnitude $|\Omega| = \sqrt{(|\kappa|)^2 + (\Delta\beta)^2}$ is large and constant until $\hat{\Omega}$ attains its final constant position, $z = l$, where the magnitude decreases exponentially, resulting in linear divergence of the two waveguides.

2.5.3 Non-Adiabatic Mode Evolution Optical Couplers

Non-adiabatic mode evolution couplers have neither stationary modes nor adiabatic mode conversion. As with adiabatic-type couplers, the eigenmodes change

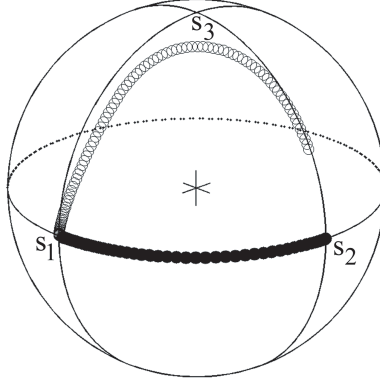


Figure 2.9: Geometrical representation of a 3-dB non-adiabatic mode evolution coupler. The rotation vector (filled circles) rotates from the s_1 -axis to the s_2 -axis and back. However, the magnitude of the rotation vector is smaller than in the adiabatic case (Figure 2.8), so that the state vector (unfilled circles) cannot closely follow the rotation vector. In this way, the state vector is transported from its initial state on the s_1 -axis to the meridian representing equal amplitude.

with z . However, in this case, the adiabaticity condition (i.e., 2.50) is not met. On the sphere, the magnitude of the rotation vector is smaller than in the adiabatic case, so the state vector does not closely follow the evolving eigenmode. Rather the rotation vector is controlled to produce a state vector trajectory with desired properties.

Let us consider a 3-dB non-adiabatic mode evolution coupler corresponding to the geometrical representation of Figure 2.9. Again, we take the initial state as in the previous two cases. However, for the output, we only require that the final state lies on the meridian through s_2 and s_3 , representing equal intensity. Here, for reasons explained below, we take the initial and final rotation vectors to be the same, $\hat{\Omega} = [1 \ 0 \ 0]^T$. Between initial and final points, the rotation vector sweeps towards and back from some maximal point in the plane. Specifically, again taking

$\hat{\Omega} = [\cos(\Theta(z)) \ \sin(\Theta(z)) \ 0]^T$, we choose:

$$\Theta(z) = \left(\frac{\pi}{2}\right) e^{-\left(\frac{4z}{L}-2\right)^2} \quad (2.52)$$

The magnitude is selected to be large and constant. Physically, this corresponds to beginning and ending the coupler with large dephasing and little coupling, and achieving the maximum coupling (minimum dephasing) in the center of the device. The reason for this is best understood in the context of the sphere. The motion of the rotation vector, when divided into infinitesimal sections, constitutes a series of infinitesimal rotations of the state vector. If the functional form of $\vec{\Omega}$ is chosen properly, the finite rotation comprised of infinitesimal rotations transports the state vector along some trajectory between the requisite endpoints. Once the rotation vector has returned to its original starting point, the state can only rotate around the line connecting the final eigenmodes, i.e., on the meridian defining an equal amplitude sum of the original eigenmodes. Note that any continued rotation merely contributes to the relative phases of the waveguide outputs while maintaining the output intensity ratio.

2.5.4 Coupler Index Profiles and Simulations

In designing optical couplers using the geometrical representation, we begin by defining $\vec{\Omega}$ that generally varies in both amplitude and direction. The task at hand is to convert this trajectory into a waveguide refractive index profile. For simplicity, we choose to model our waveguide structures as stepped-index slabs, since using effective index methods, three-dimensional structures can be approximated as slabs.

Given $\vec{\Omega}$, the propagation constants of the waveguides are determined from (2.49) according to $\beta_1(z) = \bar{\beta} + \Delta\beta(z)$ and $\beta_2(z) = \bar{\beta} - \Delta\beta(z)$, where the average propagation constant $\bar{\beta} = \frac{\beta_1 + \beta_2}{2}$ is chosen so that the waveguides remain single-mode. The widths of the waveguides are likewise chosen to be of the form $w_1(z) = \bar{w} + \Delta w(z)$ and $w_2(z) = \bar{w} - \Delta w(z)$. From the well-known solution to the slab

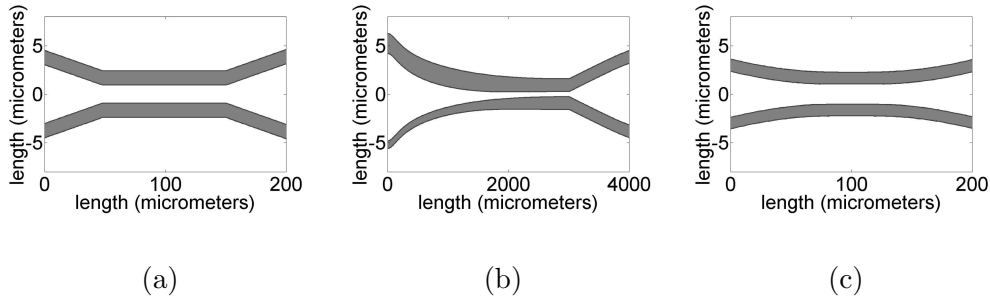


Figure 2.10: Refractive index profiles for the three types of couplers described above. In (a) the symmetric directional coupler, in (b) the adiabatic coupler, and in (c) the non-adiabatic mode evolution coupler.

waveguide [1], the widths of the waveguides $w_{1,2}$ can be numerically calculated given the propagation parameters $\beta_{1,2}$ and core and cladding indices.

Upon obtaining the widths $w_1(z)$ and $w_2(z)$ of the waveguides, and given $\text{Im}(\kappa)$ from (2.49), the gap $g(z)$ between the waveguide centers can be determined. Standard coupled mode theory expressions for the coupling coefficient [1] can be numerically inverted to determine the gap $g(z)$ between waveguides for each z .

Figure 2.10 shows the refractive index profiles, calculated using the preceding steps, for the three example couplers discussed above. To verify the predictions of the geometrical representation, we implement the split-step fast-Fourier transform beam propagation method (BPM, see Appendix A). For the simulations, the index contrast is taken to be 0.05 for the adiabatic mode evolution coupler and 0.10 for the others. The field width and calculation step size are taken as $25 \mu\text{m}$ and 0.2 (1.0 for the adiabatic coupler) μm , respectively. The lengths are as shown in Figure 2.10. The results of the BPM simulations shown in Figure 2.11 corroborate the predictions of the geometrical representation.

The geometrical representation of coupled mode theory can be used effectively to visualize and predict the output properties of general optical couplers. The intuitive insight gleaned by this representation is its primary advantage in analysis. However, as has been demonstrated, the geometrical representation also proves useful as an effective design tool for achieving specified amplitude and phase re-

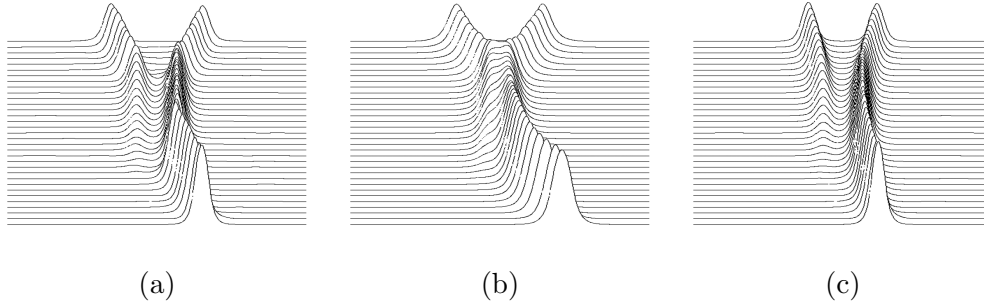


Figure 2.11: Beam propagation simulations for the three refractive index profiles shown in Figure 2.10. In each case, light is input into one waveguide and the resultant output is that of equal power between the two waveguide outputs. In (a) the symmetric directional coupler, in (b) the adiabatic coupler, and in (c) the non-adiabatic mode evolution coupler.

sponses of optical couplers. The design of a coupler reduces to the designation of an eigenmode trajectory and a corresponding state vector trajectory on the sphere. Fine detail, such as output phase relationship or wavelength response, is more easily resolved in this representation, enabling exploration of non-standard couplers exhibiting special characteristics. For instance, novel non-adiabatic mode evolution couplers can be designed to have an arbitrary phase relationship between the coupler outputs or a specific wavelength response, as will be presented in the following section.

2.6 Wavelength-Invariant and Fabrication Error Tolerant Optical Couplers

Two-by-two optical couplers that maintain output differential phase and relative amplitude conditions despite operating wavelength variation and fabrication errors are of utmost importance in integrated optics, especially for cascaded filters and modulators [36]. To this end, Mach-Zehnder structures can be constructed with a good degree of tolerance in the output amplitudes [37], however in such constructions the output differential phase changes maximally with wavelength variations,

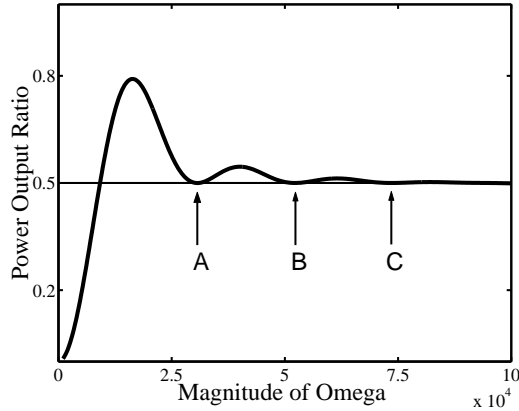


Figure 2.12: Power output ratio as a function of $|\Omega|$ for the raised cosine shape function. Points A, B, and C represent couplers with the desired 3-dB power output ratio.

rendering these devices less useful in filter applications. The most promising technology for achieving the desired tolerances has been the adiabatic coupler [35], for which the local system states follow adiabatically the local eigenstates of the waveguiding system and, thus, mode conversion between eigenstate populations is minimized. However, this requires structures that change over distances much longer than the beat length at any cross section of the coupler, thus limiting the usefulness of adiabatic couplers. Here we describe a novel design approach which is based on varying the local eigenstates while keeping their beat length constant. It is shown that by choosing the beat length with discretion while relaxing adiabatic criteria, adiabatic-like wavelength variation immunity and fabrication tolerance can be realized for much shorter device lengths.

We now describe by an example, how the formalism of Section 2.4 can be used for the design of novel couplers with unique features. The device we examine is a 3-dB non-adiabatic mode evolution coupler that, unlike a conventional directional coupler, yields no phase shift between the output waveguides. In choosing the shape function $\theta(z)$ to obtain the desired 3-dB power output ratio and phase relationship, we require the initial and final eigenstates, assuming light is input

in waveguide 1, to be $\hat{\varepsilon}^{\text{initial}} = [1 \ 0]^T$ and $\hat{\varepsilon}^{\text{final}} = (1/\sqrt{2})[1 \ 1]^T$, corresponding in the geometrical representation to $\hat{\Omega}^{\text{initial}} = [1 \ 0 \ 0]^T$ and $\hat{\Omega}^{\text{final}} = [0 \ 1 \ 0]^T$. We thus need a smoothly changing function with beginning and ending points $\theta = 0$ and $\theta = \pi/2$. Various shape functions have been compared [31], however, here we choose for illustrative purposes the raised cosine function

$$\theta(z) = \left(\frac{\theta_0}{2} - \frac{\pi}{4}\right) \left(\cos \frac{\pi z}{l} - 1\right) + \theta_0 \quad (2.53)$$

where l is the half-length of the coupler and θ_0 is an additive constant preventing $|\kappa| = 0$ (infinite waveguide separation). The magnitude of the rotation vector is taken to be constant throughout the length of the 3-dB portion of the coupler for simplicity. Beyond the point where the desired 3-dB output is obtained, the magnitude of rotation can be exponentially decreased, linearly separating the waveguides. This latter portion is of little consequence in the current study and is ignored in what follows. As discussed previously [38], to obtain the desired power output ratio, it is important to carefully choose specific ranges of the product $|\Omega| \cdot l$ for a given shape function. As optical component miniaturization and integration progresses and as planar lightwave circuit complexity grows, coupler lengths are severely restricted, so it is more realistic in this point of view to consider the length as restricted to a constant, and to carefully select ranges of $|\Omega|$ to obtain the desired output. Figure 2.12 shows a plot of the power output ratio for the raised cosine shape function, as a function of $|\Omega|$. As can be seen, there exist several values of $|\Omega|$ where the desired power output ratio (0.5) is obtained. Shape functions exhibiting smaller ripple exist, but at the cost of larger $|\Omega|$ or longer length. Larger $|\Omega|$ results in couplers that change rapidly in shape, increasing scattering loss, and alternatively longer lengths are against the spirit of this study. Referring to Figure 2.12, the perfectly adiabatic limit results from $|\Omega| \cdot l \rightarrow \infty$.

Once the magnitude $|\Omega(z)|$ and shape function $\theta(z)$ are chosen to achieve the desired output ratio and phase, the refractive index profile is computed as follows. For simplicity, we model the system as a slab waveguide structure of length 300

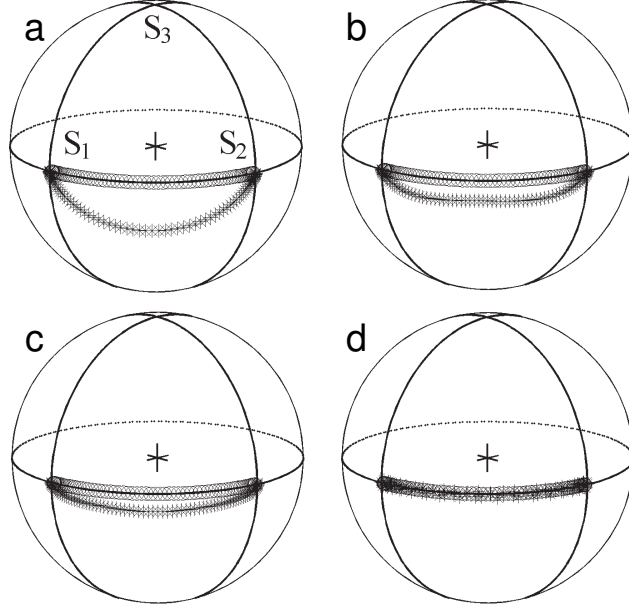


Figure 2.13: Geometrical representation of the eigenstate (\circ) and system state (\times) trajectories. The system states begin occupying one eigenmode, that is, light is injected into waveguide 1, and end in the eigenmode given by equal output power and phase. Figures 2.13 (a), (b), and (c) depict trajectories as calculated for $|\mathbf{\Omega}|$ given by points A, B, and C, respectively, for Figure 2.12. In (d) we show the coincident system state and eigenstate trajectories of a long-length adiabatic coupler for comparison.

μm , with core and cladding refractive indices of 1.55 and 1.5. The first element of the rotation vector immediately yields the individual propagation constants $\beta_1(z) = \bar{\beta} + \Delta\beta(z)$ and $\beta_2(z) = \bar{\beta} - \Delta\beta(z)$, assuming a constant average propagation constant $\bar{\beta} = (\beta_1 + \beta_2)/2$ that ensures single-mode operation. From these, the waveguide widths are obtained by inverting the solutions for the propagation constants of slab waveguides as detailed in [1]. Finally, the second element of the rotation vector is used in the equation relating the coupling coefficients to the waveguide widths and center-to-center separation.

Consider points A, B, and C in Figure 2.12, where the magnitude of the rota-

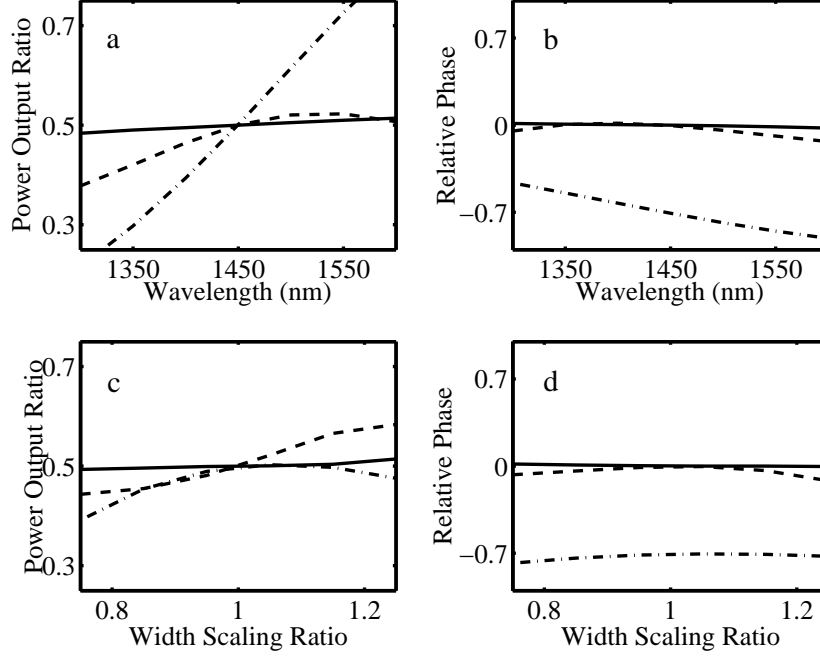


Figure 2.14: Power output ratios and relative output phases as a function of wavelength (a,b) and width scaling factor (c,d). The dash-dot (- · -) line represents a symmetric directional coupler for comparison. The dashed (- - -) and solid (—) lines give the output ratios and relative phases corresponding to couplers designed with $|\Omega|$ as given by points (a) and (b) in Figure 2.12, respectively.

tion vector yields couplers exhibiting the desired 3-dB power splitting and phase relationship. To give a geometrical understanding to couplers designed with $|\Omega|$ at these points, we calculate the state vector trajectories and plot them in the geometrical representation along with the eigenstate trajectories in Figure 2.13 (a), (b), and (c), corresponding with the letter designations in Figure 2.12. These trajectories represent the crossing of the final state and the final desired state. With increasing $|\Omega|$, the trajectories tend toward adiabatic behavior, for which the state vector and eigenstate remain arbitrarily close, as in Figure 2.13 (d).

To illustrate the wavelength insensitivity of the power output ratios and relative output phases for such non-adiabatic 3-dB coupling structures, we calculate the state vector trajectories as a function of wavelength using the model param-

eters as described above. The power output ratios are plotted in Figure 2.14 (a), over a wavelength range of 1300 to 1600 nm. For comparison, the wavelength dependence of a standard symmetric directional coupler is also shown. Clearly, the coupler designed using $|\Omega(z)|$ chosen at point A is a marginal improvement over a directional coupler, but the choice of $|\Omega(z)|$ at point B yields a coupler with a good degree of wavelength invariance. Point C gives even further improvement, but is not shown as it essentially matches the desired 3-dB output throughout the band. The relative output phases are shown in Figure 2.14 (b), and as for the case of the power output ratio, a good degree of phase invariance is obtained for the choice of $|\Omega(z)|$ at point B in Figure 2.12.

In photo- or electron-beam lithography used for the production of optical integrated circuits, an exposure error may result in a disparity of the intended waveguide widths and the actual values. To simulate this, we calculate the power output ratio and output phases while varying the intended waveguide width via a scaling factor ranging from 0.75 to 1.25. The power output ratio results as calculated using matrix methods are shown in Figure 2.14 (c), and the corresponding relative output phase calculations are shown in Figure 2.14 (d). Again, as in the case of wavelength variations, we see marked improvement over a directional coupler when $|\Omega(z)|$ is chosen as point B of Figure 2.12.

As an independent corroboration of the results as calculated using the matrix methods, beam propagation method (BPM, see Appendix A) simulations were employed. Results of the simulations agree quite well with the wavelength and scaling factor responses as predicted by the matrix method, and thus, are not shown.

We have presented a scheme for the design of optical couplers with a high degree of wavelength insensitivity and fabrication tolerance. It has been demonstrated that it is possible to obtain properties similar to those of purely adiabatic couplers, i.e., good wavelength insensitivity and fabrication tolerances, if the design parameters are chosen with care. The physical reason for the adiabatic-like features is due to the fact that as the wavelength is varied or the waveguide shapes

are scaled, $|\mathbf{\Omega}(z)|$ is changed by some amount. The key feature, therefore, to attaining the desirable properties of adiabatic couplers, is the slope of the curve shown in Figure 2.12 near the points of 3-dB output. The smaller the slope, the smaller the deviation from the desired output.

Chapter 3

Polymer Microring Resonator Optical Filters

3.1 Introduction

The practical application of many devices envisioned for integrated optics has been hindered due to immaturity of the fabrication methods necessary for realization. The advent of high resolution and rapid processing of passive polymers enables fulfilment of the proposals of optical communications engineers. Among the most important of these previously proposed devices is the microring resonator.

Originally proposed in 1969 for channel dropping in optical communications systems [39], microring and microdisk resonators have recently become the subject of intense research for a variety of applications [40, 41, 42, 43, 44, 45, 46, 50, 69, 70, 73, 74]. The original ideas of wavelength routing and switching have been extended, resulting in several synthesis and analysis techniques for high-order filtering using multiple resonators [40, 41]. Microrings have been used to demonstrate optical modulation using the electro-optic effect in polymer [42], and for all-optical switching using free-carrier injection in GaAs-AlGaAs [43]. In virtue of their long photon lifetimes, high quality factor resonators may be applied as optical delay lines [44] and for low threshold lasers [45]. More recently, interest in biological sensing has led to the development of photonic biosensors based on microring resonators [46].

In this chapter, microring resonators are examined using the established the-

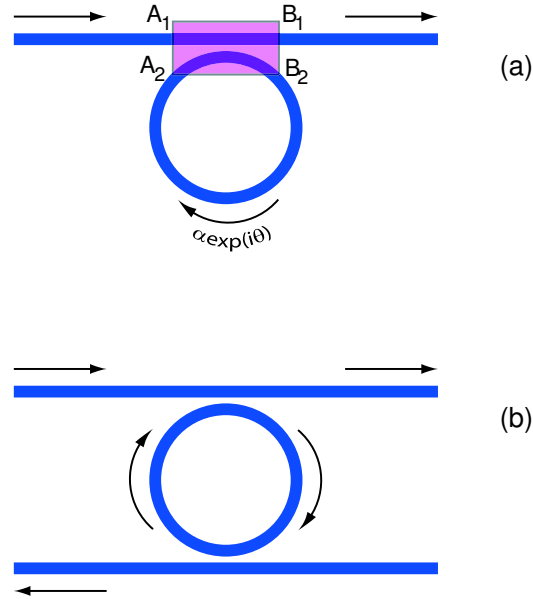


Figure 3.1: Microring resonators side coupled to one waveguide in (a), and side coupled to two waveguides in (b).

ory and are experimentally demonstrated using optical polymers. First, the fundamental properties of microring resonators are ascertained, demonstrating the wavelength filtering properties and quantities such as the quality factor, finesse, free spectral range, etc. Loss mechanisms in straight and curved waveguides are explained and the properties of passive polymer materials are examined. Microring resonator devices based on these polymer materials are demonstrated, including a chip-based microring resonator optical filter, a free-standing all-polymer microring resonator optical filter, and a microring resonator based inline reflector.

3.2 Fundamental Theory of Microring Resonators

3.2.1 The Spectral Response and Related Quantities

The theory that serves as the basis of microring resonators is very similar to that of Fabry-Perot resonators. In the following analysis, Reference [47] is followed closely. A schematic diagram of the simple ring resonator side coupled to a single

waveguide is shown in Figure 3.1(a). From Section 2.3, the boxed portion of Figure 3.1(a) obeys the coupled mode equations, with the solution given by

$$\begin{bmatrix} B_1 \\ B_2 \end{bmatrix} = \begin{bmatrix} t & -\kappa^* \\ \kappa & t^* \end{bmatrix} \begin{bmatrix} A_1 \\ A_2 \end{bmatrix} \quad (3.1)$$

where $A_{1,2}$ and $B_{1,2}$ are the optical field amplitudes as given in shown in Figure 3.1, t is the field amplitude that passes the coupler given a unity input, and κ is the field amplitude that couples into or out of the ring for a unity input.

In traveling the ring circumference, the optical field B_2 that couples into the ring incurs a phase accumulation and amplitude decrease that result in an input to the coupler A_2 given by

$$A_2 = \alpha \exp(i\theta) B_2 \quad (3.2)$$

The phase term $\theta = \beta L$ is equal to the propagation constant β multiplied by the length $L = 2\pi r$ the field travels for a ring with radius r . The propagation constant can be calculated using the effective index method of the previous chapter, and the relation $\beta = \frac{2\pi n_{eff}}{\lambda}$, where n_{eff} is the effective refractive index of the waveguide and λ is the propagation wavelength. The term α represents the field amplitude remaining after one circulation, i.e., $\alpha = 1$ for zero internal loss.

Inserting (3.2) into (3.1), and solving for the normalized output amplitude, the result is

$$\frac{B_1}{A_1} = \frac{t - \alpha \exp(i\theta)}{1 - t^* \alpha \exp(i\theta)} \quad (3.3)$$

The normalized circulating field is similarly

$$\frac{A_2}{A_1} = \frac{\kappa \alpha \exp(i\theta)}{1 - t^* \alpha \exp(i\theta)} \quad (3.4)$$

Multiplying each of the above by the corresponding complex conjugate, the normalized power output and normalized circulating power are

$$T = \left| \frac{B_1}{A_1} \right|^2 = \frac{\alpha^2 + |t|^2 - 2\alpha|t| \cos(\theta + \phi_t)}{1 + \alpha^2|t|^2 - 2\alpha|t| \cos(\theta + \phi_t)} \quad (3.5)$$

and

$$\left| \frac{A_2}{A_1} \right|^2 = \frac{\alpha^2 (1 - |t|^2)}{1 + \alpha^2 |t|^2 - 2\alpha |t| \cos(\theta + \phi_t)} \quad (3.6)$$

where $t = |t| \exp(i\phi_t)$. When $(\theta + \phi_t) = 2m\pi$, for integer m , the input wavelength is said to be resonant with the ring, and the output and circulating power are

$$\left| \frac{B_1}{A_1} \right|^2 = \frac{(\alpha - |t|)^2}{(1 - \alpha|t|)^2} \quad (3.7)$$

and

$$\left| \frac{A_2}{A_1} \right|^2 = \frac{\alpha^2 (1 - |t|^2)}{(1 - \alpha|t|)^2} \quad (3.8)$$

It is seen from (3.7) that when the term representing transmission past the ring, t , is equal in magnitude to the field remaining after a round trip in the ring, α , then (3.7) is equal to zero and there is no light output from the device. Borrowing the term from microwave optics, this condition is known as *critical coupling*.

The maximum and minimum values of T in (3.5) are

$$T_{max} = \frac{(\alpha + |t|)^2}{(1 + \alpha|t|)^2} \quad T_{min} = \frac{(\alpha - |t|)^2}{(1 - \alpha|t|)^2} \quad (3.9)$$

To minimize T_{min} , critical coupling $\alpha \approx t$ must be satisfied. To simultaneously maximize T_{max} , the resonator should be weakly coupled to the ring and the round trip loss must be low, that is, $\alpha \approx t \approx 1$.

Shown in Figure 3.2 are plots of (3.5) for several values of t and α as stated in the caption. The critical coupling conditions are satisfied in each plot for the curve representing $|t| = \alpha$. When the magnitude of the transmission term t is larger than the loss term α , the response is termed *under-coupled*. The opposite case, when $|t| < \alpha$, refers to an *over-coupled* system.

The optical filter response of the ring resonator is a periodic array of notches, occurring for wavelengths resonant with the ring, i.e., for wavelengths λ_m that satisfy $\theta = \beta L = 2m\pi$ (assuming $\theta \gg \phi_t$). The separation between successive resonances, each occurring for mode number $m = \frac{n_{eff}(\lambda_m)L}{\lambda_m}$, is the *free spectral range* ($FSR \equiv \lambda_{m+1} - \lambda_m$). To calculate the *FSR*, subtract two adjacent resonance

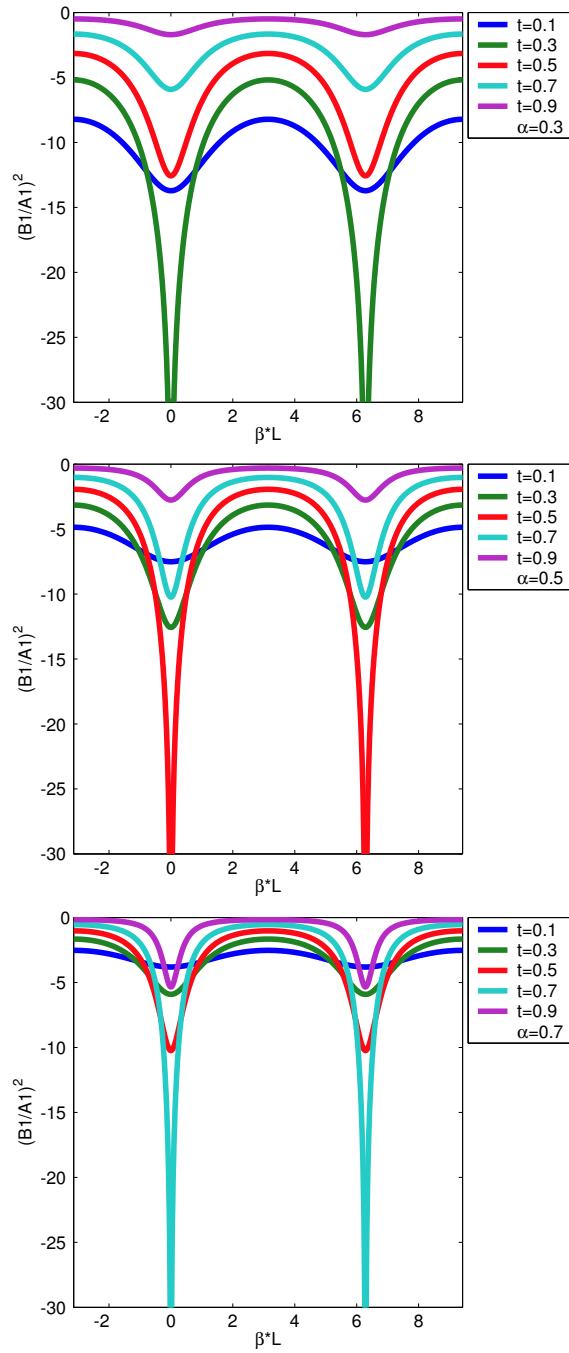


Figure 3.2: The output power of a single ring resonator coupled to a waveguide. Each plot shows the spectra with $t = 0.1, 0.3, 0.5, 0.7$ and 0.9 . The upper, middle, and lower plots represent spectra with $\alpha = 0.3, 0.5$ and 0.7 , respectively.

mode numbers

$$m = \frac{n_{eff}(\lambda_m)L}{\lambda_m}, \quad m + 1 = \frac{n_{eff}(\lambda_{m+1})L}{\lambda_{m+1}} \quad (3.10)$$

to eliminate m . Solving for $\lambda_{m+1} - \lambda_m$ gives the *FSR*. Over a large range of wavelengths, the propagation constant is not strictly constant due to waveguide dispersion. To account for this, the group index N is used rather than the effective index. The group index is given by

$$N \equiv \frac{d\beta}{dk} = n_{eff} + k \frac{dn_{eff}}{dk} = n_{eff} - \lambda \frac{dn_{eff}}{d\lambda} \quad (3.11)$$

Taking $n_{eff}(\lambda_m) \approx n_{eff}(\lambda_{m+1}) \approx N$ and $\lambda_m \cdot \lambda_{m+1} \approx \lambda^2$, the result is

$$FSR = \lambda_{m+1} - \lambda_m \approx \frac{\lambda^2}{NL} \quad (3.12)$$

The wavelength selectivity of the filter is characterized by the quality factor – or Q factor – of the resonator. Fundamentally, the Q factor is defined as the radian frequency multiplied by the ratio of the stored energy and the power dissipated in the resonator [1]. The Q can be calculated from the measured data by using the relation

$$Q = \frac{\lambda_0}{\Delta\lambda_{FWHM}} \quad (3.13)$$

where λ_0 is the center wavelength of the resonance and $\Delta\lambda_{FWHM}$ is the full width of the response curve at the half-maximum points. A related quantity often quoted for similar purposes is the finesse (F) of the filter, defined as

$$F = \frac{FSR}{\Delta\lambda_{FWHM}} \quad (3.14)$$

For the specific case of a single ring resonator coupled to a single waveguide, the quality factor and finesse are calculated as follows:

The output transmission given in (3.5) can be rewritten in the form

$$T = 1 - \frac{(1 - \alpha^2)(1 - |t|^2)}{(1 - \alpha|t|)^2 + 4\alpha t \sin^2\left(\frac{\theta}{2}\right)} \quad (3.15)$$

The right hand term in the above equation is exactly the same form as the transmission of a Fabry-Perot cavity [48], with the end-mirror reflectivities replaced by t and α . The full spectral width at half-maximum transmission, $\Delta\lambda_{FWHM}$, for the Fabry-Perot cavity is [49]

$$\Delta\lambda_{FWHM} = \frac{\lambda_0^2}{NL} \left(\frac{1 - \alpha|t|}{\pi\sqrt{\alpha|t|}} \right) \quad (3.16)$$

where the reflectivities have been replaced by α and t . An assumption used in the calculation of (3.16) was that the mirrors are highly reflecting (or, in our case, that the waveguide was weakly coupled to the resonator), as manifested in the small-angle approximation $\sin(\theta) \approx \theta$. Since, for a normalized function, the FWHM of the function is equal to the FWHM of one minus this function, we take the Fabry-Perot results for finesse and quality factor, and directly apply them to the ring resonator filter. Thus, from (3.13), the Q of the ring resonator filter is

$$Q = \frac{NL}{\lambda_0} \left(\frac{\pi\sqrt{\alpha|t|}}{1 - \alpha|t|} \right) \quad (3.17)$$

The finesse F is therefore

$$F = \frac{\pi\sqrt{\alpha|t|}}{1 - \alpha|t|} \quad (3.18)$$

Another common geometry involving a single ring resonator is shown in Figure 3.1(b). In this case, two waveguides are coupled to the ring rather than one waveguide. For analysis, from the point of view of the first waveguide, the second waveguide merely acts as another loss mechanism. The preceding equations are valid for this case if we substitute $\alpha|t_2|$ for α and $|t_1|$ for $|t|$ [47]. The transmission

function then becomes [50]

$$T = \left| \frac{B_1}{A_1} \right|^2 = \frac{\alpha^2 |t_2|^2 + |t_1|^2 - 2\alpha |t_1| |t_2| \cos(\theta + \phi_{t_1} + \phi_{t_2})}{1 + \alpha^2 |t_1|^2 |t_2|^2 - 2\alpha |t_1| |t_2| \cos(\theta + \phi_{t_1} + \phi_{t_2})} \quad (3.19)$$

The power exiting the device from the lower left waveguide in Figure 3.1(b) is [50]

$$P_{drop} = \frac{\alpha^2 (1 - |t_1|^2) (1 - |t_2|^2)}{1 + \alpha^2 |t_1|^2 |t_2|^2 - 2\alpha |t_1| |t_2| \cos(\theta + \phi_{t_1} + \phi_{t_2})} \quad (3.20)$$

This is referred to as the *drop port* of the device, because for wavelengths resonant with the ring, light exits this port rather than the *through port* denoted by B_1 . To get the full input power output from the drop port, two conditions must be met. First, the internal loss of the ring must be small, such that $\alpha \approx 1$. Second, the couplers must be identical $|t_1| = |t_2|$.

It follows that the wavelength FWHM of the add/drop filter is similar to the above, but with the replacement of $\alpha|t_2|$ for α and $|t_1|$ for $|t|$:

$$\Delta\lambda_{FWHM} = \frac{\lambda_0^2}{NL} \left(\frac{1 - \alpha|t_1||t_2|}{\pi\sqrt{\alpha|t_1||t_2|}} \right) \quad (3.21)$$

This results in a quality factor given by

$$Q = \frac{NL}{\lambda_0} \left(\frac{\pi\sqrt{\alpha|t_1||t_2|}}{1 - \alpha|t_1||t_2|} \right) \quad (3.22)$$

and therefore the finesse for the two-waveguide ring resonator filter is

$$F = \frac{\pi\sqrt{\alpha|t_1||t_2|}}{1 - \alpha|t_1||t_2|} \quad (3.23)$$

The quality factors and finesesses discussed above were the so-called *loaded* values, referring to the fact that the quantities included the power decay due to the coupling to the waveguides in addition to the intrinsic power decay due to waveguide loss. A more fundamental property of the resonator often quoted is the *unloaded* Q . For this case, the coupling terms $|t_{1,2}|$ are set equal to one, simulating the case in which there are no coupling waveguides present. The unloaded quality

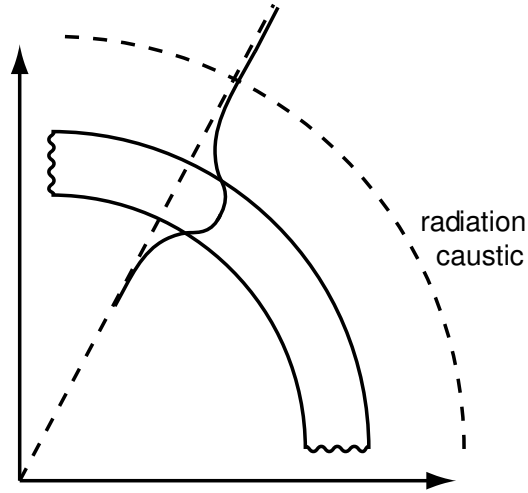


Figure 3.3: A curved waveguide section with the first order mode illustrated. The radiated field is on the constant phase line beyond the radiation caustic.

factor is then

$$Q = \frac{NL}{\lambda_0} \left(\frac{\pi\sqrt{\alpha}}{1-\alpha} \right) \quad (3.24)$$

for both the single and dual waveguide configurations.

3.2.2 Radiation Loss in Bent Waveguides

A curved waveguide results in power attenuation due to the leakage of light around the bend [51]. It is a fundamental issue when designing any type of integrated optical structure, but it is an especially important design consideration for microring resonators. As shown in the previous section, the intrinsic loss of the ring resonator is a crucial factor in achieving critical coupling, and hence in achieving proper filtering characteristics. Further, it is the internal loss of the ring resonator that determines the wavelength selectivity of the filter, given by the quality (Q) factor.

The physical mechanism responsible for bend loss is described by a simple model [36, 51]. In Figure 3.3, a curved section of waveguide is shown, along with a schematic of the first order mode intensity. From basic considerations, the phase

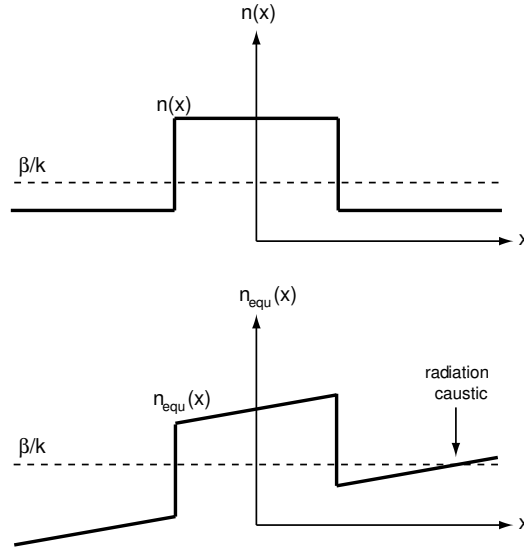


Figure 3.4: Slab waveguide refractive index profile $n(x)$ and corresponding equivalent refractive index profile $n_{equ}(x)$.

velocity of light in the guided mode must not exceed the speed of light in the bulk material. The constant phase line is shown as the dashed line from the origin outward. Further from the origin on the equiphase line, the phase velocity increases. The radius at which the phase velocity increases beyond that of the guided mode is called the *radiation caustic*, as illustrated in Figure 3.3. The field that lies beyond this radius is lost in the form of radiation, as it must disassociate from the guided field so as not to achieve $v_{phase} > v_{bulk\ cladding\ material}$. Physically, the mode does not distort, as the radiated portion of the field essentially “detaches” and the field constantly “heals” to retain its modal shape while radiating power outward.

The refractive index profile of a curved waveguide can be approximated by a straight waveguide with a modified refractive index profile due to the curved coordinate system. The modification is manifested in a conformal transformation [52]. In its simplest form, the transformation is of the form

$$n_{equ}(x) = n(x) \sqrt{1 + \frac{2x}{R}} \quad \text{for } x \ll R \quad (3.25)$$

where $n_{equ}(x)$ is the transformed equivalent index profile of the original index profile $n(x)$ at a position x in a curved system with radius of curvature R . The linear transformation is valid for large radii of curvature.

Shown in Figure 3.4 are the refractive index profile of the original curved structure, along with the equivalent index profile of the straight, transformed coordinate system. For light to be guided, the propagation constant obeys the relation $n_{clad} < \beta/k_0 < n_{core}$. Where $n_{clad} > \beta/k_0$, the light is radiated. The radiation caustic is the point for which the equivalent index becomes larger than β/k_0 , and thus, represents the location of the onset of radiation.

An accurate and simple scheme to numerically predict the attenuation of the propagating power in curved waveguides was developed by Marcuse [53]. The decay of the intensity in the waveguide after propagating a distance z is assumed to have the form

$$I = I_0 e^{-\alpha z} \quad (3.26)$$

By calculating the fields in curved waveguides in terms of Hankel functions and finding the power carried in these fields, an approximation for the attenuation coefficient is found to be [53]

$$\alpha = \frac{ph^2 e^{wp} e^{-U}}{(n_{core}^2 - n_{clad}^2) k_0^2 \beta (w/2 + 1/p)} \quad (3.27)$$

where

$$U = \left[\frac{\beta}{p} \ln \left(\frac{1 + p/\beta}{1 - p/\beta} \right) - 2 \right] pR \quad (3.28)$$

and $h = \sqrt{k_0^2 n_{core}^2 - \beta^2}$, $p = \sqrt{\beta^2 - k_0^2 n_{clad}^2}$, w is the waveguide width, and β is the propagation constant.

In Figure 3.5, we show the bend loss as calculated from (3.27) and (3.28). The core refractive index is taken to be a constant 1.60 while the cladding refractive index takes the values 1.45, 1.50, and 1.53. Clearly, the bend loss is very sensitive to refractive index differences and higher index contrast results in lower losses for a given radius. The curves exhibit the characteristic “elbow” at which the bend

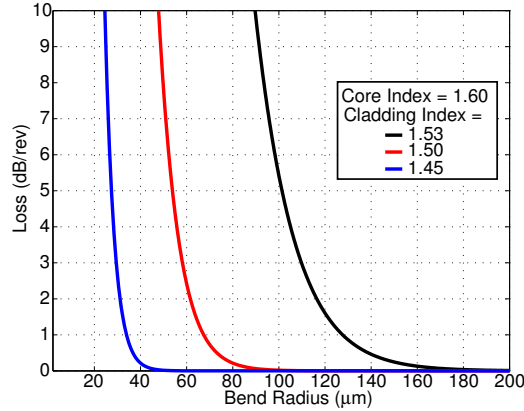


Figure 3.5: Typical “elbow” curves of bend loss for several cladding refractive indexes ($n_{clad}=1.45, 1.50, 1.53$) and fixed core index ($n_{core}=1.60$).

loss becomes small for some radius. Beyond this radius, the bend loss is generally negligible, but for radii smaller than this “elbow” value, the bend loss is a very strong function of radius.

An earlier, three dimensional analysis of bend loss due to Marcatili [39], concludes some important qualitative results. The analysis compares waveguides with widths less than, comparable to, and larger than, the thickness. The conclusion is that waveguides with widths larger than the thickness result in reduced bend losses. This is intuitive, as waveguides with less width have more field outside of the core and thus, more power at the radiation caustic. The reduction in bend loss, however, is found only for widths up to

$$w \sim \left(\frac{r\lambda_0}{\pi n_{core}^2} \right)^{1/3} \quad (3.29)$$

3.2.3 Waveguide Surface Scattering Loss

A significant source of loss for both bent and straight waveguides is due to surface scattering. Since, as shown in Chapter 2, three dimensional waveguide systems can be reduced to equivalent slab waveguide systems, we consider the surface scattering of the slab waveguide system dealt with in Section 2.2.2. In the ray-

optics picture of a slab waveguide, as propagating light reflects off of the interfaces, it has associated with each reflection a loss determined by the Rayleigh criterion. The expression for the Rayleigh criterion states that an incident beam with power P_i results in a specularly reflected beam with power

$$P_t = P_i \exp \left[- \left(\frac{4\pi\sigma}{\lambda} \cos(\theta'_m) \right)^2 \right] \quad (3.30)$$

where σ is the root mean square (RMS) surface roughness, λ is the wavelength in the core, and θ'_m is the compliment of the propagation angle (that is, $\theta_m = \arccos(\beta/k_0 n_{core})$ and $\theta'_m = \pi/2 - \theta_m$). Based on this simple expression, the surface scattering loss can be expressed as [54]

$$\alpha_{scattering} = A^2 \left(\frac{\cos^3 \theta'_m}{2 \sin \theta'_m} \right) \left(\frac{1}{t + (1/q) + (1/p)} \right) \quad (3.31)$$

where t is the waveguide width, and q and p are the extinction coefficients as given for the slab waveguide in Section 2.2.2. The coefficient A is a composite RMS surface roughness given by

$$A = \frac{4\pi}{\lambda} \left(\sigma_{12}^2 + \sigma_{13}^2 \right)^{1/2} \quad (3.32)$$

for the surfaces of the slab waveguide. To convert the loss from inverse centimeters to dB/cm, (3.31) is multiplied by 4.343.

It is clear from (3.31) that the loss is proportional to the square of the RMS surface roughness, given by A , and thus, smoother waveguides result in less scattering loss. The loss is also inversely proportional to the waveguide thickness plus the terms $1/q$ and $1/p$. This results in decreased scattering from thicker waveguides as there are smaller field tails at the interfaces for thicker waveguides. From numerical investigations, the loss goes approximately as t^{-3} [55]. The refractive index contrast of the waveguide core to the cladding materials also has a significant effect on the scattering loss since the contrast also determines how well the field is confined. Given an index contrast $\Delta n = (n_{core} - n_{clad})$, the loss is found to

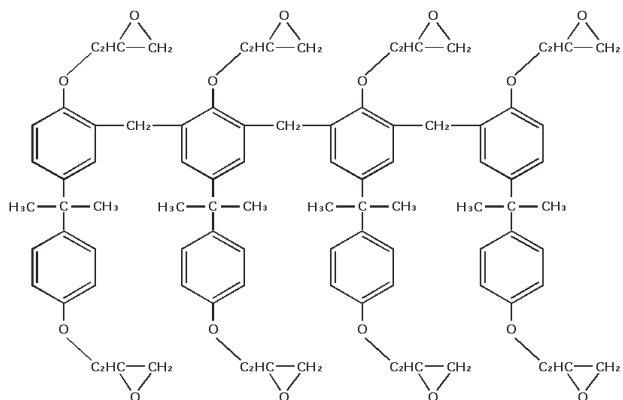


Figure 3.6: The chemical structure of the SU-8 molecule showing the eight epoxy groups.

be proportional to $(\Delta n)^2$ [55]. Lastly, higher order modes are susceptible to more scattering loss because higher order modes are characterized by smaller θ'_m .

3.3 Passive Polymer Planar Optics Using SU-8

SU-8 (Microchem Corp.) is a negative-tone epoxy-based resist that can be cured by exposure to ultraviolet radiation (365 nm), an electron beam, or X-ray radiation. The chemical structure of the base epoxy EPON SU-8 developed by Shell Chemical Company is shown in Figure 3.6. As a resist, SU-8 was developed by IBM-Watson Research Center in 1989 [56]. The high functionality of its eight epoxy groups is responsible for its high sensitivity as a resist, and the low molecular weight results in extremely high resolution. To formulate as a resist, the EPON SU-8 resin is first dissolved in either gamma-butyrolactone or cyclopentanone [57]. Subsequently, a photoacid generator, in the form of triarylsulfonium hexafluoroantimonate salt, is added to the solution. Upon exposure, the photoacid generator decomposes to an acid activating the epoxy groups and enabling polymerization with other activated epoxy groups. Thus SU-8 exhibits the negative-tone property that the exposed material remains, whereas unexposed material is removed upon developing in the appropriate solvent. This is in contrast to polymethylmethacrylate

(PMMA), a positive-tone resist that when exposed to beam of energetic electrons undergoes scission of the polymer backbone and the material in the exposed areas are subsequently removed by developing in solvent.

SU-8 is widely used as a resist because of its remarkable properties in comparison to other commercially available resists. By varying the solid/solvent ratio and hence, varying the viscosity, single spin film thicknesses can be attained from the sub-micron level up to the millimeter level. Very good transparency for wavelengths longer than ~ 360 nm allows for high aspect ratio structures with near-vertical sidewalls. High resolution patterns are possible with as low as sub-50 nm features because of the low initial molecular weight of pre-polymerized SU-8 [58]. The high functionality of the epoxy groups produces extremely high sensitivity, such that very low photon or electron fluences are needed for crosslinking. The electron beam exposure required to crosslink is on the order of 100 times less than what is needed to expose PMMA. Further, the high functionality and number of epoxy groups provides a high level of crosslinking. This very dense three-dimensional crosslinked network results in a comparatively high glass-transition temperature of $T_g \sim 200^\circ\text{C}$ and degradation temperature of $\sim 380^\circ\text{C}$. There are no known chemical solvents that dissolve cured films of SU-8 predictably and reproducibly. Clearly, the chemical resistance of cured SU-8 is very good.

The preceding properties of SU-8 contributed to extensive use in the fabrication of micro-electromechanical systems (MEMS) devices, as well as the production of micro-fluidic devices. Recently, however, SU-8 has proven to be a useful material for planar integrated optics devices. One of the earliest implementations of SU-8 for integrated optics is Reference [59], in which several optical properties were investigated. The refractive index of an SU-8 film illuminated with 1550 nm light was found to be 1.575. This value is higher than most other polymer materials typically used for cladding layers, and ensures good optical confinement. Waveguides with cross sections $6\ \mu\text{m}$ by $1.8\ \mu\text{m}$ were fabricated with SU-8 core material, with Norland epoxy NOA61 as the lower cladding, and either air or NOA61 as the upper cladding. Cut-back loss measurements resulted in propagation loss

values of 0.41 dB/cm and 0.49 dB/cm for air-clad propagation at 1310 nm and 1550 nm, respectively. When similar waveguides are measured with NOA61 upper cladding, the propagation losses reduce to 0.22 dB/cm and 0.48 dB/cm at 1310 nm and 1550 nm, respectively. These figures are commensurate with measurements of other polymer core materials. As for environmental degradation, the authors report negligible changes in propagation loss after 200 hours at 90 °C and 95% relative humidity.

Electron beam lithography has been applied as one of the most effective methods for modern micro- and nano-fabrication. Electron beam lithography utilizes the effect that some materials such as SU-8 resist will undergo chemical changes when exposed to a beam of energetic electrons such as that described in the preceding paragraphs. Since the diameter of a well-collimated electron beam is typically much smaller than the diffraction limited spot of UV light, this method has an inherent advantage over photolithography. Electron beam lithography has made it possible to fabricate high-resolution devices impossible to make by photolithographic techniques. Single-mode integrated optic structures typically have cross-section dimensions on the order of micrometers and minimum features on the nanometer scale. Fabrication on these scales is routine for electron beam lithography, but is near the limit of photolithography and requires an optimized system. Where photolithography has an advantage over electron-beam lithography is in throughput; that electron-beam lithography must be carried out in a high-vacuum environment causes the method to be much more time consuming as compared to photolithography.

Shown in Figure 3.7 are scanning electron micrographs of waveguides fabricated by optimized electron beam lithography of SU-8. The substrate material is thermally grown silica (6 μm thick) on silicon. The fabrication method of such waveguides is extraordinarily simple. A layer of SU-8 is spun onto the substrate at a thickness of $\sim 1.5 - 2 \mu\text{m}$. The thickness versus spin speed for a given solution of SU-8 can be calibrated by spinning at various rates, curing with exposure to a UV-lamp, and measuring the depth of fully scratched away section with a stylus

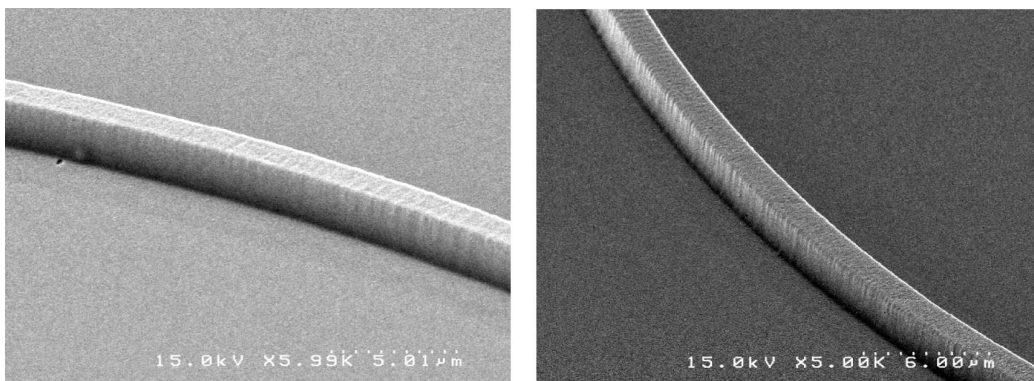


Figure 3.7: Scanning electron microscope images of SU-8 waveguides fabricated by direct electron beam exposure of the core.

profilometer. This type of calibration must be done for each new polymer solution, and for the same polymer solution every few weeks, as small quantities of evaporated solvent result in large differences in the calibration curve. Once the desired film thickness is achieved, the chip is baked at approximately 90°C for approximately one minute to remove any residual solvents. Electron beam lithography is performed, with the electron beam tracing out a path predetermined in the lithography software. The electron beam dosage is an extremely critical quantity to generate good quality structures. This again must be individually calibrated for the particular lithography apparatus. The appropriate dosage can be distinguished from too high of a dose by observation of “shoulders” surrounding the exposed structures indicating overexposure. These “shoulders” result from electrons scattered at the substrate surface impinging on surrounding material and crosslinking areas not intended. A low dosage is indicated by less than full height of the exposed area. For instance, if an initial $2\ \mu\text{m}$ film results in $1\ \mu\text{m}$ features, this is an indication of underexposure. Once the appropriate exposure conditions are obtained, the structures are exposed by the sweep of the electron beam and the chip is removed. Convention suggests a post-exposure bake at approximately 90°C for approximately 1 minute to fully crosslink the exposed SU-8. However, structures similar in character have been fabricated both with and without this post-

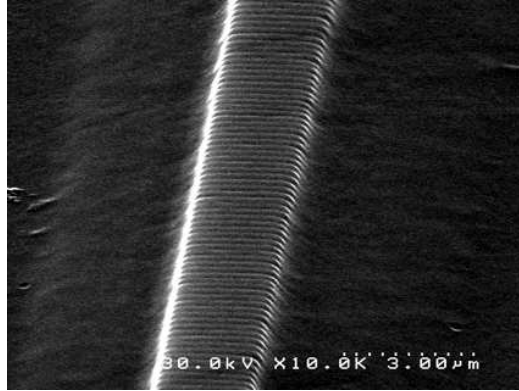


Figure 3.8: A waveguide grating fabricated by direct electron beam exposure of SU-8.

exposure bake. If anything, the post-exposure bake results in further crosslinking and structures that appear as if overexposed. The structures are then developed by immersing the chip in propylenglycol-monomethylether-acetate (PGMEA) for approximately 2 minutes, followed by immersion in isopropyl alcohol (IPA). If in the IPA step, any white or milky substance appears, the develop step was not fully achieved and must be repeated.

As discussed, the optical properties of SU-8 make it an attractive material for polymer integrated optics applications. Beyond these optical properties, SU-8 is unique because the patterning is performed directly on the core material. This is in contrast to the more typical fabrication procedure for polymer integrated optics. More typically, a photoresist to be patterned is spun atop the polymer core material, and then the pattern is transferred to the underlying optical core using reactive ion etching (RIE). This method adds several more time-consuming steps on several apparatus, not to mention opportunities for fabrication errors. Since the core is patterned directly using SU-8, the fabrication is extraordinarily rapid. Given a CAD drawing of the desired pattern, a passive SU-8 device can be fabricated from start to finish in approximately one hour. This incredible speed enables rapid prototyping and less overall time for the numerous iterations necessary in optical device research and development.

Since the direct fabrication of SU-8 waveguides can be performed with either UV lithography, or with electron beam lithography, the process can be tailored to the desired speed or device resolution. If high-throughput fabrication is the premium quality in the fabrication, large areas of SU-8 can be patterned to produce hundreds of devices in parallel. However, the resolution of UV lithography is limited. In this case, electron beam lithography is employed to make devices otherwise impossible using UV lithography. For instance, waveguides with surface corrugations such as that shown in Figure 3.8 are useful as Bragg grating wavelength filters. An surface grating wavelength filter was fabricated in SU-8 and measured to have up to -27 dB extinction of the rejected wavelength in Reference [60]. Surface gratings are made in SU-8 by setting the spacing of consecutive raster lines of the electron beam to the desired corrugation spacing. This spacing is easily calculated as $\Lambda = \lambda_{Bragg}/(2n_{eff})$, where Λ is the grating period, λ_{Bragg} is the reflected wavelength in free space, and n_{eff} is the waveguide group index. The high resolution lithography possible with electron beam lithography is useful not only for Bragg grating devices. Optical couplers as discussed in Chapter 2 require careful control of the coupling constant to achieve the desired coupling ratio. This coupling ratio is determined by the separation between the coupled waveguides and is typically on the order of hundreds of nanometers. Therefore, to achieve the critical coupling condition for a ring resonator coupled to a waveguide, it is highly advantageous to use electron beam lithography to precisely set the coupling to match the ring round-trip loss.

3.4 Polymer Microring Resonators

The microring resonator structure is one of the most useful integrated optics elements with several applications. For instance, when doped with luminescent dyes, polymer microring resonators can be optically pumped to exhibit lasing [61, 62, 63, 64]. The key feature is the dramatic modification of the spontaneous emission due to the resonant characteristics of the microring. In addition to lasing, when

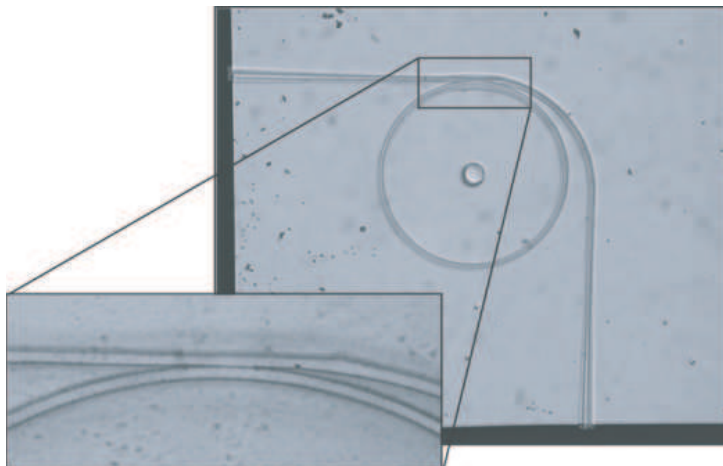


Figure 3.9: An early example of a microring resonator optical filter fabricated in SU-8 by direct electron beam writing.

evanescently coupled to a waveguide as described in Section 3.2, a passive microring resonator acts as an optical filter. The frequency response is typified by a periodic sequence of narrow notches, acting as a highly selective frequency rejection filter. Although several polymeric microring lasers have been produced during the past few years, the studies of polymer microring resonator optical filters have been limited. The limiting factors have been overcoming the high propagation loss figures typically associated with polymer core materials, and the ability to precisely fabricate low scattering loss waveguides and good quality, controllable waveguide-to-ring couplers.

As alluded to in the previous section, the properties of SU-8 provide an enabling technology toward rapid fabrication of highly precise optical integrated circuits. This provides a good platform for the fabrication of polymer microring resonator devices. Shown in Figure 3.9 is an example of one such device. The fabrication was done by direct electron beam lithography of SU-8 on a substrate consisting of lower cladding silica, thermally grown atop a piece of silicon wafer. The waveguides end-facets were prepared by cleaving the silicon substrate. Because of the good adhesion between the polymer material and the silica, the core polymer shears

at the location of the silicon wafer cleave. Scanning electron microscope (SEM) images reveal shear planes of the waveguide input/output parallel to the cleavage planes, with smooth faces to within the resolution of the SEM. The resulting waveguide end facets provide – albeit not optimal – reasonably good input and output coupling efficiencies for device interrogation.

The polymer ring has a radius of $100\ \mu\text{m}$ that with air cladding assures negligible bending loss. The core cross section is approximately $2\ \mu\text{m}$ in thickness and width to provide a single transverse waveguide mode in the resonator.

The measurement setup is typical of standard integrated optical device measurement apparatus. After passing through a polarization controller, light from a tunable laser was input to the waveguide via commercially available (Oz Optics) tapered and lensed SMF-28 optical fibers. The spot size of the tapered and lensed fiber was specified to be $1.5\ \mu\text{m}$ by $3\ \mu\text{m}$ to ensure good modal overlap and thus good coupling efficiency. A microscope was used to align the input tapered fiber to the polymer waveguide using five-axis stages. The output waveguide end-facet was focused on an infrared CCD camera for viewing, or on a photodetector for measurement. A computer GPIB controller stepped the laser through wavelength and recorded the voltage output from the photodetector at each wavelength step.

The spectral output of the SU-8 polymer microring resonator is shown in Figure 3.10. As predicted by the preceding theory, the output spectrum is characterized by a periodic series of notches. The maximum extinction ratio shown in the inset is approximately -22 dB. This indicates that the critical coupling condition was achieved to a high degree of precision. This is a testament to the ability of direct electron beam writing to fabricate precise gaps. The wide spectral data shows that the extinction ratio does not change very much over a wide wavelength range. This indicates that the coupling between the ring and waveguide is relatively immune to variations in wavelength and that the polymer waveguides have little dependence of loss on the wavelength.

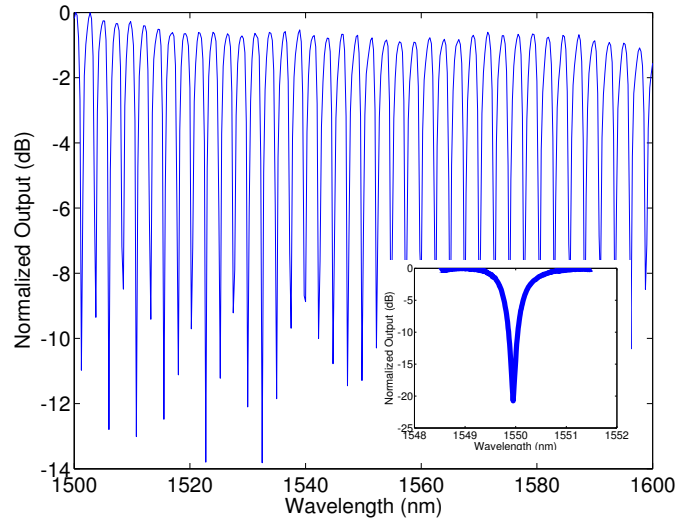


Figure 3.10: The measured output spectrum for the microring resonator depicted in Figure 3.9.

3.5 Freestanding All-Polymer Optical Devices

Electronic integrated circuits (EICs) face fundamental material and fabrication limitations which are hindering to their future use in high-speed telecommunications, optical networking and optical computing. Alternatively, optical integrated circuits (OICs) are currently receiving more attention for potential use for these and other applications. The materials for advanced OICs will not be limited to semiconductors. Foremost among the new materials, polymers are becoming increasingly important for OIC applications because their optical, mechanical and functional properties can be broadly tuned by changing their chemical structures through molecular design and proper synthesis procedures. During the past two decades, significant progress was made in polymer materials for OIC applications [4, 65]. Recently, for example, electro-optic polymer materials with highly active nonlinear-optical chromophores have been proven to be excellent for use in optical modulator devices [12, 13, 66]. However, compared with common materials used today for OIC devices (most of which are semiconductor and inorganic single crystals), polymer materials are not only highly-efficient and low-cost, but

also mechanically flexible. This flexibility is one of the distinct advantages over other materials, making it possible to make pliable and transparent all-polymer devices, and to reshape the devices by adhering to non-flat surfaces for special purposes. Recently, Larsen et al. [67] have used soft-lithography to make freestanding polymeric structures proposed as waveguides, while Steier et al. [68] described a method to lift off a thick (> 100 nm) and long section (> 2 cm) of flexible modulator from a solid substrate.

In the following section, we demonstrate a simple method to fabricate thin free-standing all-polymer OIC devices and their successful transfer to various substrates such as curved glass surfaces of capillary tubes. We also demonstrate a passive microring resonator optical filter device with a -27 dB notch extinction for certain wavelengths in the telecommunication band (~ 1.55 μm), which is the best value reported in similar polymer devices and is within the range of the requirements for practical telecommunications applications. By utilizing the poor adhesion between the lower cladding polymer and gold, we can easily peel off a very thin layer several square centimeters in extent containing a large number of all-polymer OIC devices, and with a total thickness of less than 10 μm . Surprisingly, the end-facets of the OIC devices can be easily cut by normal scalpel blades yielding good optical quality inputs and outputs. Each device, or the film of several devices, can also adhere to many different types of surfaces by heating while the optical properties are minimally changed. This last point is possibly the most significant aspect of freestanding all-polymer OIC devices, setting them apart from their crystalline counterparts.

3.5.1 Fabrication

Figure 3.11 shows the schematic diagram of the complete procedure of making free-standing OIC devices. A very thin layer of Cr (~ 5 nm) is evaporated onto the freshly cleaned silicon wafer to improve the adhesion between Au (300 nm) and silicon. UV15 (Masterbond), an optically clear UV curable epoxy with low refractive index (1.504 at 1550 nm), is applied as the lower cladding layer of thickness 6 μm .

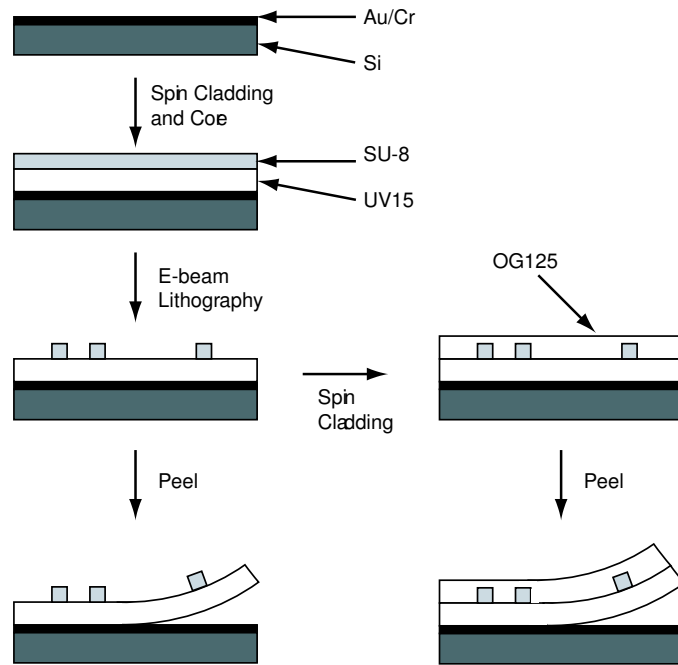


Figure 3.11: Schematic fabrication procedure for freestanding polymer integrated optical devices. For clarity, the thicknesses are not drawn in proportion to the real device.

A $2\ \mu\text{m}$ thick SU-8 core layer is spin coated and exposed by electron beam using a scanning electron microscope (SEM). The structure is dried, without post-baking, by nitrogen gas after being developed by propylene glycol monomethyl ether acetate. Using the previously mentioned weak adhesion between the UV15 lower cladding layer and the gold, a film of several structures can be easily peeled off from the substrate. To protect the optical devices from contaminants or to meet refractive index requirements for the optics, we can also apply an upper cladding polymer, OG125 (Epotek, refractive index 1.456 at 1550 nm).

To be useful in OIC applications, the waveguide sections of the devices must have input and output end-facets of good optical quality, exhibiting low optical loss and good interconnection coupling. Typical of polymer OIC devices that are left on the silicon substrate, the end-facets are prepared by dicing the silicon substrate and the polymer with a semiconductor saw, and polishing the end-facets

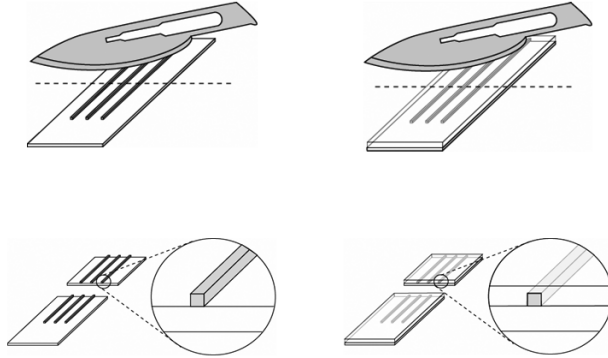


Figure 3.12: Preparation of freestanding all-polymer optical device end-facets using scalpel blades.

to produce good optical quality interfaces. An added complication is that the polymer waveguides must be protected from the by-products of the dicing and polishing by the use of an encapsulating polymer. Clearly in the case of the films produced by our procedure, there is no substrate to be diced, although dicing or cleaving the substrate before peeling off the optical devices is possible, but only one device can be put on each substrate. To solve the difficulty of preparing the end-facets of the freestanding polymer waveguides, we find that a simple but effective method is to cut through the film using normal scalpel blades. As shown in Figure 3.12, both air clad devices and those with polymer upper cladding layers can be cut easily using scalpel blades. Using optical measurements and SEM observations, we find that the end-facets of the polymer waveguides cut in this fashion are of good optical quality. In principle, one can envision cutting and reassembling polymer optical components to form reconfigurable OICs.

We show in Figure 3.13 several optical microscope images of our model structures with freestanding polymer films prepared using the method described above. In Figures 3.13(a) and 3.13(b), we show a passive microring and microdisk still on the substrate. Films containing several of these structures are peeled up without

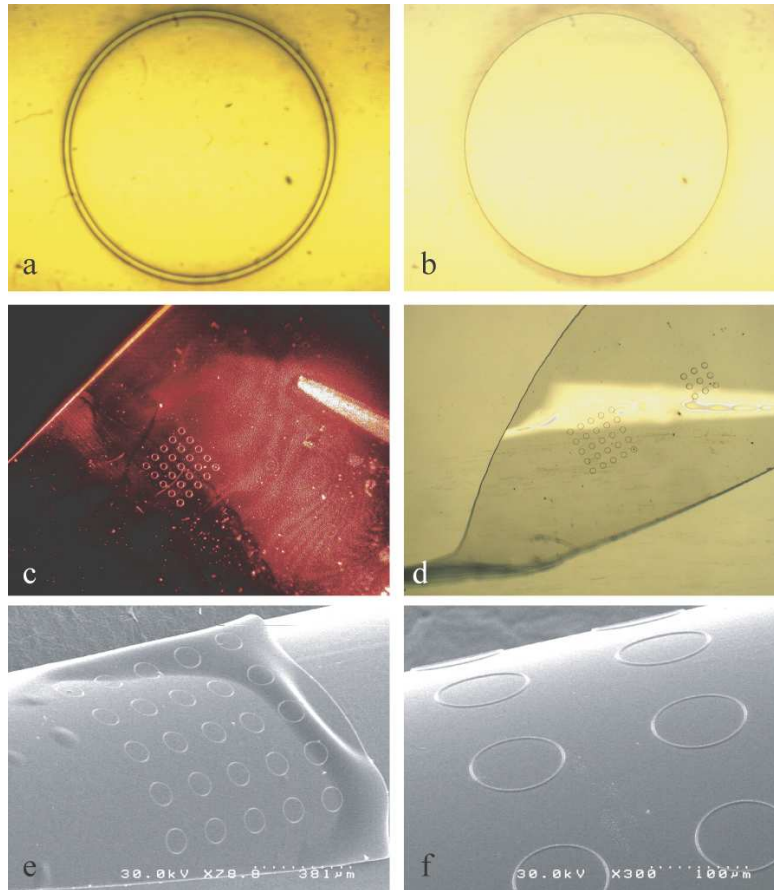


Figure 3.13: Optical microscopic images of polymeric model structures. All structures are made with SU-8 core layers on UV15 lower cladding using electron beam lithography. (a) Microring with 200 μm diameter. (b) Microdisk with 200 μm diameter with 2 μm wide waveguides. (c) Freestanding all-polymer film with a microring array, illuminated with a HeNe laser. The bright wedge is the fine tip of the tweezers used to hold the film. (d) Curved freestanding polymer film with microring array (5 by 5) and microdisk array (3 by 3). (e) and (f) All-polymer microring array on curved surface. The structures are peeled off of the substrate and reattached on a glass capillary tube (2 mm diameter) by heating.

damage and become freestanding polymer microring and microdisk arrays, as in Figures 3.13(c) and 3.13(d). Once heated to $\sim 125^\circ\text{C}$, perhaps due to localized melting of the polymer surface, the freestanding film can be adhered to surfaces of arbitrary shape or different material. Figures 3.13(e) and 3.13(f) show the examples of microring arrays adhered to the curved outer surface of capillary tubes. This way of adhering the polymer films onto arbitrary surfaces is perhaps the easiest way to make non-flat OIC devices. An important use for the adhesion of polymeric optical devices to foreign substrates lies in the potential for hybrid-material devices, i.e., with the polymer devices integrated with semiconductor lasers, or functional materials for chemical or biological sensing.

3.5.2 Measurement Results and Discussion

As previously discussed, an important application of microring resonators for wavelength-division multiplexed (WDM) systems is the conditioning and filtering of an input optical waveform. Here, we describe a high-performance microring resonator optical filter based on critical coupling between a microring and a straight side-coupled waveguide. A schematic diagram of device is presented in Figure 3.14(a). In Section 3.2, we have shown that this device can be analyzed by a transmission matrix method that describes the evanescent coupling of the optical field into the resonator, and the optical field output as the function of input wavelength. In brief, when the wavelength is such that the optical phase accumulated in a round trip of the resonator is $2\pi m$ where m is an integer, this is defined as the resonance condition of the microring. In this case, the field returning to the coupler from the ring after traversing the ring length interferes destructively with the field impinging on the coupler from the straight waveguide. If the amplitudes of the interfering fields are equal, the destructive interference is complete, and the through output of the straight waveguide vanishes. Mathematically, this complete extinction of the output occurs at wavelengths right on resonance, when α – defined as the field amplitude remaining after one round trip in the resonator – is equal to $|t|$, the field amplitude that is not coupled into the ring. This critical

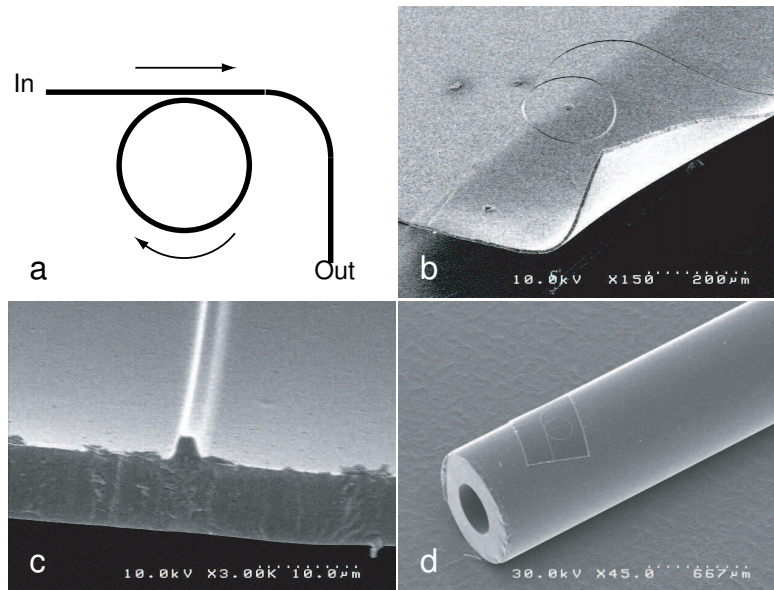


Figure 3.14: Freestanding all-polymer microring resonator optical filter. (a) Schematic diagram of a microring resonator optical filter. (b) SEM image of freestanding microring resonator optical filter, purposely curled to show the excellent flexibility. (c) SEM image of a waveguide (SU-8) and lower cladding layer (UV15). The end-facet of device is prepared by scalpel blade cutting method. (d) Polymer microring resonator optical filters on a curved surface. The devices are peeled off of the substrate and heated to adhere to small glass capillary tube (0.8 mm diameter).

coupling condition is one of the desired properties of a microring resonator based optical filter.

In our experiments, the radius of the microring resonator is designed to be $100\ \mu\text{m}$, and the width and thickness of the core waveguide $2\ \mu\text{m}$ and $2\ \mu\text{m}$, respectively. In Figure 3.14(c) we present an SEM image of the cross-section of a freestanding all-polymer waveguide end-facet as prepared by a scalpel. The end-facet of the waveguide is smooth. Note that the cross section does not appear perfectly square due to the electrons backscattered from the lower cladding material during exposure, but this does not adversely affect the optical properties of the waveguide. The total thickness of the device is about $8\ \mu\text{m}$. As in the case of the microdisk and microring arrays, we can adhere the microring optical filter to the outer surface of a glass capillary tube ($0.8\ \text{mm}$ diameter). An SEM image of this is presented in Figure 3.14(d) showing minimal change in the physical properties of the device.

The experimental measurement setup is shown in Figure 3.15. A tunable laser is employed as the source for the transmission measurements. The laser is input by a tapered/lensed fiber and coupled into one end of the polymer waveguide. The optical transmission signal emitted from the other end of the waveguide is collected by an aspherical objective lens and then focused onto an IR-CCD camera for imaging. The emitted signal intensity is measured by a femtowatt IR photodetector and acquired by a digital multimeter. All the equipment is controlled by MATLAB via GPIB interface.

The measured data is presented in Figure 3.16. One of the key characteristics for a good filter response is, among other things, high extinction of the wavelength rejection nulls in the spectral response, requiring critical coupling, $\alpha = |t|$ of the resonator/waveguide system. Since the loss parameter is set by the size and waveguiding properties of the ring, we must find the appropriate gap between the waveguide and the resonator to control $|t|$, thus achieving critical coupling. The gap needed to maximize extinction was experimentally found to be $250\ \text{nm}$. Figure 3.16, shows the measured spectral transfer function of this device in a spectral

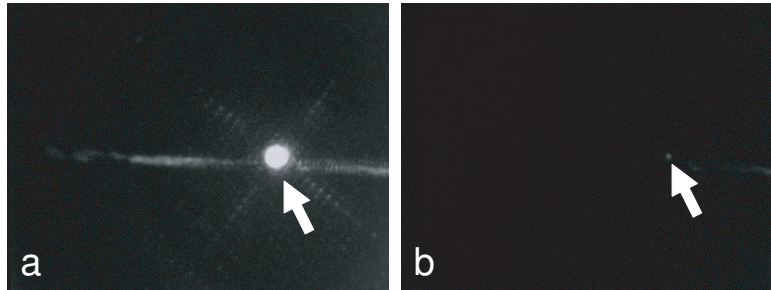
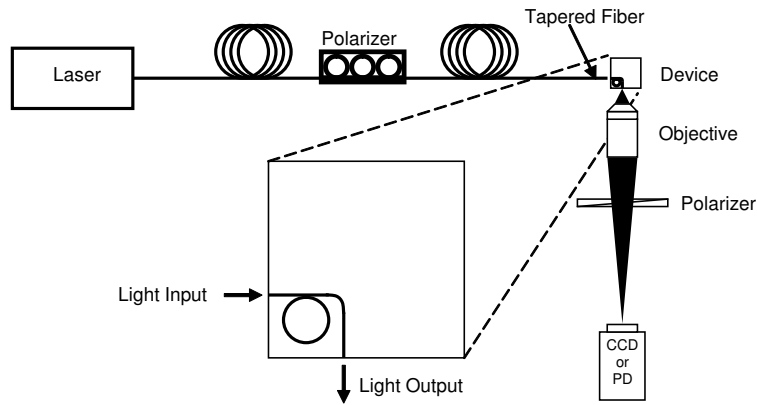


Figure 3.15: Schematic diagram of measurement setup for the microring resonator optical filter. TE-polarized laser light is coupled into the input end of polymer device via a tapered fiber, and the output optical signal was collected by an IR-CCD camera or IR photodetector (PD). The two IR-CCD images of the output light are at different wavelengths, with the arrows indicating the position of the output end of the device. In (a), the wavelength of the light is off-resonance for the microring and in (b), on-resonance.

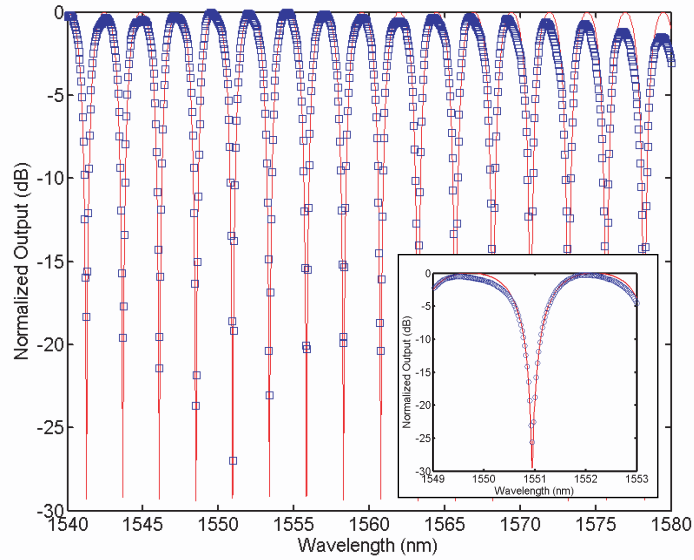


Figure 3.16: Spectral transfer function of a freestanding air-clad critically coupled microring resonator optical filter. The open square is experimental data and the line is theoretical calculation. The inset is a higher resolution measurement (open circle) around 1550 nm and theoretical calculation (line).

band which is important for optical communications. Using simple finite difference simulations (see Appendix B), we verify that for wavelengths around 1550 nm, there is only one mode that can propagate through the waveguide structure we have fabricated. By combining the effective refractive index of the single propagating mode, the size of the ring and waveguides, and the waveguide loss, we can fit the data based on matrix methods described in Section 3.2. The theoretical fit is shown as solid line in Figure 3.16 and shows excellent coincidence.

The deep notches in the measured spectral response – up to -27 dB (0.2 %) of the maximum signal – is to the best of our knowledge, the lowest value reported for any polymer ring resonator to date, whether on a substrate or freestanding. This indicates that the properties of the freestanding all-polymer optical filter are as good as can be achieved in a polymer device on a substrate. Furthermore, the

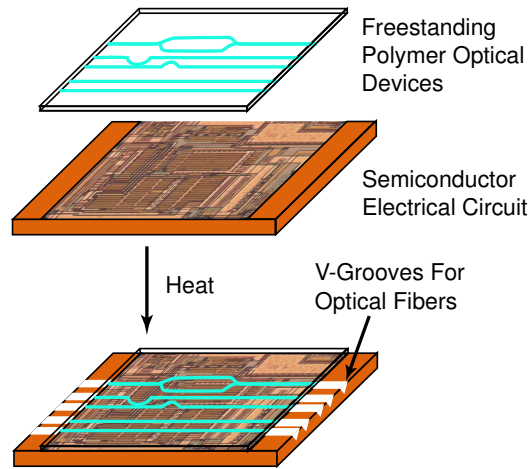


Figure 3.17: The integration of freestanding all-polymer waveguide devices with CMOS drive or trimming circuitry.

value of -27 dB of the maximum response also represents the noise floor of our measurement apparatus, i.e., the photodetector voltage measured when the laser diode is turned off relative to the maximum signal.

In summary, we have developed a novel method to fabricate freestanding flexible all-polymer integrated optical devices with total film thicknesses of less than $10\ \mu\text{m}$. A microring resonator optical filter demonstrated by this method shows the most promising results among similar reports and meets the practical rejection requirements of telecommunications systems. This method can be applied not only to devices fabricated by direct electron-beam writing as described here, but also to other fabrication methods such as photolithography and imprint techniques.

3.5.3 Potential Applications of Freestanding All-Polymer Optical Circuits

Freestanding polymer optical circuits take advantage of the most basic property of polymer material: the plastic, malleable nature of polymers. As shown in the previous section, by simply peeling the polymer waveguide films from their crystalline substrates, flexible waveguide structures are achieved. Among the myriad appli-

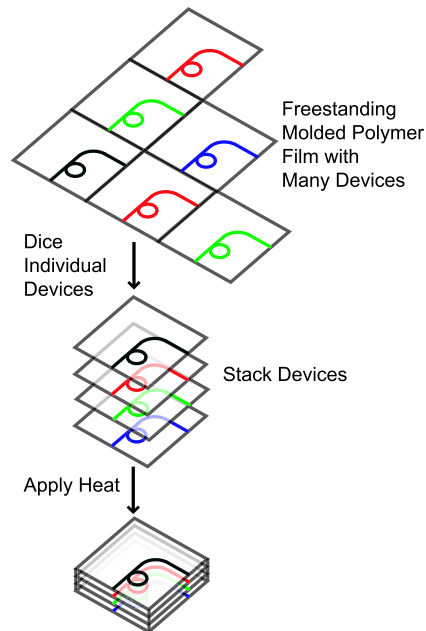


Figure 3.18: The creation of a three-dimensional densely integrated optical waveguide circuit by stacking several freestanding all-polymer waveguide devices.

cations one can envision for freestanding all-polymer optical circuits, we briefly present two such possibilities.

While polymer materials for optical devices are advocated in this thesis, the electronics used to drive or trim optical devices are fabricated in silicon using standard CMOS technology. All modulators must in some way be coupled to the drive and trim circuitry. The freestanding all-polymer optical circuits enable a unique way to achieve this coupling of optical device to drive circuitry. Shown in Figure 3.17 is a schematic diagram of how one can achieve this coupling. The initially separate devices are adhered together using the adhesion properties of the polymer material upon heating. The waveguiding film is simply aligned appropriately with the CMOS chip, and modest heat (approximately the lower cladding layer's glass transition temperature) is applied to secure the polymer film to the circuitry chip.

Another application is presented in Figure 3.18. There exists great interest in three-dimensional integration of separate optical elements, forming a sort of mul-

tilayer optical circuit board. Freestanding polymer waveguide technology allows for a simple implementation of multilayer optical devices. As shown in the figure, a single film containing the desired devices is fabricated by whatever appropriate method. This film is then diced to separate the devices into many freestanding polymer microdevices. Integration is achieved in much the same way as the previous application. The different layers are aligned as desired, and the composite structure is heated to a temperature at which the polymer becomes soft. At this point, the different layers adhere to one another and become a three-dimensional, densely packed optical waveguiding circuit.

3.6 Microring Resonator Based Reflector

Here we present a novel geometry for wavelength-selective reflectors employing microring resonators, in the spirit of References [69] and [70]. Inline reflectors – particularly fiber Bragg gratings [71] – are widely used components in optical telecommunications systems. Applications include external wavelength stabilization for lasers, gain-flattening, dispersion-compensation, and add/drop filtering. Integration of inline reflectors into planar optical circuits is important for several reasons. Integrated reflectors can be much smaller than corresponding fiber devices and can be fabricated in a variety of materials with special nonlinear functionality or with specific dispersion properties. In addition, integrated optical reflectors can be combined on a single chip with additional photonic devices such as modulators, couplers, sources, etc. However, integration of Bragg gratings within a planar waveguide optical circuit is difficult due to the high-resolution lithography required over large areas necessary to achieve high reflection efficiency and low scattering loss [72]. This is especially the case in integrated geometries requiring aperiodic gratings. An alternative to Bragg gratings for planar integrated optical inline reflectors is shown in Figure 3.19. Here, we present the design, fabrication and characterization of a microring-based inline integrated optical reflector. We discuss the potential applications and various advantages of the device.

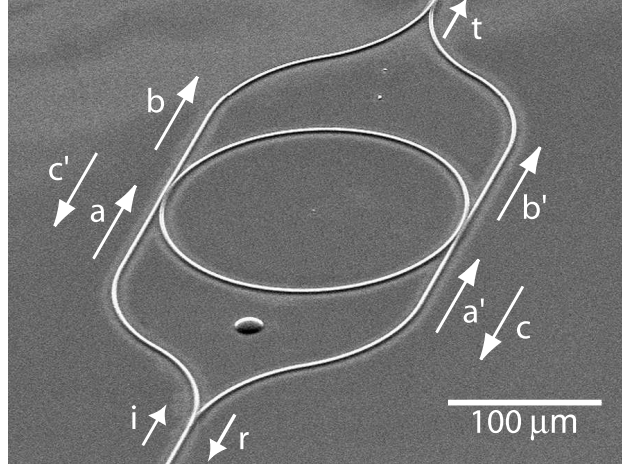


Figure 3.19: A scanning electron microscope perspective image of a device similar to that measured here. The input, reflected, and transmitted signals are labeled i, r and t , respectively. Two sets of fields, a, b, c and the corresponding primes, obey Equations 3.34 and 3.35.

3.6.1 Theory

Referring to the device shown in Figure 3.19, the central portion between the Y-junctions is the well-known microring resonator add/drop filter. Each of the two waveguides interacts with the ring according to the coupling matrix (see Section 3.2):

$$\mathbf{T} = \begin{pmatrix} t & \kappa \\ -\kappa^* & t^* \end{pmatrix} \quad (3.33)$$

where, for a unity input, t is the field amplitude transmitted past the coupler, and κ is the field amplitude coupled across the coupler. For a lossless coupler, $|t|^2 + |\kappa|^2 = 1$. In general, the two couplers need not be the same, but in the following we assume identical couplers.

Given an input, a , as shown in Figure 3.19, the normalized intensity past the resonator is given by (see Section 3.2):

$$\left| \frac{b}{a} \right|^2 = \frac{|t|^2 + |t|^2 \alpha^2 - 2|t|^2 \alpha \cos(\Theta)}{1 + |t|^4 \alpha^2 - 2|t|^2 \alpha \cos(\Theta)} \quad (3.34)$$

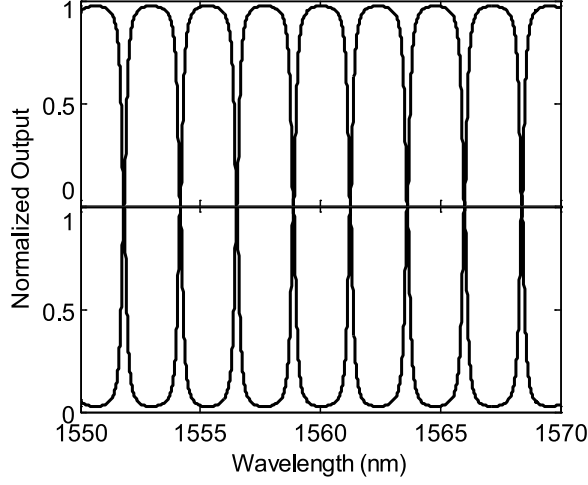


Figure 3.20: Normalized transmission (upper) and reflection (lower) signals for the microring-based inline reflector. For the calculation, the microring radius is 108.25 microns, the effective refractive index is 1.515, t is 0.85, and the loss parameter α is taken to be 1.

where α is the field amplitude remaining after one round-trip in the resonator, and $\Theta = \beta \cdot L$ is the phase accumulated over a ring circumference L for a waveguide with propagation constant β . The normalized intensity of the field exiting the drop port of the add/drop filter is given by (see Section 3.2):

$$\left| \frac{c}{a} \right|^2 = \frac{(1 - |t|^2)^2 \alpha^2}{1 + |t|^4 \alpha^2 - 2|t|^2 \alpha \cos(\Theta)} \quad (3.35)$$

When Θ is an integer multiple of 2π , and if the loss term α is close to one, then the input light exits through the drop port and no light is transmitted past the resonator.

As shown in Figure 3.19, a Y-junction splitter equally divides the input light between the upper and lower arms of the device. Thus, there are two identical sets of fields (a, b, c and a', b', c') obeying (3.34) and (3.35). Since the drop ports

are connected to the input, the dropped signals of (3.35) are the reflected signals. Figure 3.20 shows the predicted transmitted signal (upper plot) and the reflected signal (lower plot) for parameters as described in the figure caption.

3.6.2 Demonstration

For demonstration purposes, the microring-based inline reflector was fabricated in optical polymer. A silicon wafer with 5 microns thermal oxide ($n=1.445$) served as the device substrate and lower cladding layer. The core polymer, SU-8 ($n=1.565$), was crosslinked using direct electron beam exposure. The waveguide dimensions were 2 microns in width and 1.8 microns in thickness. Finite-difference mode solver calculations (see Appendix B) predict a well confined first-order mode ($n_{eff} = 1.515$) and weakly guided second- and third-order modes around 1550 nm. The microring resonator radius was 108 microns. The separation between the waveguides and the microring were designed to be 250 nm, resulting in approximately 25% power coupling. For measurement, the end-facets were prepared by cleaving the substrate wafer.

Transverse electric polarized light from a tunable laser was fiber-coupled to the device after passing through a circulator. Index matching fluid was applied, covering both the device and the fiber input to reduce the reflected signal noise to an acceptably low level. The reflected signal was collected by connecting the reflection port of the circulator to a photodetector. The transmitted signal was collected by focusing the output on a photodetector using a microscope objective. The wavelength was scanned from 1550 to 1570 nm and the normalized transmitted (upper plot) and reflected (lower plot) signals were recorded, as shown in Figure 3.21.

3.6.3 Discussion

Comparing the theoretical fit in Figure 3.20 to the measurement in Figure 3.21, we find good agreement. As expected, the nulls of the transmitted signal occur at the same wavelengths as the reflected peaks. The rejection ratio of the transmit-

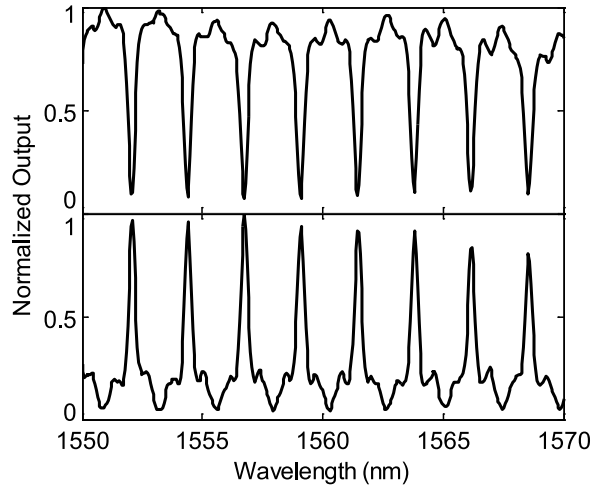


Figure 3.21: Measurement results showing the normalized transmission (upper) and reflection (lower) signals. The extinction ratios for the nulls in the transmission signal are better than 10 dB.

ted signal nulls is better than 10 dB. These nulls appear every free spectral range (FSR) of 2.33 nm. A closer inspection of the smaller features in the data shows a high degree of complementarity between the transmitted and reflected signals. These smaller features were caused by the weakly guided higher-order modes. This is supported by similar multimode behavior previously observed in slightly thicker SU-8 waveguides, and the lack of such features in slightly thinner waveguides. A best-fit of the data suggests a propagation loss of approximately 15 dB/cm. However, in the demonstration, there was no attempt to minimize the propagation loss. Since the bend radii are large, we attribute the propagation loss predominantly to scattering loss. This is reduced by stabilization of the lithography or by post-fabrication annealing of the polymer.

As an alternative to an integrated Bragg grating reflection filter, the microring-based reflector presents several advantages and increased flexibility. Most notably, the microring-based reflector is more compact than typical integrated waveguide

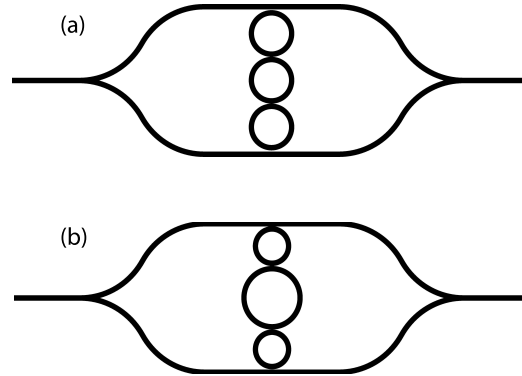


Figure 3.22: In (a): a reflector employing three microring resonators to exhibit a special spectral response (e.g., a wavelength-flattened reflection band). In (b): a reflector employing the Vernier effect with resonators of different radii.

gratings, allowing for simpler and more controlled fabrication, as well as for the possibility of incorporation with additional photonic devices.

The ability to simply manipulate the lineshape of the transmitted and reflected responses presents a significant advantage over both Bragg grating structures and the ring-based reflector suggested in Reference [69]. As previously pointed out, there exist several synthesis techniques for constructing higher-order filter responses using multiple microrings [40, 41]. Applying these algorithms to the reflectors presented here, one can design a system to deliver the desired lineshape transmission and reflection. One restriction is that there must always be an odd number of resonators for the device to act as a reflector. Shown schematically in Figure 3.22 (a) is such a device, employing three microrings to achieve a 3rd-order response.

Along similar lines, composite structures involving different resonators can be used, as illustrated in Figure 3.22 (b). When resonators of different circumference are placed in series, only wavelengths that are resonant with all resonators are transmitted in steady state. Thus, the reflected peaks and the transmitted nulls will only occur at wavelengths for which $m \cdot FSR_1 = n \cdot FSR_2 = \dots$ (the Vernier effect) for integers [73]. By employing this effect, integrated inline reflectors with

large free spectral ranges can be devised.

Finally, these reflective devices are easily rendered tunable by using the thermo-optic or electro-optic effects. These can be exploited to either tune the lineshape in multiple resonator structures, or to alter the resonant wavelength of an individual reflector. These tunable reflective elements can serve as laser end mirrors, providing wavelength selectivity as in Reference [74].

In conclusion, simple wavelength-selective inline reflectors based on microring resonator add/drop filters have been presented. The concept was demonstrated in optical polymer. The resulting device exhibited a rejection ratio better than 10 dB. The measured transmission and reflection signals were observed to have a high degree of complementarity, as expected from theoretical considerations. The versatility of these inline reflectors lies in the fact that multiple rings can be used for higher-order responses or to employ the Vernier effect. The compact structures can be fabricated using conventional techniques and thus, are readily incorporated with other photonic devices. Use of thermo-optic or electro-optic effects renders the reflected wavelengths or lineshapes tunable for use as laser end-mirrors.

Chapter 4

Coupled Resonator Optical Waveguides

4.1 Introduction

Serially coupled microresonators have been studied as optical filters exhibiting large free spectral range [75] and higher-order filter characteristics [40, 41, 76, 77]. In addition, it was recently shown that serially coupled microresonators present a fundamentally new form of waveguiding. Shown in Figure 4.1 are illustrations of three forms of waveguiding. Figure 4.1(a) represents the familiar and most common type of light confinement in which a refractive index difference between the core and the cladding traps the light within the core by total internal reflection. Examples of this type of waveguides are optical fibers and the planar waveguides described in Chapter 3. The second type of waveguiding uses Bragg reflections to reflect light impinging on the waveguide walls back toward the core layer. This is illustrated in Figure 4.1(b). Examples of these types of waveguides are photonic crystals and distributed feedback lasers. The newest class of waveguides has been termed coupled-resonator optical waveguides (CROWs) [78], and is shown in Figure 4.1(c). In this case, light circulates many times around the circumference of each resonator, each time weakly coupling to the adjacent resonators. The coupling acts to transmit power through the waveguide at a group velocity determined by the magnitude of the coupling, as will be shown. Although CROWs have also been proposed incorporating coupled photonic crystal defects, coupled

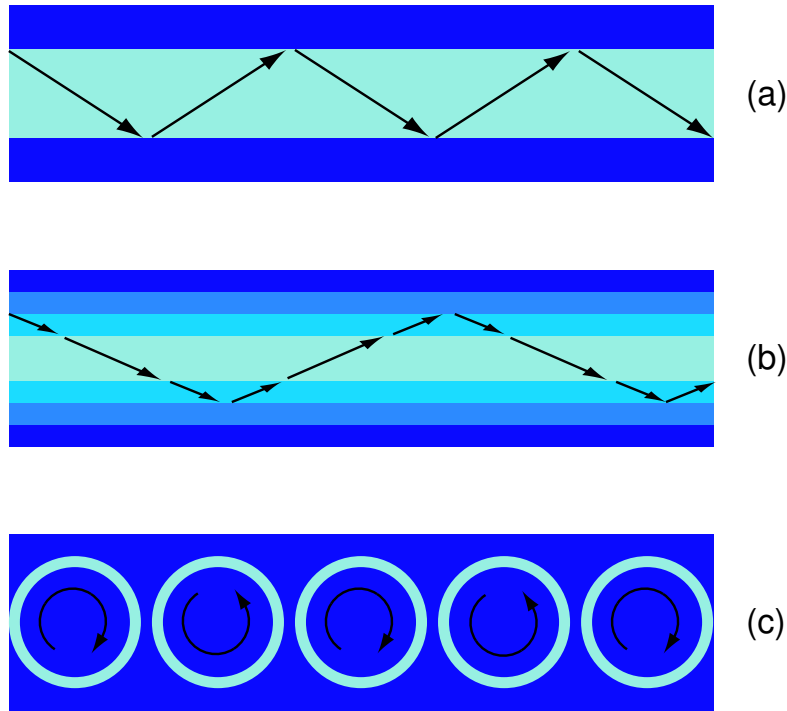


Figure 4.1: Three types of waveguiding structures. In (a), a conventional dielectric waveguide using total internal reflection for confinement. In (b), light is guided by Bragg reflection at the waveguide boundaries. In (c), light propagates by coupling from each resonator to the subsequent resonator.

Bragg resonators, or coupled whispering-gallery mode disks among others, we consider CROWs incorporating waveguide microrings as the resonators as depicted in Figure 4.1(c).

In this chapter, the development of CROW devices in polymer is presented. The fundamental theory of CROWs is first set forth as the basis for design and examination of the fabricated devices. Both the tight-binding method and a matrix method are introduced. A hybrid Mach-Zehnder CROW device is demonstrated in optical polymer, confirming both the validity of the analysis method and the ability to fabricate high-precision devices in polymers. Further, the advent of polymer CROW devices as optical delay lines is discussed.

4.2 Fundamental Theory of Coupled Resonator Optical Waveguides

4.2.1 Tight Binding Model

For the case of an infinite number of resonators, each weakly coupled only to nearest-neighboring resonators, a simple tight-binding formalism can accurately analyze the CROW [78]. In this limit, CROWs can exhibit reduced group velocity dependent only on nearest neighbor mode overlap integrals. The reduction in group velocity can improve the efficiency of nonlinear frequency conversion, or in the limit of zero group velocity, result in “frozen” pulses [79, 80].

The assumption of weak coupling between individual resonators implies that the individual resonator modes are perturbed only slightly by the adjacent resonators. This allows for the eigenmode of the individual resonator to be used as the basis for the CROW mode. This is essentially the same as the tight-binding (or linear combination of atomic orbitals, LCAO) analysis of electronic wave functions in a lattice of atoms. The analogy holds by making the individual resonators counterparts of the atoms and the CROW equivalent to the lattice. Similar to the initial assumption of the tight-binding analysis, the CROW eigenmode $\mathbf{E}_K(\mathbf{r}, t)$ is chosen to be a linear combination of individual resonator eigenmodes $\mathbf{E}_\Omega(\mathbf{r})$. Each resonator is located on the $\hat{\mathbf{z}}$ axis at $z = nR$ for resonator n . The resulting CROW eigenmode is

$$\mathbf{E}_K(\mathbf{r}, t) = E_0 e^{i\omega_K t} \sum_n e^{-inKR} \mathbf{E}_\Omega(\mathbf{r} - nR\hat{\mathbf{z}}) \quad (4.1)$$

It is also assumed that the individual resonator modes are nondegenerate, a requirement that is satisfied if only unidirectional propagation is assumed in each resonator. This is true in cases where there are negligible back reflections due to surface imperfections or very short coupling regions.

It is essential to calculate the dispersion relation to understand light propagation in CROWs. This is attained by inserting the ansatz CROW eigenmode (4.1) into the wave equation and finding the eigenvalue equation. The wave equation in

this case is

$$\nabla \times (\nabla \times \mathbf{E}_K) = \epsilon(\mathbf{r}) \frac{\omega_K^2}{c^2} \mathbf{E}_K \quad (4.2)$$

where $\epsilon(\mathbf{r})$ is the dielectric constant of the composite system of resonators and ω_K is the eigenfrequency of the mode. The same wave equation governs the individual resonator modes $\mathbf{E}_\Omega(\mathbf{r})$ if ω_K is replaced by Ω , the eigenfrequency of an individual resonator, and $\epsilon(\mathbf{r})$ by $\epsilon_0(\mathbf{r})$, the dielectric constant of an individual resonator.

To determine the dispersion relation, (4.1) is inserted into (4.2), and both sides are multiplied by $\mathbf{E}_\Omega(\mathbf{r})$. Integrating over all space, the dispersion relation is

$$\omega_K^2 = \Omega^2 \frac{1 + \sum_{n \neq 0} e^{-inKR} \beta_n}{1 + \Delta\alpha + \sum_{n \neq 0} e^{-inKR} \alpha_n} \quad (4.3)$$

where α_n , β_n , and $\Delta\alpha$ are overlap integrals defined by

$$\alpha_n = \int d^3\mathbf{r} \epsilon(\mathbf{r}) \mathbf{E}_\Omega(\mathbf{r}) \times \mathbf{E}_\Omega(\mathbf{r} - nR\hat{\mathbf{z}}) \quad n \neq 0 \quad (4.4)$$

$$\beta_n = \int d^3\mathbf{r} \epsilon_0(\mathbf{r} - nR\hat{\mathbf{z}}) \mathbf{E}_\Omega(\mathbf{r}) \times \mathbf{E}_\Omega(\mathbf{r} - nR\hat{\mathbf{z}}) \quad n \neq 0 \quad (4.5)$$

$$\Delta\alpha = \int d^3\mathbf{r} (\epsilon(\mathbf{r}) - \epsilon_0(\mathbf{r})) \mathbf{E}_\Omega(\mathbf{r}) \times \mathbf{E}_\Omega(\mathbf{r}) \quad (4.6)$$

The full dispersion relation of the CROW (4.3) can be simplified significantly by applying a few reasonable assumptions. First, it is assumed that the individual CROW modes are limited spatially to only couple to its nearest neighbors. Thus, one need only consider the coupling terms α_n and β_n for $n = 1$ and $n = -1$, as all others are set to zero. It is also assumed that the system is symmetric so that $\alpha_1 = \alpha_{-1}$ and $\beta_1 = \beta_{-1}$. The weak coupling means that the overlap integrals α_1 , β_1 , and $\Delta\alpha$ are small. The resulting simplified dispersion relation is

$$\omega_K = \Omega \left(1 - \frac{\Delta\alpha}{2} + \kappa_1 \cos(KR) \right) \quad (4.7)$$

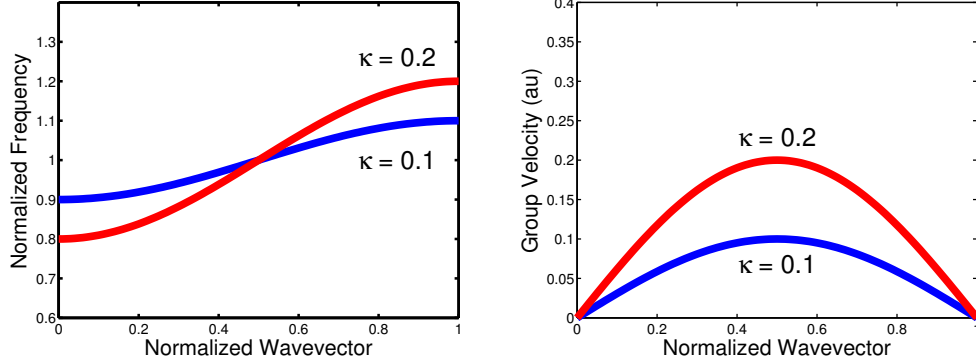


Figure 4.2: Left: Dispersion diagram showing plots of (4.7) with $\kappa = 0.1$ and 0.2 . The frequency ω_K is normalized to Ω . The wave vector is represented on the horizontal axis as KR/π . Right: Group velocity as a function of normalized wave vector for $\kappa = 0.1$ and 0.2 .

where κ_1 , the coupling coefficient, is defined as

$$\kappa_1 = \beta_1 - \alpha_1 = \int d^3\mathbf{r} [\epsilon_0(\mathbf{r} - R\hat{\mathbf{z}}) - \epsilon(\mathbf{r} - R\hat{\mathbf{z}})] \mathbf{E}_\Omega(\mathbf{r}) \times \mathbf{E}_\Omega(\mathbf{r} - nR\hat{\mathbf{z}}) \quad (4.8)$$

Shown on the left-hand portion of Figure 4.2 are plots of (4.7) for two values of κ_1 .

Taking the derivative of the dispersion relation with respect to the wave vector yields the group velocity

$$v_g(K) = \frac{d\omega_K}{dK} = -\Omega R \kappa_1 \sin(KR) \quad (4.9)$$

It is an important feature that the group velocity of the CROW is determined only by the coupling constant κ_1 . The right-hand portion of Figure 4.2 illustrates the dependence of the group velocity on the coupling coefficient. This feature can be manipulated to implement CROWs as optical delay lines, to be discussed in sections to follow.

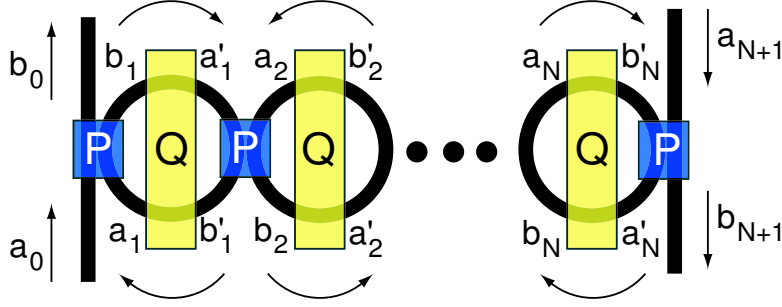


Figure 4.3: Coupled resonator optical waveguide with N rings (N odd for the output direction as shown). The arrows signify the direction of light propagation. The matrix \mathbf{P} represents the coupling segments and \mathbf{Q} accounts for the phase and loss accumulated in the resonators.

4.2.2 Matrix Method for CROW Analysis

For the present analysis, we employ an alternative analysis method in which each coupling section is represented by a coupling matrix and the phase and loss accumulated in the resonator are represented by a propagation matrix. By cascading the matrices, the transmission of the CROW is built up for an arbitrary series of resonators with arbitrary coupling between them. The model used here embodies a more general approach than the matrix method, restricted to neither the special case of weak coupling, nor an infinite number of resonators. The convergence of the matrix and tight-binding methods and an investigation on the limits of validity of the tight-binding method is presented elsewhere [81].

We describe the optical response of a CROW with a unidirectional (2×2) matrix model incorporating the evanescent ring-to-ring coupling and the propagation within each ring [40, 47]. The notation for the complex field amplitudes of the CROW device is shown in Figure 4.3.

The (assumed lossless) evanescent coupling of two waveguides is given by the

well-known coupling matrix of coupled-mode theory (see Section 2.3)

$$\begin{pmatrix} b'_n \\ b_{n+1} \end{pmatrix} = \begin{pmatrix} t & \kappa \\ -\kappa^* & t^* \end{pmatrix} \begin{pmatrix} a'_n \\ a_{n+1} \end{pmatrix}, \quad |\kappa|^2 + |t|^2 = 1 \quad (4.10)$$

where κ denotes the normalized coupling and t the transmitted field past the coupler. These are determined by the physical separation between the two coupled waveguides. (4.10) can be rewritten in the form

$$\begin{pmatrix} a_{n+1} \\ b_{n+1} \end{pmatrix} = \mathbf{P} \begin{pmatrix} a'_n \\ b'_n \end{pmatrix}, \quad \mathbf{P} = \frac{1}{\kappa} \begin{pmatrix} -t & 1 \\ -1 & t^* \end{pmatrix} \quad (4.11)$$

The optical phase and the waveguide loss accumulated over a half-ring distance is given by a propagation matrix

$$\begin{pmatrix} a'_n \\ b'_n \end{pmatrix} = \mathbf{Q} \begin{pmatrix} a_n \\ b_n \end{pmatrix}, \quad \mathbf{Q} = \begin{pmatrix} 0 & e^{-i\beta\pi R - \alpha\pi R} \\ e^{i\beta\pi R + \alpha\pi R} & 0 \end{pmatrix} \quad (4.12)$$

where α is the absorption coefficient per unit length, R is the ring radius, and $\beta = 2\pi n_{eff}/\lambda_0$ is the propagation constant of the waveguide. For the case of $N - 1$ resonators with N coupling regions, we form the full transmission matrix of the CROW by cascading the matrices \mathbf{P} and \mathbf{Q} :

$$\begin{pmatrix} a_{N+1} \\ b_{N+1} \end{pmatrix} = (\mathbf{PQ})_N (\mathbf{PQ})_{N-1} (\dots) (\mathbf{PQ})_2 P_1 \begin{pmatrix} a_0 \\ b_0 \end{pmatrix} = \mathbf{T} \begin{pmatrix} a_0 \\ b_0 \end{pmatrix} \quad (4.13)$$

For simplicity we adopt the notation

$$\mathbf{T} = \begin{pmatrix} A & B \\ C & D \end{pmatrix} \quad (4.14)$$

Assuming an input a_0 , and taking $a_{N+1} = 0$, the output complex field amplitudes

normalized to the input are

$$\frac{b_0}{a_0} = -\frac{A}{B}, \quad \frac{b_{N+1}}{a_0} = C - \frac{AD}{B} \quad (4.15)$$

Starting with (4.13) and applying the Bloch theorem, the dispersion relation is [81]

$$\sin(\beta\pi R) = \pm \text{Im}(\kappa) \cos(K\Lambda) \quad (4.16)$$

where K is the Bloch wave vector and Λ is the periodicity. The \pm results from considering forward and backward propagating waves. Expanding the left hand side of (4.16) and assuming small argument (corresponding to weak coupling) and forward wave propagation, the resulting dispersion relation is [81]

$$\omega = \Omega \left[1 + \frac{|\kappa|}{m\pi} \cos(K\Lambda) \right] \quad (4.17)$$

where m is the azimuthal mode number. This result calculated in the matrix formalism is in essence identical to (4.7), which was calculated from the tight binding method when we make the association between κ_1 and $\kappa/m\pi$.

4.3 CROW Mach-Zehnder Interferometer

The Mach-Zehnder interferometer (MZI) presents one of the simplest geometries for interrogating optical phase characteristics of waveguides through interference. A MZI composed completely of coupled photonic crystal defects was proposed and fabricated with aluminum rods, and interference nulls were observed in the microwave regime [82]. However, by incorporating a CROW as only one path of the MZI, interference occurs between the field amplitudes of a waveguide whose phase properties we know (conventional ridge waveguide) and a waveguide whose phase properties we are interested in (CROW). A similar concept was used to investigate light propagation for coupled defects in an aluminum rod photonic crystal by measuring the interference of microwaves in free-space and in the coupled-defect device [83]. A schematic diagram of the CROW-MZI device we propose is illus-

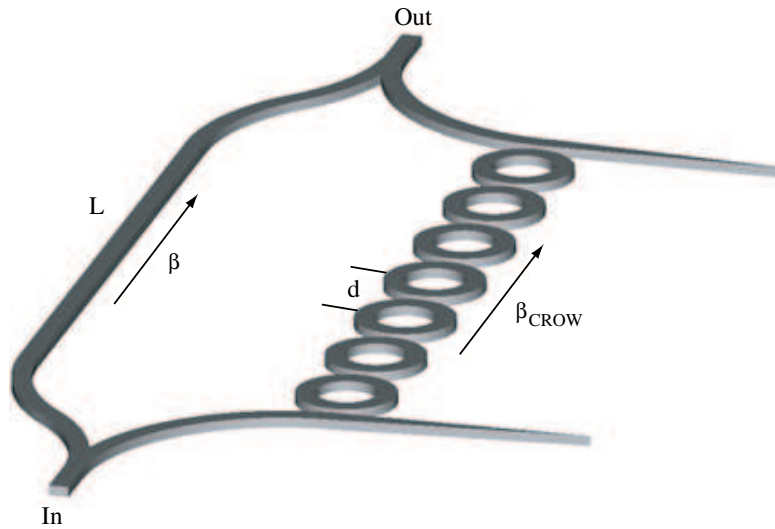


Figure 4.4: Schematic diagram of a CROW-MZI with one arm as a ridge waveguide of length L , with propagation constant β , and the other arm consisting of coupled microresonators, spaced by a distance d , with propagation constant β_{CROW} . Y-branches divide and add the optical field equally between the two arms. Adiabatic tapers act as impedance matched terminations after the field couples to the first resonator, ensuring no back reflected fields.

trated in Figure 4.4. In this section, we demonstrate a CROW-MZI fabricated in a polymeric waveguide material for operation near telecommunications wavelengths ($\lambda \sim 1550$ nm). Good agreement is found between the measured results and the predictions of the matrix theory.

4.3.1 Fabrication and Measurement

The devices were prepared by first spinning a $1.6 \mu\text{m}$ thick optical core layer of SU-8 ($n=1.565$) onto a silicon wafer with $5 \mu\text{m}$ of thermal silicon-oxide serving as the lower cladding. Waveguides of width $2 \mu\text{m}$ were directly patterned by electron beam crosslinking of the SU-8 core using a scanning electron microscope (SEM). The end facets of the waveguides were left as prepared by cleaving the

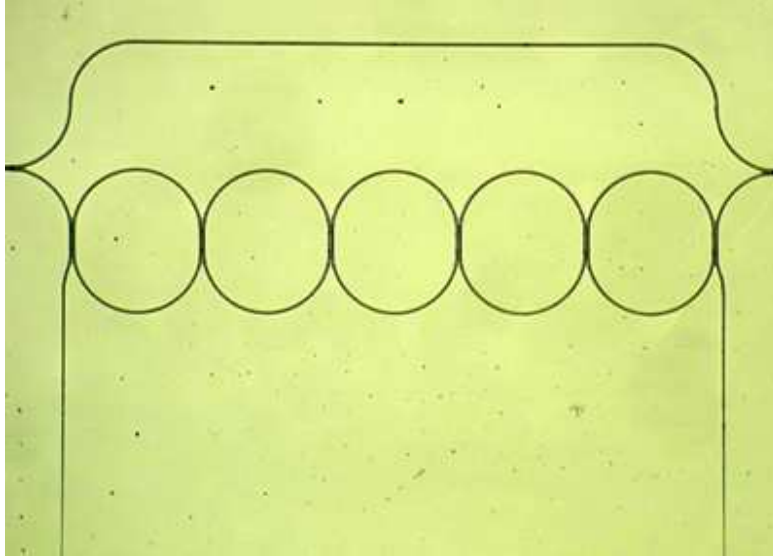


Figure 4.5: Optical microscope image of the CROW-MZI showing a total device width of approximately 1.2 mm. The identical racetrack microresonators had 50 micron straight coupling sections and 100 micron bend radii in the curved sections.

substrate. The racetrack resonators had semi-circular sections of radius $100 \mu\text{m}$, and $50 \mu\text{m}$ long parallel coupling regions. The waveguides in the coupling section were separated by 750 nm , although further SEM investigation revealed a layer of residual SU-8 between the waveguides, decreasing the effective separation and increasing the coupling beyond what would be expected for a 750 nm gap. The effective refractive index of the waveguide was calculated to be 1.485 by semi-vectorial finite difference simulation (see Appendix B). The free spectral range of an individual resonator is therefore 2.2 nm for transverse electric (TE) polarized light in the vicinity of the 1550 nm telecommunication band. An optical microscope image of the fabricated device is shown in Figure 4.5.

For measurement, a tunable laser diode provided the input TE-polarized optical signal via a polarization controller and a tapered single-mode fiber. The device output was collected by a $20\times$ microscope objective focused on either an infrared CCD for viewing or a photodetector for measurement. Both the tunable laser and

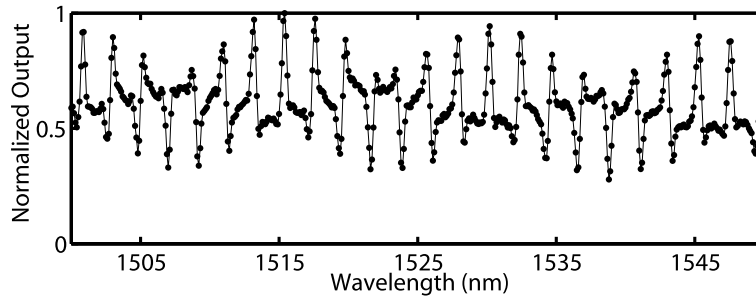


Figure 4.6: Normalized measured output power of the polymer CROW-MZI ranging over a spectral bandwidth of 50 nanometers, approximately 22 single resonator free spectral ranges.

the photodetector measurement were controlled by computer. Shown in Figure 4.6 is a measured spectrum of the CROW-MZI transmission for an input wavelength scan of 50 nanometers, ranging from 1500 to 1550 nanometers, covering approximately 22 individual-resonator free spectral ranges. The output spectrum shows an intricate, but essentially periodic, interferometric waveform.

4.3.2 Results and Discussion

In resonant optical systems, small parameter deviations due to slight fabrication errors typically result in unintended spectral features. For instance, small deviations (fractions of a wavelength) in the radii of the $N - 1$ constituent resonators result in different resonance frequencies that potentially spoil sharp spectral transmission features of a CROW device. Furthermore, the transmission is very sensitive to small differences (tens of nm) in the N gaps between the coupled waveguides that comprise the CROW. Thus, for a proper analysis of the device fabricated and measured here, we would expect the need for $N - 1$ fitting parameters for the ring radii and N for the coupling sections. In addition, other variables to be included in the fit are: the length of the ridge waveguide arm, the waveguide loss per unit length, the polarization mixing ratio, the waveguide effective refractive index for both polarizations, and the overall wavelength shift.

To greatly simplify the analysis, we undertake the assumption of single values for the resonator radii and coupling coefficients. Considering this special case of (4.13) with identical matrices \mathbf{P} and \mathbf{Q} , the transmission matrix becomes

$$\begin{pmatrix} a_{N+1} \\ b_{N+1} \end{pmatrix} = (\mathbf{PQ})^N \mathbf{P} \begin{pmatrix} a_0 \\ b_0 \end{pmatrix} \quad (4.18)$$

In the CROW-MZI shown in Figure 4.5, a dividing Y-branch evenly distributes the optical field between the ridge waveguide and CROW sections of the interferometer, while an adding Y-branch combines the fields that have traveled the separate paths. Thus, light is input only at one port of the CROW section and the output field amplitudes for this arm are given by (4.15), with \mathbf{T} defined by (4.18). At the combining Y-branch, the field in the ridge waveguide arm has accumulated an optical phase and loss given by $e^{-(\alpha+i\beta)L}$ in a length L . The output transmitted power is proportional to the square of the summed complex amplitudes of the fields passing through the two arms

$$output \propto \left| C - \frac{AD}{B} + e^{-(\alpha+i\beta)L} \right|^2 \quad (4.19)$$

Finally, this simple analysis method does not incorporate waveguide dispersion – typically a linear function of wavelength – nor does it account for the wavelength dependence of the coupling coefficient which can vary significantly over the large bandwidth measured here.

In Figure 4.7, we show the theoretical fit (blue) of the CROW-MZI transmission superimposed on the experimental data (black). A wavelength range of approximately 30 nm is shown to more clearly show the detail of the fit to the data. The parameters used for the fit are noted in the caption of Figure 4.7 and are consistent with expected values. Using these parameters, the intrinsic CROW response is given by (4.15). The qualitative agreement in Figure 4.7 between the theory and experiment is remarkable, considering the many simplifying assumptions described above. Clearly the precision of the fabrication was sufficient to

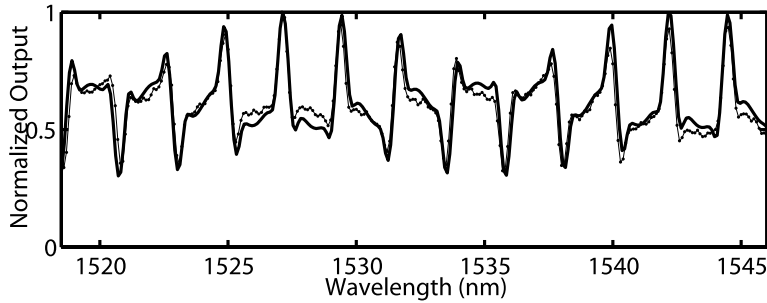


Figure 4.7: Experimental data (thin line with filled circles) and the theoretical fit (solid thick line) based on (4.18). The fitting parameters used for the fit were: polarization 93% TE and 7% TM, effective indices 1.48475 for TE and 1.48555 for TM, power coupling coefficients 0.46 for TE and 0.85 for TM, and waveguide loss of 30 dB/cm.

validate our assumptions and confirm the theory.

We have demonstrated at telecommunications wavelengths a novel polymeric MZI geometry that uses serially coupled microresonators. In a conventional MZI, light that traverses two separate optical paths interferes after accumulating different optical phases. The optical paths typically differ only in the effective optical length so that only a phase difference, but no intrinsic amplitude response, is incurred in each arm. Here, however, one path is a ridge waveguide, while the other arm consists of coupled resonators. The response of the coupled resonator arm exhibits not only more complicated phase properties than a simple ridge waveguide, but also a periodic spectral response of the absolute field amplitude. Thus, the overall transmission is a mixture of the interference of different phases accumulated in the two arms of the device, and the spectral amplitude response of the CROW arm. Although these phenomena cannot be simply decoupled in a CROW with a finite number of resonators, the simple matrix model used to analyze the CROW-MZI shows good agreement with the measured spectral output. Using the assumption of exactly equal ring radii and coupling coefficients, the agreement of the experimental data and the theoretical fit attests to the precision of the

fabrication.

4.4 Potential Applications of Polymer CROWs

There are several applications envisioned for CROWs in integrated optics. For instance, more efficient frequency conversion in a nonlinear medium can be attained because the propagation of light in a CROW is slower than propagation in standard ridge waveguides, and because high power levels are built up as light circulating within each resonator. Specifically, by fabricating a CROW in material capable of second harmonic generation (SHG), the high fields and slow propagation result in increased second harmonic efficiency [79]. Further, the dispersion diagram can be manipulated through careful design to ensure proper phase matching of the fundamental and second harmonic signals. Manipulation of the dispersion diagrams can also be used to offset unwanted dispersion of optical pulses in wavelength division multiplexed systems. As a single resonator acts as an optical filter, a CROW acts as a high-order optical filter capable of passing the desired wavelengths with high extinction ratio [40, 41, 76, 77]. Similarly, a CROW with dissimilar resonators can be used for an optical filter with free spectral range large enough such that there is only one pass or rejected signal within a wide communications spectrum [75].

Among the most compelling applications of CROWs are for use as optical delay lines or pulse storage devices. Delay lines are important in optical time division multiplexed systems where data signals must be made to coincide with tag or control signals. Delay lines are also important for radio-frequency phased-arrays to provide tunable signal time delay for beam steering.

Optical delays can be achieved by either changing the physical distance light travels, or by enhancing the travel distance of the light by the use of optical resonators. Resonators achieve this length enhancement by increasing the effective length of flight for a light beam through the many reflections within the cavity before the light is transmitted. It has been shown that a CROW acts as an equivalent waveguide with effective length indicative of the delay, given by the

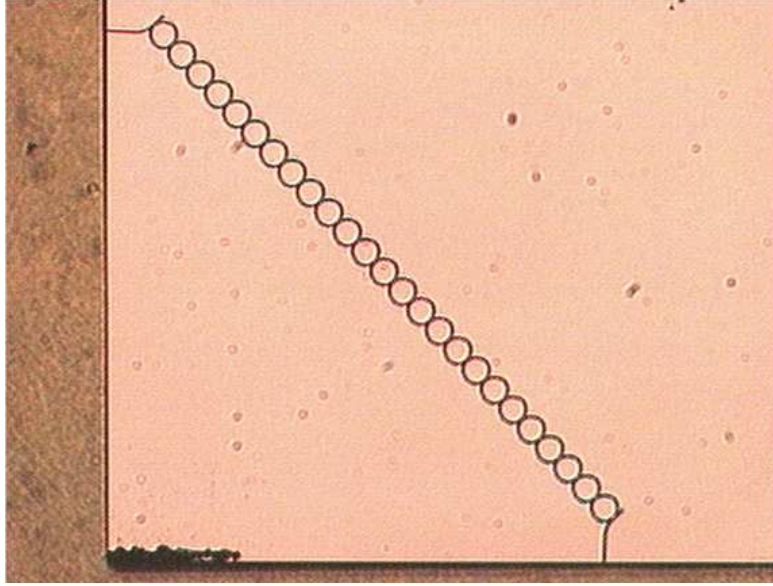


Figure 4.8: An example of a CROW delay line consisting of 27 microring resonators, each with radius $50 \mu\text{m}$ and separated by 200 nm , fabricated in SU-8 by direct electron-beam exposure.

simple form [84]

$$L_{eff} = \frac{\pi RN}{|\kappa|} \quad (4.20)$$

where $|\kappa|$ is the coupling coefficient, R is the ring radius, and N is the number of rings. Clearly, either more resonators or a smaller coupling results in a longer effective length and longer delay. This is intuitively simple; with smaller coupling, it takes longer for the light to couple from one resonator to the next down the waveguide so the group velocity is decreased and delay increased.

From (4.20), we see that the goal in designing optical delay lines in CROWs is to decrease the coupling and to increase the number of resonators. However, there is a penalty for decreasing the coupling. Since resonant structures are incorporated in the device, smaller coupling results in narrower pass-bands. This means that the usable bandwidth of the delay line is decreased as the delay is increased through smaller coupling. See Reference [84] for a more thorough discussion of the tradeoffs in the design of CROW delay lines.

An example of a polymer CROW delay line is shown in Figure 4.8. Fabricated in SU-8 directly on a silicon wafer with 6 μm silica serving as the lower cladding, the CROW incorporates 27 microresonators. Each microresonator is 50 μm in radius, separated by 200 nm, and has waveguide dimensions of 1.6 by 2.0 μm . This device has not been characterized at the time of writing this thesis. Polymer materials present a good platform for CROW delay lines due to the ease and flexibility of fabrication, the ability to produce reasonably high-Q resonators, and the ability to integrate the CROWs with other on-chip devices. Further, the functionality of the material can be enhanced by blending in the polymer a multitude of dopant molecules such as electro-optic molecules or lasing dyes capable of providing gain, to render CROW delay lines tunable.

Chapter 5

Soft-Stamp Replica Molded Polymer Integrated Optical Devices

5.1 Introduction

As has been demonstrated in the preceding chapters, many devices used for integrated optics inherently require high resolution in their patterning. High resolution fabrication is achievable through the use of electron beam lithography. The major limitation of electron beam lithography, however, is the limited throughput of the procedure when compared to other lithography techniques, most notably, ultraviolet photolithography. The main factor in making electron beam lithography an inefficient method is that it must occur within a vacuum, and thus, several minutes are spent for each sample for the chamber to pump down to appropriate pressures. This time-consuming procedure oftentimes negates the use of electron beam lithography in industrial settings as a tool for mass fabrication of optical devices. Thus, there is a quandary: on the one hand, there is a need for high-resolution fabrication, but on the other there is also a demand for high-throughput fabrication. The procedure in this chapter evokes promise for solving the resolution/throughput predicament.

In this chapter, the method of soft-stamp replica molding of polymer optical integrated circuits is discussed and demonstrated. First, the basic method is described. A difficulty that is characteristic of the method is presented and the

overcoming of this issue is detailed. Next, the efficacy of this method for replicating precise optical elements is demonstrated through fabrication and characterization of a microring resonator. Finally, a more advanced application of replica molding is demonstrated: the ability to mold several devices successively on separate layers, thus producing a three-dimensional polymer integrated optical chip.

5.2 Soft-Stamp Replica Molding

5.2.1 The Technique

Soft lithography has proven to be a powerful technique for fabricating many novel structures [85, 86, 87]. Optical devices made by soft lithography have been mostly limited to the visible regime. The process is, however, largely unexplored for producing complex polymer optical elements useful for infrared telecommunications applications. Implemented by Zhao et al. to make polymer optical couplers [88] in the visible regime, the technique has been extended to make polymer distributed feedback and distributed Bragg reflector lasers [89], hybrid organic/inorganic photonic crystal lasers [90], and mesoporous silica waveguide lasers [91]. It has been recently shown that soft lithography is amenable to producing integrated optical components in the infrared regime such as optical interconnects [92]. The early fundamental research particularly demonstrates the high fidelity and precision required to achieve the performance needed for fabrication of devices in the telecommunications component industry.

In contrast, hard-mold replication – or hot embossing – of polymer devices has been used to make several devices (e.g., microring resonators [93]), but this technique presents several difficulties. For complex multi-layer devices, this procedure is less useful due to the high temperatures needed to reflow the polymer film. The high temperatures needed for reflow could disturb lower cladding layers and may possibly alter optically active dopant molecules. Furthermore, this process is also of limited use for cross-linking polymer films because for these materials, the degradation and glassy temperatures occur at nearly the same temperature.

Finally, hard molding is less useful for mass production due to pattern defects caused by the physical contact between the mold and the substrate, thus limiting multiple use of the hard mold. In contrast, for soft-stamp replica molding, polydimethylsiloxane (PDMS) is used to make the mechanically flexible molds because its relatively low surface energy results in weak adhesion to other materials. This property allows a large number of PDMS molds to be produced from one master device. It also allows for the easy release of the molded polymeric replicas from the PDMS mold without damage. Using soft lithography, several simple optoelectronic components have been fabricated such as distributed feedback structures [89, 94, 95, 96], photonic band-gap structures [90], microlens arrays [97], and waveguides [67, 88].

The process-flow diagram is shown in Figure 5.1. The master device is first prepared by photo-lithographic or electron beam patterning of SU-8 resist on a bare silicon substrate (Figure 5.1(a)). The master is baked for one hour at 150 °C to harden the structures and to smooth out nanometer scale sidewall and surface imperfections due to the exposure and developing. To make the mold, liquid poly (dimethylsiloxane) (PDMS) is poured atop the master device in a Petri dish (Figure 5.1(b)). The PDMS is cured for one hour at 80 °C, upon which the mold is peeled from the master device (Figure 5.1(c)).

To make the replica device, a drop of solution is placed on an appropriate substrate (Figure 5.1(e)) and the mold is depressed (Figure 5.1(f)). To guide light, the substrate must have a layer of material with a lower refractive index than the core light-guiding material. Typically, a layer of SiO₂ ($n=1.45$) or another polymer ($n \simeq 1.3-1.6$) is used. Droplets of the core polymer solution are placed on the substrate, and as the mold is depressed, the force exerted on the mold is monitored with a force gauge (see Figure 5.2). For evaporative-cured polymers, the solvent escapes through the PDMS mold, thus solidifying the waveguide structures. The mold is released and removed from the substrate, revealing the waveguide structures (Figure 5.1(g)). The molded replica device is baked at 100 °C for two hours to remove any remaining solvent. A photograph of the basic molding setup

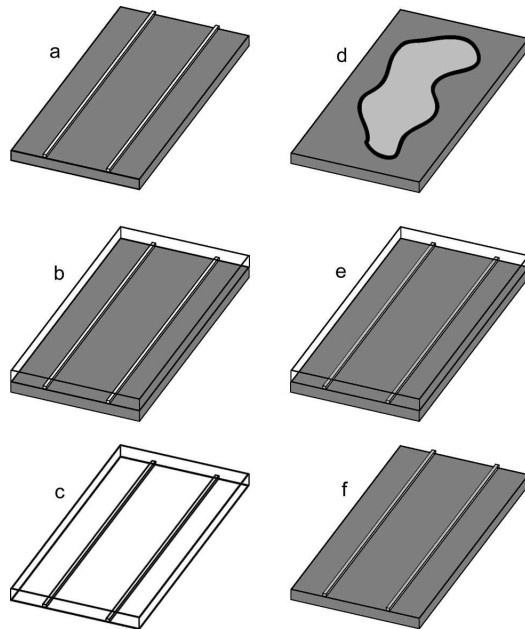


Figure 5.1: Schematic diagram of the replica molding process for polymer waveguide devices. (a) The master device is fabricated in SU-8 resist by ultraviolet or electron beam exposure. (b) PDMS is poured atop the master device and thermally cured. (c) Once cured, the PDMS mold is peeled from the master device. (d) A drop of the core polymer solution is placed on an appropriate substrate. (e) The PDMS mold is depressed. (f) Once cured, the PDMS mold is peeled to expose the molded replica.

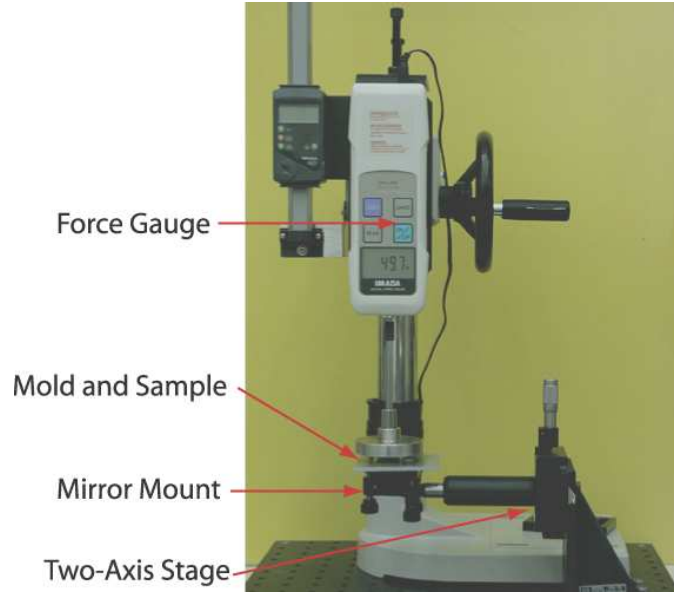


Figure 5.2: Photograph of the molding setup.

is shown in Figure 5.2. The necessary components other than the mold and sample substrate are a two-axis stage, a mirror mount, and a force gauge.

An example application of polymer waveguide molding is shown in Figure 5.3. Given a semiconductor chip with CMOS drive or trimming circuitry, active polymer waveguides and devices can be molded directly on the circuitry. The resulting hybrid device represents multi-material and multi-functional integration of optical and electrical devices. Clearly, such integration is not so simply achieved using crystalline materials.

5.2.2 The Background Residue

A limiting difficulty of this technique remains. The ubiquitous presence of a background residue of polymer material has the potential to ruin the desired optical performance of devices. We study numerically the impact of the presence of the residue on simple optical waveguides, on the coupling output ratio of directional couplers, and on the radiation losses in waveguide bends. We investigate techniques of reducing the residue to acceptable levels. Control of the residue to acceptable

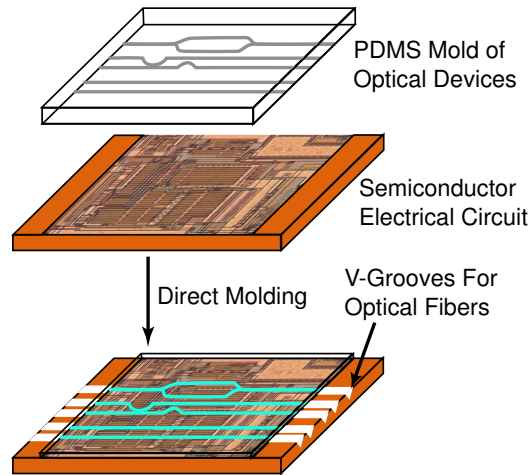


Figure 5.3: Molding of polymer waveguide structures directly on electrical circuitry.

levels leads the way to the mass production and deployment of polymer integrated optical devices fabricated by soft-mold replication.

Here, for the investigation of the effects of molding parameters on the structural features, we use bare silicon as the substrate. The core polymer solution is prepared by dissolving a polycarbonate, Poly[Bisphenol A carbonate-co-4,4'-(3,3,5-trimethylcyclohexylidene)diphenol carbonate] (Aldrich) in dibromomethane, CH_2Br_2 in varying concentrations from 7.2 to 0.45 wt.%. The polycarbonate is of practical interest as it is the same polymer host material used in the state-of-the-art electro-optic guest-host systems [10].

As seen in Figure 5.4, the replica molding process of polycarbonate ridge waveguides results in an undesired background residue film. It is crucial to know to what extent this residue impairs the performance of integrated optical devices. Several test cases can be investigated using simulation tools. Here, we study the effects of the background residue on three fundamental properties important for integrated optical waveguide devices: the modal properties of individual waveguides, the output coupling ratio in directional couplers, and the radiation loss due to the curvature of waveguide bends.

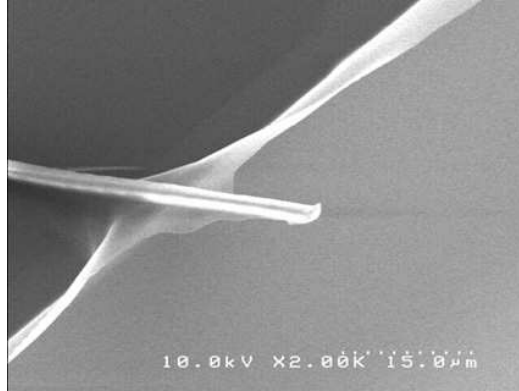


Figure 5.4: Scanning electron microscope image of a molded waveguide, and the surrounding residue, overhanging a cleaved silicon substrate.

Numerical Simulations

Of basic interest for any guided wave device are the modal properties of an individual waveguide, described chiefly by the mode effective indices n_{eff} . Since the mode effective indices are governed in part by the cross-sectional shape of the waveguide, it is expected that the presence of the residue will alter the modal properties of the waveguide. For effective indices below the bulk refractive index of the cladding material, the mode is cut-off and will not be guided. Further, modes that are near cut-off are more weakly guided and typically exhibit more propagation loss. The effective indices of the several lowest-order modes are calculated using a semi-vectorial finite-difference method mode-solving algorithm (see Appendix B) for residue thicknesses varying from zero to $1 \mu\text{m}$. The waveguide is taken to have a $2.5 \mu\text{m}$ square cross-section, independent of the residue, with core index 1.6. The cladding index of 1.55 is chosen to ensure single-mode operation for transverse-electric polarized light at 1550 nm, with no residue present. Figure 5.5 shows the results of the calculations. The first-order mode is guided for all values of the residue thickness, and the effective index increases as the residue increases in thickness. The second- and third-order mode effective indices become larger than the cladding index when the residue thickness is approximately 200

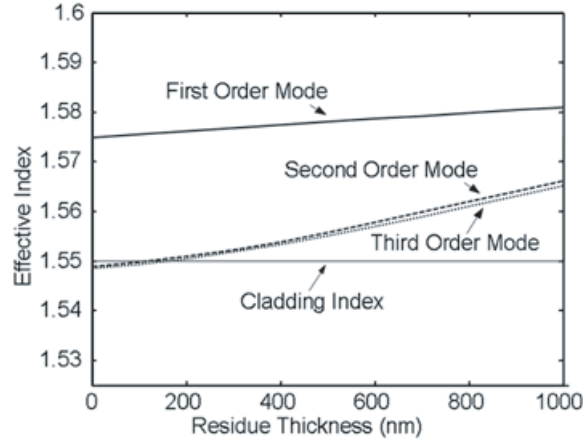


Figure 5.5: Effective indices of the first, second and third order mode as a function of residue thickness.

nm. However, at this residue thickness, these modes are presumed to be weakly guided and exhibit high propagation loss. For thicker residues, the effective indices of these higher-order modes become significantly greater than the cladding index and are thus more strongly guided. These modes would degrade device performance through mode-mixing. From these results, we find that for preventing multimode behavior, restricting the residue thickness is important. If the residue cannot be restricted, it is important to know the thickness so the other waveguide dimensions can be reduced appropriately to ensure single mode guiding. For the parameters used in this example, limiting the residue thickness to several hundred nanometers is essential, but for different waveguide cross-sections, this value could be more or less, depending on how close the higher-order modes are to cut-off.

Directional couplers are passive devices that divide input light between two output waveguides due to the proximity of the waveguides. As such, directional couplers form fundamental elements in Mach-Zehnder modulators, optical switches, and lattice filters [36]. The proportion of light coupled from one waveguide to an-

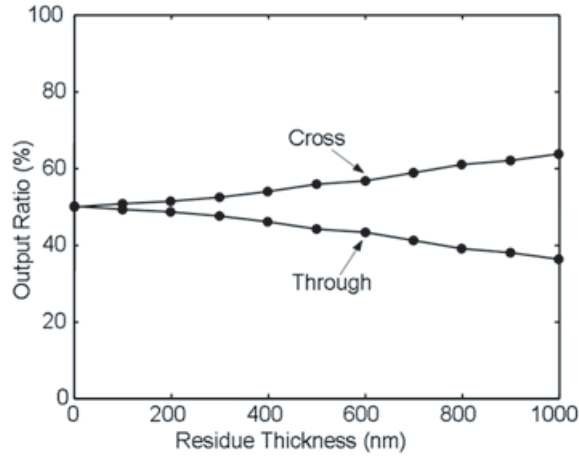


Figure 5.6: Output ratio of a directional coupler as a function of residue thickness.

other is determined by the field amplitude overlap integral. Because this overlap integral is determined by the individual waveguide field profiles, the results of the previous section suggest that the output coupling ratio should be strongly affected by the presence of a residue. To study the effects of the residue on the performance of optical couplers, a finite-Fourier-transform beam propagation method algorithm (see Appendix A) is used to calculate the coupling output ratio for varying residue thickness. Two waveguides, each of the same cross-section and refractive indices as in the previous section, are separated by $1.4 \mu\text{m}$ for a coupling length of $147 \mu\text{m}$. The separation and coupling length are chosen as such so light input into one waveguide results in an output coupling ratio of 50% (3-dB coupling) with no residue. The results of the calculation, shown in Figure 5.6, indicate that indeed, the output coupling ratio increases with increasing residue thickness. For small residue thicknesses, the deviation from the desired 3-dB coupling is small, but for residue thicknesses greater than a few hundred nanometers, the deviation becomes significant. This is due to the fact that as the residue gets thicker, more of the individual mode field amplitude occupies the area shared by both individual modes

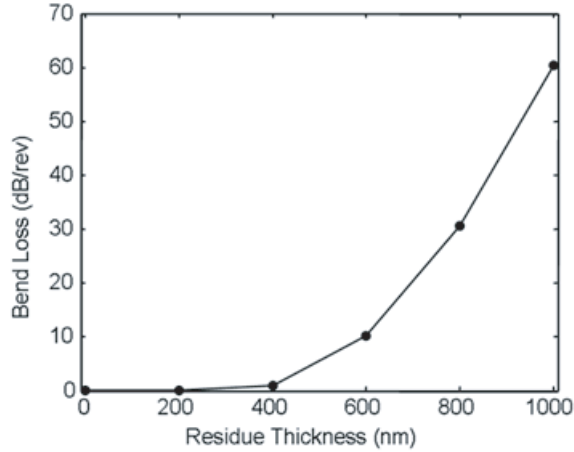


Figure 5.7: Bend loss as a function of residue thickness.

so the overlap integral is increased.

Waveguide bends are integral in nearly all integrated optical circuits. More specifically, a waveguide that bends back upon itself forms a ring resonator that exhibits resonances periodic in wavelength, each occurring when light acquires a phase equal to an integer multiple of 2π radians. Such structures are used for channel-dropping filters [41], intensity modulators [42], and dispersion compensators [36]. For a given bend radius, bend loss is predominantly determined by the degree of confinement. As the residue thickness increases, more of the field occupies the residue, which is not laterally restricted by refractive index, so it is expected that the bend loss significantly increases as a function of the residue thickness. To test this supposition, an azimuthal beam propagation algorithm [98] is used to calculate the bend loss by monitoring the remaining field amplitude in the waveguide after each revolution of the optical field. As in the previous two calculations, we take the waveguide cross-section to be $2.5 \mu\text{m}$ square with core and cladding index 1.6 and 1.55. The bend radius is $400 \mu\text{m}$, chosen because it gives essentially no bend loss for the ring without residue. The results of the

calculation, Figure 5.7, show that bend loss is a dramatic function of the residue thickness. For residues up to 400 nm, the bend loss is less than one dB/revolution, however, the bend loss quickly increases to unacceptable levels for residues thicker than 400 nm.

Reduction of the Residue

The reduction of the residue is of paramount importance for replica molding to be a useful technique for polymer waveguide fabrication. The previous simulations have shown that while small residue thicknesses are tolerable in many cases, as the residue becomes thicker, the waveguides may exhibit multimode behavior, directional couplers will not divide light as intended, and waveguide bends will exhibit unacceptably high loss. In defining what variables are at hand for reducing the residue, there exist several plausible possibilities. Two apparent means of reducing the residue thickness are changing the concentration of the polymer solution or the force with which the mold is depressed. Although chemical or plasma etching is a possible treatment for reducing the residue, this adds a costly step to the otherwise simple fabrication procedure and introduces spurious effects such as changing the surface features such as smoothness and reducing the waveguide thickness. Another possibility that must be immediately disregarded is the change in the shape or size of the structures. The waveguide structures cannot be modified because the dimensions are determined by the modal waveguide requirements (e.g., as required for the optical device). However, previous results suggest that typical polymer optical waveguide dimensions are in the correct size and shape regimes to avoid mold deformations: the waveguides are thin enough so that there is no sagging of the mold, but wide enough and separated enough to avoid lateral deformations of the mold [99].

The solution concentration is an obvious candidate for reducing the residue, as the residue thickness will be dependent on the solution viscosity and density. Previously, dilution of a resist solution was used to reduce the residue in soft molding of etch resist, allowing a single-step etch to pattern a silica substrate [100]. To deter-

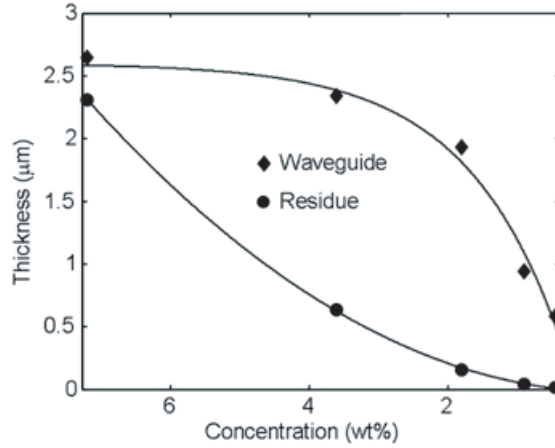


Figure 5.8: Waveguide and residue thickness for various solution concentrations.

mine the functional dependence of the solution concentration, we mold amorphous polycarbonate waveguide structures using several concentrations of the polycarbonate solution. A stock solution of 7.2 wt.% polycarbonate in dibromomethane is diluted in factors of two resulting in concentrations of 7.2, 3.6, 1.8, 0.9, and 0.45 wt.%. Each solution is used to mold the waveguide structures with a constant force of 50 N applied to the mold in each case. Upon solvent evaporation and removal of the mold, it is visually clear that the background films are greatly reduced by reducing the solution concentrations. A stylus profiler is used to precisely measure the thickness of both the background residue and the waveguide thickness for each of the test samples. The thicknesses at several locations – the same for each sample – were measured and averaged. The measurement results are shown in Figure 5.8. The residue thickness is strongly reduced by decreasing the concentration of the solution, suggesting that carefully selecting the appropriate solution concentration is a good means of reducing or controlling the residue thickness. The cost of reducing the residue by thinning the solution, however, is the reduction in the thickness of the waveguides for very low concentrations. This is because for low

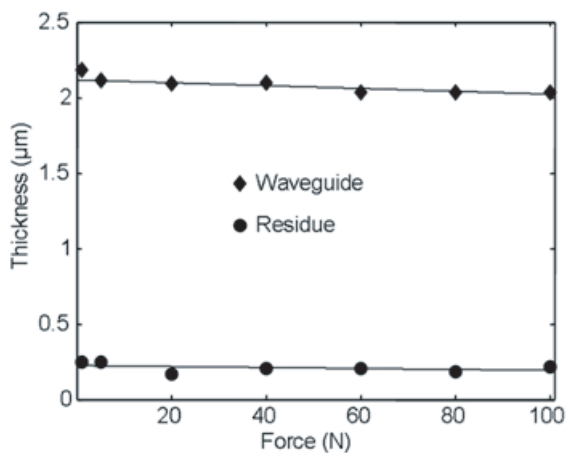


Figure 5.9: Waveguide and residue thickness for various forces applied to the mold.

concentrations, there is not enough solid in the volume of solution that fills the waveguide mold and so the condensed solid volume is much less than the intended thickness.

The mechanism that results in the residue appears to be trapping the solution between the mold and the substrate, forming pockets within which the solid residue forms. It is reasonable to assume that the force with which the mold is depressed may be a useful parameter for the reduction of the background residue because higher force would drive out more of the trapped solution. We mold several waveguide structures using a similar procedure as above, but at a constant concentration (1.8 wt.%) for various forces applied to the mold (2-100 N). The corresponding range of pressures on the mold is 3×10^4 (0.3) to 1.46×10^5 Pa (14.6 N/cm²). When the samples are cured, the mold is removed and the film and waveguide thicknesses are measured with a stylus profiler. The results are shown in Figure 5.9. The thickness of both the residue and the waveguide are changed very little over a wide range of applied forces, demonstrating that the force applied to the mold is not a useful means for reducing the residue. Since the residue is very

weakly affected by the force on the mold, we must consider two other observed effects that could potentially degrade device performance. First, for low forces, the mold did not make conformal contact [101] with the substrate and a very thick residue was often observed at an edge or corner of the molded area. Second, for very high forces, the mold began to deform around the edges, distorting the device features at the extremities of the mold.

As proposed, the mechanism for the formation of the residue is due to the soft and flexible nature of the PDMS mold. As the mold is depressed, the solution on the substrate is forced into the waveguide structures and the excess escapes to the edges of the mold. What solution does not escape, however, forms pockets surrounding the waveguides by flexing the mold in these regions upwards, as shown in Figure 5.10 (a) and (b). The regions of greatest rigidity to vertical forces are the sidewalls of the waveguide structures, and although they might deform laterally slightly, they do not buckle and are in close contact to the substrate. Therefore the residue is thinnest in the regions immediately surrounding the waveguides, and the residue is thickest between two far-apart waveguides. In Figure 5.10 (c), we show a top-view microscope image of a molded waveguide. The previously noted phenomenon is observable in this image: the dark colored waveguides are immediately surrounded by light color, corresponding to a very thin residue. Further from the waveguide, the residue gets thicker, shown as a darker color. The ramifications of this effect in soft-mold replica molding are significant for optical applications. The simulations presented above are worst-case, upper-bound scenarios and the actual waveguide performance is better than what the simulations predict. This result does not invalidate the importance of reducing the background residue, however.

In conclusion, soft lithography replication is a good technique for inexpensive, fast, mass fabrication of polymer integrated optical devices. The resolution requirements have been previously demonstrated. The major remaining fabrication difficulty preventing wide-spread polymer device replication is the unavoidable residue remaining after the molding process. For rational polymer waveguide cross-sectional parameters, we calculate that a small residue up to several hundred

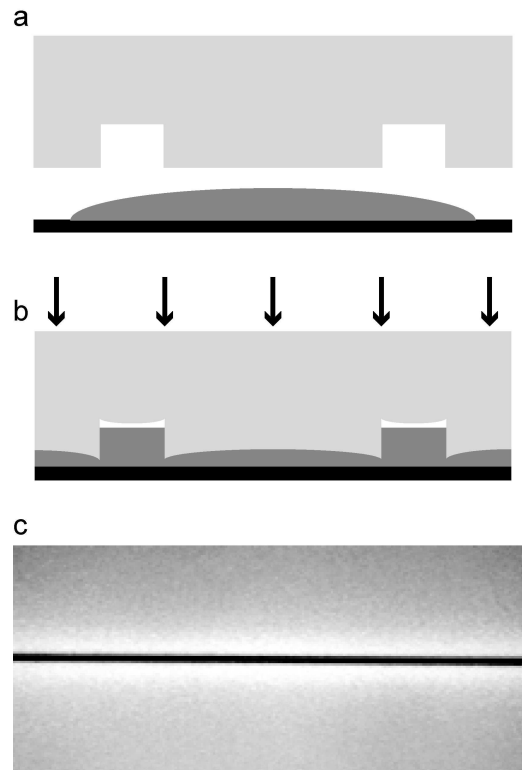


Figure 5.10: Formation of background residue. In (a) the PDMS mold and polymer solution before molding. In (b) the mold is pressed atop the solution/substrate, forming the waveguide structures, but leaving a polymer residue layer surrounding the waveguides. In (c), optical microscope image showing a waveguide (black) surrounded by thin residue (white) that gets thicker farther from the waveguide (gray). The measured thicknesses correspond to the gray areas, the areas of thickest residue.

nanometers is tolerable. Beyond several hundred nanometers of residue, waveguides become multimode, directional couplers do not exhibit the intended coupling ratios, and waveguide bends exhibit exorbitant losses. To correct the problem of the residue, the use of dilute polymer solutions greatly reduces the residue. Applying more force to the mold during the formation of the waveguides does not affect the thickness of the residue. The force does affect the conformal contact of the mold to the substrate. Finally, the molded devices yield structures with the residue being thinnest immediately surrounding the waveguides because for the aspect ratios of waveguides, there is little lateral deformation of the mold and no buckling of the waveguide walls. The thinness of the residue surrounding the waveguides will tend to reduce the deleterious effects predicted by the simulations.

5.3 Polymer Microring Resonators Fabricated by Replica Molding

Among integrated optical circuits, the microring optical resonator is a key device for optical communications. Due to the resonant nature of microrings, light of certain wavelengths can be canceled by interference, resulting in periodic notches of the transmission spectrum (see Section 3.2). There are several reports of polymeric microring resonators. The typical fabrication procedure uses reactive ion etching (RIE) [42] to form the guiding structures, similar to the fabrication methods of semiconductors. A potential disadvantage of RIE for polymeric devices is that waveguide scattering loss can be significantly increased due to dry etching processes. An alternative method for making polymeric microrings is an imprinting technique in which the polymer reflows at high temperature and fills a hard mold with “negative” relief features [93]. However, this method also requires complicated etching processes to get a proper mold.

In the following, we demonstrate the comparison of a master microring optical resonator device made by electron beam lithography to the replicated devices made by soft lithography, using the same materials. The results show that soft lithog-

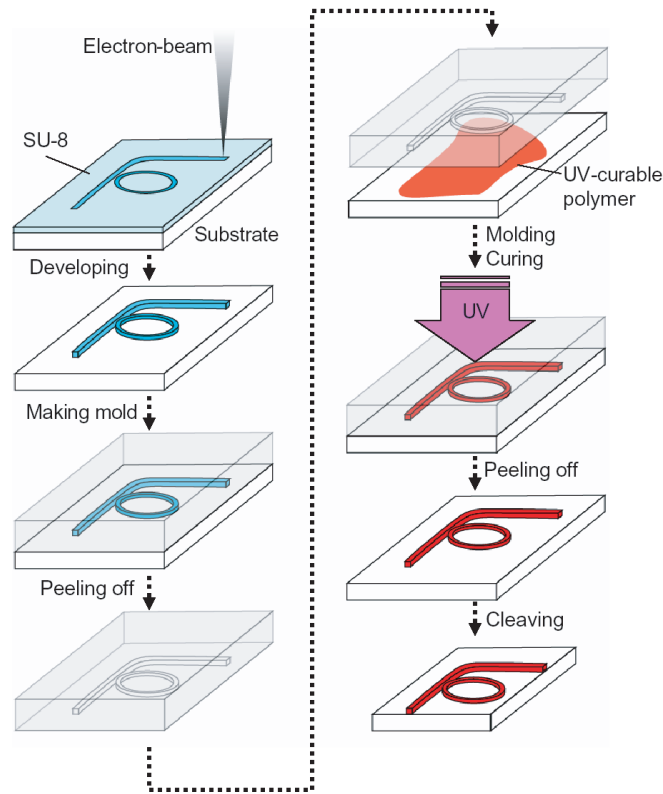


Figure 5.11: Schematic diagram of fabrication processes. Generally, the ultraviolet curable polymer can be either the same material used for electron beam lithography or different ones.

raphy meets the rigorous requirements of high-precision fabrication for integrated optical devices.

5.3.1 Fabrication and Measurement

Figure 5.11 is the flowchart of fabrication processes used in this section. Briefly, we make the master devices by electron beam lithography and replicate them using a PDMS mold to form the devices in the same materials as the master. The substrates are silicon wafers covered with a $5\ \mu\text{m}$ thermally grown amorphous silica film (refractive index 1.445). A thin film ($2\ \mu\text{m}$) of SU-8 (refractive index 1.565) is

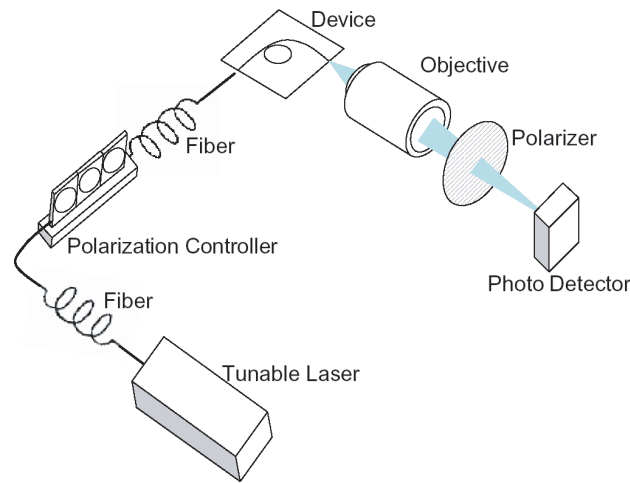


Figure 5.12: Optical setup for transmission measurement.

spin coated on the substrates and exposed by electron beam lithography to form the master device. After developing in SU-8 developer, the structure is covered by PDMS and baked at 80°C for 1 h. Once cured, the PDMS mold is peeled off. To mold the replicas, a drop of SU-8 is placed onto a new silica substrate and stamped with PDMS mold. The replicated device is cured under ultraviolet light until solidified. Both the master and replicated devices are cleaved to expose the waveguide end-facets for optical measurement.

The measurement setup is shown in Figure 5.12. Light from a tunable laser is coupled into one end of the straight waveguide using a tapered fiber (also see Figure 5.13). The transmission signal, collected by an objective from the other end facet of the device, is measured using a femtowatt infrared photoreceiver.

Both master devices (fabricated by electron beam lithography) and molded devices (by soft lithography) are tested under the same conditions. Figure 5.13 shows that the PDMS mold can successfully reproduce the details of master devices and transfer to molded ones.

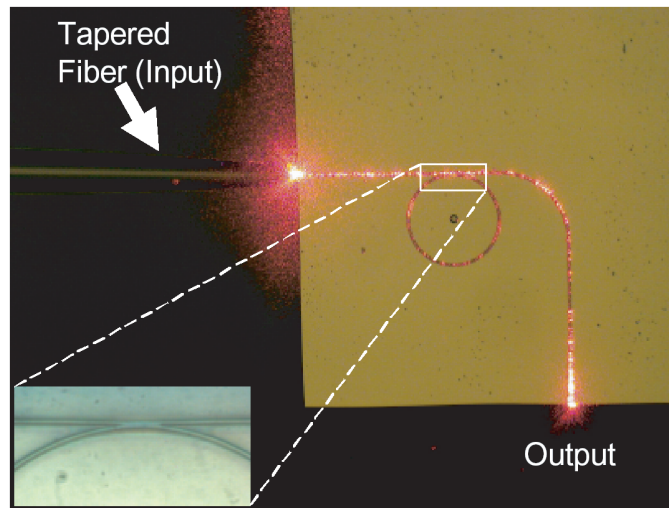


Figure 5.13: Optical microscope image of microring optical resonator fabricated by soft lithography. The inset shows the detail of coupling region. The ring diameter is designed to be $200\ \mu\text{m}$ and the waveguide width is $2\ \mu\text{m}$. Light from a He-Ne laser is input into the device for illustration only.

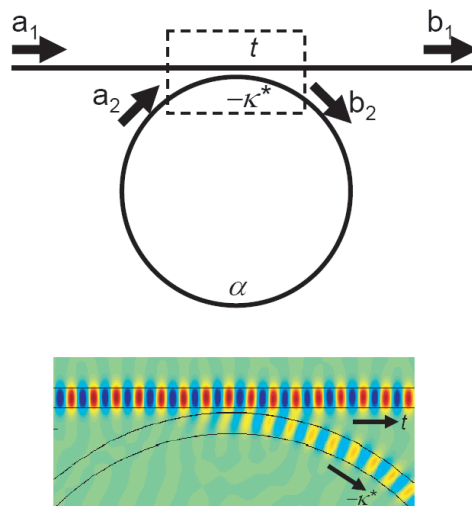


Figure 5.14: Schematic geometry for waveguide ring resonator coupling. The color plot is a finite-difference time-domain simulation of the coupling between the straight waveguide and the ring.

5.3.2 Results and Discussion

The generic geometry of a microring optical resonator is illustrated in Figure 5.14. The evanescent coupling of light between the waveguide and the ring is analyzed by well-known coupled mode theory. As shown in Section 3.2, the transmission of the device is

$$\left| \frac{b_1}{a_1} \right|^2 = \frac{\alpha^2 + |t|^2 - 2\alpha|t| \cos \theta}{1 + \alpha^2|t|^2 - 2\alpha|t| \cos \theta}. \quad (5.1)$$

At resonance, i.e., $\theta = m2\pi$, m an integer, the equation above can be written as

$$\left| \frac{b_1}{a_1} \right|^2 = \frac{(\alpha - |t|)^2}{(1 - \alpha|t|)^2}. \quad (5.2)$$

The condition $\alpha = |t|$, i.e., the critical coupling condition that results in a null of the output is the desired condition for a microring resonator optical filter. In practice, for a given microring structure, α is determined by the material loss and the bend loss. To achieve critical coupling, the coupling (represented by t) must be tuned by varying the gap between the straight waveguide and the microring. Precise duplication of this parameter is key to good replication of the master device.

The two transmission spectra shown in Fig. 5.15 are attributed to the master and the molded replica devices. The shapes of transmission spectra are clearly quite similar. Furthermore, the extinction of the notches which is extremely sensitive to the coupling between the straight waveguide and the microring resonator are almost the same (~ -9 dB), indicating that the soft lithography method precisely replicates the master devices on the nanometer scale. The obvious difference in the spectra of the master and molded replica devices is the shift of notch positions due to slightly different free spectral ranges (FSRs). We attribute these differences to small discrepancies between the effective refractive indexes of the two devices. The difference of effective refractive index is about 5×10^{-4} according to this measurement. In practical applications where active material is used, this shift could be controlled by a bias voltage.

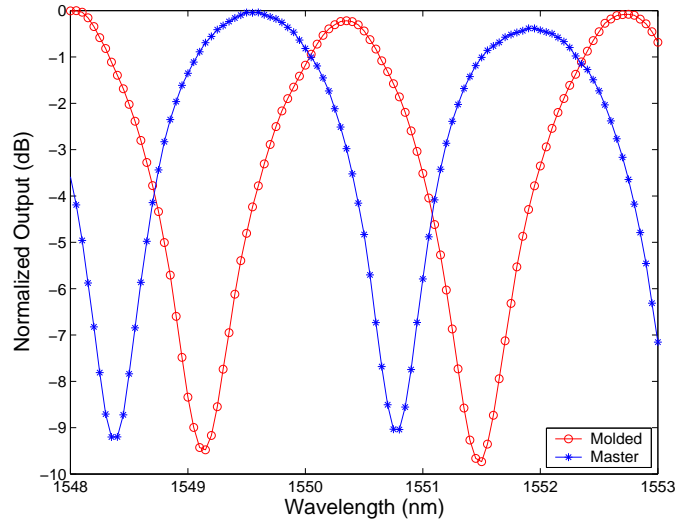


Figure 5.15: Comparison of transmission spectra of the master (blue) to molded (red) ring resonator.

In conclusion, microring optical resonators are fabricated by electron beam lithography and replicated by soft lithography. Evaluating the quality of the replication, we demonstrate excellent agreement in the optical properties between molded replicated devices and master devices. This result shows the potential of soft lithography for industrialized integrated optical circuit fabrication. Compared to conventional fabrication methods currently used for polymer integrated optics, soft lithography shows promise by not only achieving the requirement of precise fabrication, but also of decreasing the fabrication cost through low material costs and high fabrication throughput.

5.4 Multilayer Molding

Integrated optical devices, especially planar lightwave circuits (PLCs), are important elements of modern communications and networking. Conventional PLCs are two-dimensional photonic circuits and the degree of integration is limited by the size of the devices. Stacking PLCs to make three-dimensional (3D) structures

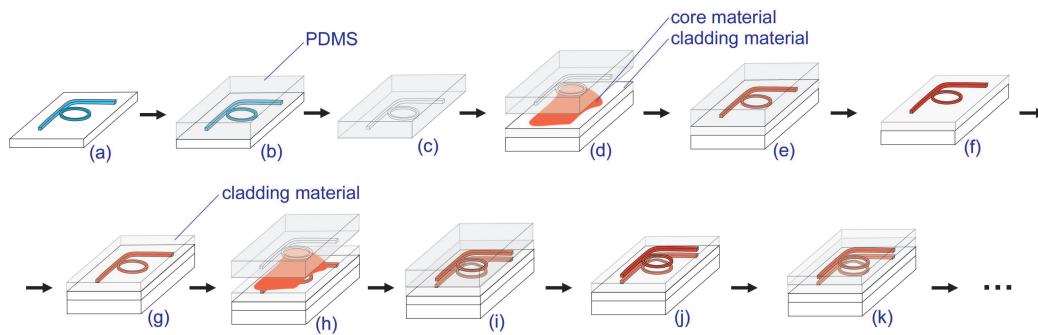


Figure 5.16: Schematic flowchart of the fabrication of 3D integrated optical microchips.

will efficiently increase the density of photonic circuits. Polymers, as one class of promising materials for the next generation of optical devices, have been investigated for several years [4]. Several polymer 3D integrated optical devices have been realized by conventional lithography [102, 103]. As shown in the preceding sections, soft lithography has been applied to fabricate high quality polymer integrated optical devices. Soft lithography has also been shown to be a powerful method for generating 3D multilayer structures [104, 105]. In what follows, we describe and demonstrate the development of a multistep soft lithography method to fabricate 3D multilayer integrated optical devices.

5.4.1 Fabrication and Measurement

The schematic fabrication procedure of the multistep soft lithography is shown in Figure 5.16. A poly(dimethylsiloxane) (PDMS) stamp, which constitutes a negative relief of the device, is used as the mold to reproduce the polymeric core structure. In our demonstration, electron beam lithography of SU-8 is used to generate the master structures of the core layers, shown in Figure 5.16(a). PDMS prepolymer (RTV-615, GE) is poured on and cured (Figure 5.16(b)) to form the mold. After cooling to room temperature, the cured PDMS layer can be easily peeled off (Figure 5.16(c)), preserving the original master, to serve as the soft

mold. A polymer with a lower refractive index such as OG-125 (Epotek, $n=1.46$) is spun on a silicon wafer and cured by ultraviolet light, serving as the lower cladding layer (Figure 5.16(d)). A drop of the solution of the core polymer with a higher refractive index is placed upon the cladding layer and the PDMS mold is pressed on the substrate (Figure 5.16(e)) until the solidification of the core is complete. By releasing the PDMS mold, the core structure – identical to the master device – is formed (Figure 5.16(f)). Another layer of OG-125 material is spun atop the core layer just molded (Figure 5.16(g)) to serve as both the upper-cladding for the first core layer underneath and the under-cladding layer for the second core layer. By repeating the molding-cladding procedure (Figure 5.16(h-k)), a two-layer structure is fabricated. The thickness of the cladding layer between the two core layers can be adjusted by changing the parameters of the spin-coating and the concentration of the cladding solution. By choosing the correct cladding material and film thickness, the crosstalk between the core layers can be adjusted or avoided. This procedure can be repeated to fabricate 3D multilayer structures with more than two layers.

There are several intrinsic advantages of applying the multistep soft lithographic method to fabricate integrated optical devices. First, compared with the other fabrication methods for 3D optical devices such as multilayer grayscale optical lithography [102] and two-photon lithography [106], our multistep soft lithographic method has obvious cost advantages. Furthermore, multistep soft lithography allows for the application of different core structures for the layers and integration of various optical functions on a single chip. As shown in Figure 5.17(a), we fabricated a three-layer integrated optical microchip with a different structure in each layer. The lower layer (layer 1) is a waveguide Y-splitter made of amorphous polycarbonate ($n=1.60$). The molding solution is a dibromomethane solution containing 2 wt.% polycarbonate. The middle layer (layer 2) is a ring resonator optical filter (ring diameter 400 μm) made of polystyrene ($n=1.60$). This core layer is molded from a 4 wt.% toluene solution of polystyrene. The upper layer (layer 3) is a waveguide made of SU-8 ($n=1.57$) by ultraviolet curing during the

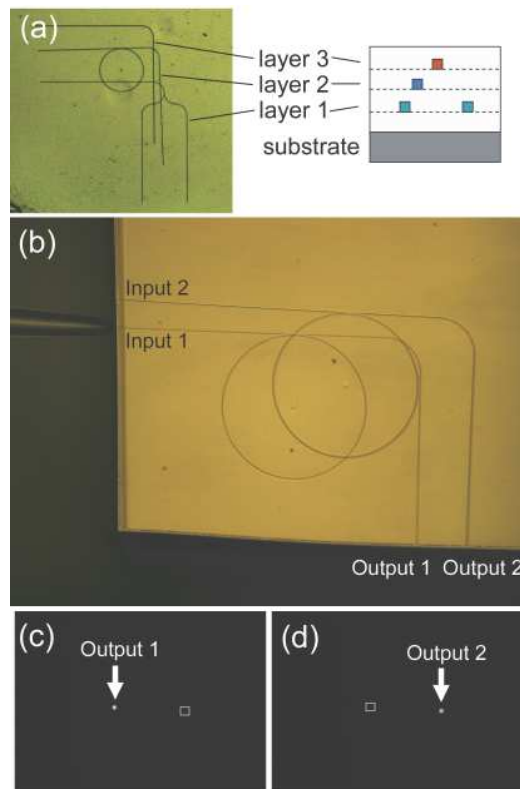


Figure 5.17: Optical microscope images of multilayer devices. A three-layer microchip and its schematic structure are shown in (a). Each layer consists of a different polymer material. A two-layer microchip containing a microring resonator optical filter in each layer is shown in (b). (c) and (d) are infrared camera images of the outputs of the microring resonator filters in the upper layer (input/output 1) and in the lower layer (input/output 2), respectively. The squares in (c) and (d) are the positions of the end facets of the other output.

molding step. The four cladding layers between which three different core layers are fabricated, are all made of OG-125. This chip with three different core structures and different core materials can be fabricated by multistep soft lithography using only PDMS molds and a press, and each mold can be used hundreds of times for reproduction. With conventional etching techniques, this chip would require complicated and lengthy processing. Moreover, in contrast to conventional top-down etching methods, the bottom-up method is more suitable for constructing 3D structures on existing devices, which may be important for hybrid optoelectronic integration.

In order to investigate the optical properties of each layer of the multilayer structure, we fabricate a two-layer microchip in which both layers have microring resonator optical filters molded from the same PDMS mold. The microring resonator optical filter consists of a straight waveguide evanescently coupled to a filtering waveguide ring. As we have seen in Section 3.2, when the coupling between the straight waveguide and the ring reaches the critical coupling condition, the resonance wavelengths will be completely attenuated at the output of the waveguide.

Figure 5.17(b) shows the optical microscope image of the 3D microchip containing two layers of microring resonator optical filters. Each optical filter has an input end and output end (Input 1 and Output 1 in Figure 5.17(b) belong to the upper layer, while Input 2 and Output 2 belong to the lower layer), and the end facets are prepared by cleaving the silicon substrate. The cores of the microring resonator optical filters are made from SU-8 and the cladding layers are OG-125. The cross section of the core waveguides is $2\ \mu\text{m} \times 1.6\ \mu\text{m}$ and the OG-125 layers are $3\ \mu\text{m}$ thick. Light from a tunable laser is coupled into one of the inputs through a tapered single-mode fiber and optical transmission from the outputs are collected by a $10\times$ aspherical objective and then detected by an IR photodetector. The tapered fiber can be controlled by a moving stage to selectively couple the laser into one of the two inputs of the chip. When the laser is coupled into Input 1 (upper layer), we observe light at Output 1 (Figure 5.17(c)). When we

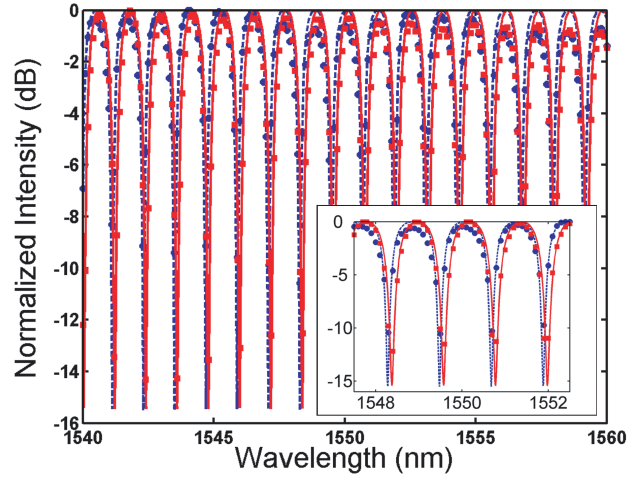


Figure 5.18: Transmission spectra of the microring resonator optical filters in the two layers of the microchip, as shown in Figure 5.17(b). The experimental data are shown as solid circles (lower layer) and solid squares (upper layer). The solid line and dashed line are the fitting curves of experimental data of the upper layer and the lower layer, respectively. The inset shows detailed spectra around 1550 nm.

move the tapered fiber to the lower layer and couple the light into Input 2, an output is observed at Output 2 (Figure 5.17(d)). The position of the end facet of the waveguide in the layer that we have not coupled light into has been marked by a square in the images to indicate the horizontal and vertical displacement. Both images show the good mode confinement of the SU-8 waveguide surrounded by OG-125 cladding, indicating that the refractive index contrast is suitable for single mode transmission. Finite difference simulations (see Appendix B) confirm the waveguides are single-mode near 1550 nm. By design, no crosstalk is observed in the experiment due to the thick cladding layer between the core layers.

5.4.2 Results and Discussion

Figure 5.18 shows the transmission spectra of the dual-layer microring optical filter chip. In order to achieve the critical coupling condition, the gap between the straight waveguide and the ring resonator is designed to be 400 nm. Both spectra show periodic notches with extinction ratios of around -15 dB, indicating that the critical coupling condition is nearly achieved with our design and fabrication. Besides the extinction ratio which is extremely sensitive to the fabrication accuracy, the two spectra are also similar in terms of their free spectral ranges (FSRs) and shapes. The FSRs of the lower layer and the upper layer are both measured to be 1.201 nm. The unloaded quality (Q) factors of the two microring resonators are estimated by data fitting to be around 1.0×10^4 . The similarities indicate that the two layers of microring resonator optical filters are nearly identical. The 0.1 nm offset between the two spectra is due to slightly different effective refractive indices. According to the data fitting of the two spectra, the difference in the effective refractive indices is 0.0001. The essentially identical microring resonator optical filters in this dual-layer device shows the significant accuracy and fidelity of soft lithography, as well as the potential of polymer integrated optical devices in 3D optical circuits.

In summary, our experimental demonstration of 3D multilayer integrated optical devices made by multistep soft lithography points the way to highly integrated multilayer optical circuits which can be easily fabricated with low cost polymer materials. Through a highly efficient and well-controlled soft molding process, planar lightwave circuits with various functionalities in different materials can be stacked together to form high-density multifunctional optical chips.

Chapter 6

Electro-Optic Polymer Mach-Zehnder Modulators

6.1 Introduction

In the preceding chapter, the demonstration of replica molding for the fabrication of polymer integrated optics was applied only to passive polymer materials. While passive polymers are useful in their own right, they do not take advantage of a property that renders polymer-based devices interesting to the optics-based communications industry. That property is the ability to achieve extraordinary electro-optic efficiencies in polymer materials by doping certain passive polymer hosts with highly electro-optic chromophore molecules. These polymer materials promise the advent of incredibly high-bandwidth and very low switching voltage electro-optic modulators for future high-speed communications systems. The demonstration of such devices fabricated by replica molding is crucial in proving the usefulness of this method for polymer integrated optics. Upon this proof, the advantage of electro-optic polymers is not only found in high bandwidth and low switching voltage, but also in robust and extremely high throughput fabrication.

Since electro-optic polymers are not generally photocurable themselves, fabrication of polymer modulators has been mostly limited to traditional semiconductor etching techniques such as reactive ion etching. An alternative fabrication technique that takes advantage of the plastic nature of electro-optic polymers is the

soft-stamp replica molding lithography discussed in the previous chapter. Materials fabricated by this method can be either photo-curable due to the transparency of the stamp material to ultraviolet light, or solidified by solvent evaporation made possible by the permeability of the stamp material to common polymer solvents. Previously, this technique has been employed to make optical couplers [88] and polymer distributed feedback and distributed Bragg reflector lasers [89] for use in the visible regime. For infrared applications, this technique has been applied to optical interconnects [92] and microring resonator optical filters [20] as demonstrated in Chapter 5.

In this chapter, the method of replica molding is applied to electro-optic polymers. A brief introduction to electro-optic guest-host polymers is first given. These materials in their basic state do not exhibit electro-optic properties, so poling of these materials is necessary to align the dopant molecules. The method of corona poling is explained. This is followed by a proof-of-principle, prototype electro-optic polymer modulator fabricated by replicating a small Mach-Zehnder structure patterned by electron beam lithography. Although the prototype proves the principle, it is not a worthy example of the ability of the molding method. Thus, a full size electro-optic polymer Mach-Zehnder modulator is fabricated by replica molding of a master patterned by photolithography. Measurements of this device prove the ability to make industry-grade polymer electro-optic devices using the molding method.

6.2 Electro-Optic Polymers

Organic nonlinear optical materials have been the subject of significant recent technological advances with the aim of commercial deployment, especially for telecommunications applications [107]. Polymers for integrated optical circuits exhibit several advantageous features. The raw materials are lower in cost than their crystalline and semiconductor counterparts and offer more flexible fabrication methods [4]. Electro-optic polymers have low material dispersion and thus, low velocity mis-

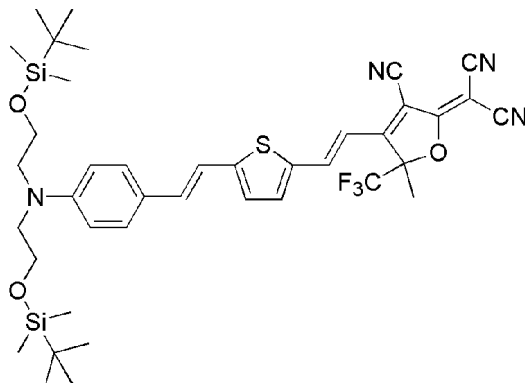


Figure 6.1: The chemical structure of AJL8 chromophore.

match between optical signals and microwave modulation, allowing electro-optic modulation bandwidths up to 1.6 THz [13]. The chromophore dopants responsible for the nonlinear optical characteristics are devised to achieve high nonlinearities, allowing for modulators with switching voltages of less than 1 V [12]. Recent advanced chromophore design has resulted in the development of highly nonlinear chromophores with good thermal- and photo-stability [107]. Shown in Figure 6.1 is the chemical structure of one such newly developed chromophore, referred to as AJL8 [108]. Films of AJL8 doped in an amorphous polycarbonate matrix exhibit a very high r_{33} value of 94 pm/V at 1300 nm. The onset degradation temperature was found to be 220 °C and around 80% of its original r_{33} value maintained very constantly for more than 500 hours at 85 °C [108].

Most polymers are not in and of themselves electro-optic. Rather, the polymer must host dopant molecules such as the AJL8 molecule shown in Figure 6.1 that do exhibit electro-optic activity. These hybrid materials in which electro-optic molecules are mixed with polymer hosts are termed *guest-host* electro-optic polymers. Alternatively, in an attempt to stabilize the materials against environmental and chemical damage, the electro-optic molecules can be attached to the polymer backbone, or locked into position by crosslinking the polymers while the dopants are in collective alignment [109]. Guest-host materials, however, have been shown to be remarkably reliable over long periods of time at elevated temperatures and

in several ambient environments [108, 110].

The dopant molecules that exhibit electro-optic effects are typically dye, or *chromophore*, molecules that strongly absorb light at certain wavelengths. Among the earliest of the electro-optic chromophores was the commercially available Disperse Red 1 dye. Recently, however, materials scientists and chemists have become interested in the development of new, more highly nonlinear chromophores. The microscopic properties that result in strong macroscopic electro-optic effect are a large dipole moment (μ) and large first hyperpolarizability (β). The large dipole moment is important in the alignment of the molecules, to be discussed in the following section. The microscopic hyperpolarizability β is related to the second-order susceptibility $\chi^{(2)}$ by the relation [107]

$$\chi_{zzz}^{(2)} = N\beta f(\omega) \langle \cos^3 \theta \rangle \quad (6.1)$$

and

$$\chi_{zxx}^{(2)} = N\beta f(\omega) \langle \cos \theta \rangle \langle \cos^2 \theta \rangle \quad (6.2)$$

where N is the chromophore number density, $f(\omega)$ takes into account how the local field is attenuated by the local environment of the chromophore, and the cosine terms are the order parameter related to the alignment of the molecules. $\chi_{zzz}^{(2)}$ and $\chi_{zxx}^{(2)}$ are used to define the electro-optic coefficients r_{33} and r_{13} , respectively. Thus, in developing the newest generation of chromophores for electro-optic devices, enhancement of β via quantum mechanical calculations and molecular engineering will ensure higher nonlinearity and more efficient devices. In the simplest picture, an increase in the molecular hyperpolarizability is obtained by increasing the length of the *pi*-electron system [107].

6.2.1 Poling of Guest-Host Electro-Optic Polymers

Once the chromophores have been designed and synthesized, the objective in maximizing the electro-optic efficiency is to create a film of highly ordered molecules – that is, to maximize the order parameter $\langle \cos^3 \theta \rangle$. The chromophores are ini-

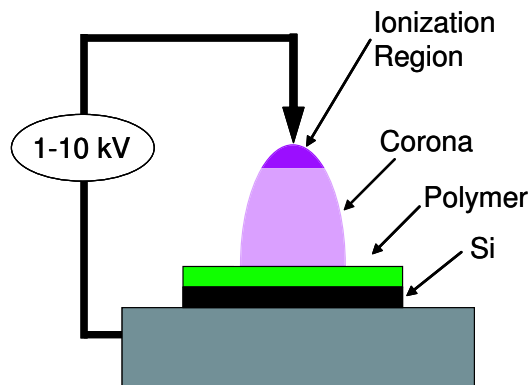


Figure 6.2: Schematic diagram of the corona poling method for alignment of the chromophores in guest-host electro-optic polymers.

tially mixed with the polymer in a solvent. This solution is spun onto a substrate, consisting of a lower cladding atop some foundation material such as silicon. The spun film is amorphous and cannot exhibit electro-optic activity. To orient the molecules in the film, obtaining a collective electro-optic effect, one must make use of the dipolar properties of the chromophores. This alignment of the chromophores is known as *electric field poling*. In this procedure, the polymer is heated to a temperature near its glass-transition temperature. At this elevated temperature, the polymer material becomes soft and allows for reorientation of the chromophores. This is done by subsequently applying a strong electric field that rotates the dipolar molecules into alignment with the field. At this point, the temperature is allowed to drop to room temperature, effectively locking the molecules into proper alignment. As the temperature of the film reaches room temperature, the electric field is turned off and the sample removed.

There are two common ways in which to accomplish electric field poling. One method is the contact poling method. In this case, the voltage is applied directly to metallic contacts previously deposited on the film surface. These contacts are generally also used for microwave driving fields in electro-optic polymer modulators, and so this method is a good choice for such structures. Further, in contact poling, the poling is limited to areas covered by the electrodes. This allows for sep-

arate contacts to be at different voltages on the same device. In this way, two arms of a Mach-Zehnder interferometer can be poled oppositely by applying a positive voltage on one arm and a negative voltage on the other. This is commonly used for low voltage polymer modulators in which this “push-pull” operation results in a factor of two decrease in the switching voltage [12]. A limitation of the contact poling method is that lower poling fields are achieved compared to other methods. In addition, the spatial field distribution of the poling field can be an issue for certain structures.

The second method of electric field poling, illustrated in Figure 6.2, is corona poling [109]. A corona is defined as self-sustainable, non-disruptive electrical discharge due to partial dielectric breakdown of a gas. To create the corona, a metallic needle is positioned several centimeters from the film surface. A voltage of several kilovolts is applied to the needle, while the silicon substrate is grounded. The large field between the needle and the ground plane ionizes the molecules of the gaseous environment and accelerates the ions towards the film surface. The ions build up upon the film surface, thereby creating a very strong electric field across the film. An advantage of this method is that stronger fields can be achieved across the polymer films, leading to better poling efficiencies and better performing devices [107]. Further, the method allows for large area poling across (e.g., 6 or 8 inch wafers) with good uniformity. This is important for mass production of poled electro-optic devices.

It is important to monitor and limit the corona current in the poling process to avoid full breakdown of the environment. If this occurs, a violent discharge damages the film and renders any further poling impossible. The environment in which one practices the corona poling is of great importance. The environment is important because poling in an oxygen rich environment results in infiltration of the film with oxygen molecules that electrochemically damage the chromophores and reduce the electro-optic effect. Therefore, it is of interest to perform the poling in an inert gas environment, thereby purging the damaging oxygen. Shown in Figure 6.3 are measurements of the current as a function of the tip-to-sample

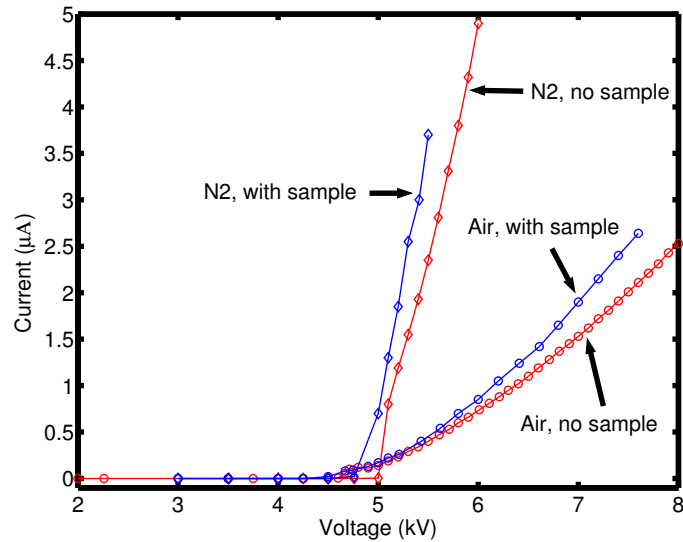


Figure 6.3: The corona current versus the tip-to-sample voltage in both nitrogen and ambient environments, with and without the sample present.

voltage in a nitrogen and in an ambient environment. It is seen that the current increases much more rapidly in the nitrogen environment. This results in stability problems and in the increased likelihood of full dielectric breakdown.

An appropriate method of characterizing the efficiency of the poling of the polymer films is required. Easily observable in the laboratory, second-harmonic generation provides a rapid test of the poling quality. Using the output of a Nd-YAG laser ($\lambda = 1064$ nm) as the fundamental beam impinging on the poled electro-optic polymer film, the second-harmonic at 532 nm can be measured. Since the second-harmonic intensity is proportional to the square of the nonlinear coefficient, one can compare the measurement of the polymer film to that of a baseline material such as lithium niobate.

6.3 Prototype Polymer Electro-Optic Modulator Fabricated by Soft-Stamp Replica Molding Using the CLD-1 Chromophore

As discussed in the previous chapter, soft lithography, which utilizes a master device to generate several soft molds each used to reproduce identical replicas, has been extensively developed during the past ten years and has shown promise for improving optical waveguide manufacturing throughput [111]. This simple method has been applied in a number of fields to transfer and reproduce micro- or nanometer patterns and features. The limiting feature size can be on the order of 1 nm [87], indicating that soft lithography is a competent technique for producing high-quality polymer integrated optical devices.

Here we demonstrate a prototype Mach-Zehnder interferometer modulator fabricated by soft lithography. For this prototype device, we employ electron beam lithography to prepare the master device. This limits the overall device size to the small field of view of an electron beam microscope. However, this method is used to rapidly produce a prototype device. A brief description of the fabrication process is given in the next subsection. For the full description, see Section 6.4.

6.3.1 Fabrication and Measurement

The structure of the device is shown in Figure 6.4. A guest-host material, CLD-1/APC, is used as the electro-optically active polymeric material core. The dopant molecule is CLD-1 [110], and the passive host polymer is amorphous polycarbonate (APC). The total length of the active section of the interferometer, limited by the electron beam lithography system, is restricted to 2 mm. We directly pattern the master Mach-Zehnder interferometer in a 2 μm SU-8 film on a silicon substrate. After developing and hard baking, this structure is used to make the PDMS mold. A 200 nm thick Au layer was deposited onto the Cr coated (10nm) silicon substrate, serving as the bottom electrode. A 5 μm layer of UV15 is spun onto the Au, serving as the lower cladding. After one minute of ultraviolet exposure and post

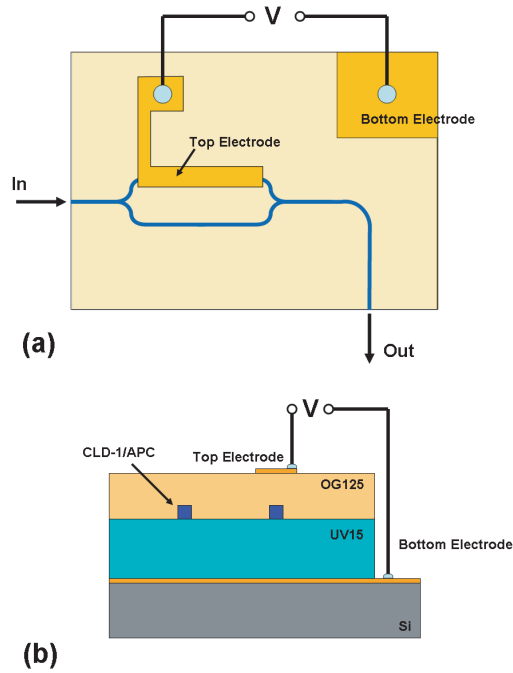


Figure 6.4: The structure of the polymeric Mach-Zehnder interferometer modulator: (a) Top view, (b) Side view.

baking at 310K for 30 minutes, the UV15 cladding is fully cured. A drop of CLD-1/APC guest-host polymer dissolved in trichloroethylene solution is placed onto the UV15 cladding layer and stamped by the PDMS mold with pressure 2×10^5 Pa for 20 minutes to form the core waveguide. After the PDMS mold has been released, OG-125 ($3 \mu\text{m}$) is spun on the molded device serving as the upper cladding. After the OG-125 layer is cured by ultraviolet exposure, the entire structure is heated near the glass-transition temperature of APC and poled by a corona poling setup. The poling voltage is set to 8 kV and the distance between the corona electrode and the sample is 2 cm. The temperature is increased to ~ 140 °C, and both the temperature and poling voltage are kept constant for 30 minutes. The poling voltage is applied continuously while the temperature is allowed to drop to room temperature, fixing the orientation of the chromophores in the polymer waveguide. The concentration of the second-order nonlinear optical

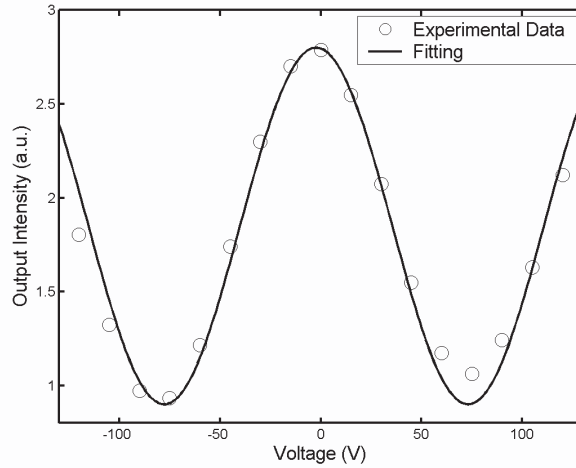


Figure 6.5: Halfwave voltage measurement from a 2 mm soft lithographic Mach-Zehnder interferometer modulator device.

chromophore CLD-1 is optimized for the best electro-optic effect, according to the investigation on the competition of intermolecular electrostatic and poling-field interactions for guest-host polymer materials [112]. The measurement setup of the Mach-Zehnder interferometer modulator device is similar to that of the microring resonator, except the wavelength is fixed and a voltage is applied to one arm of the modulator.

6.3.2 Results and Discussion

The intensity of the output signal is changed by the applied voltage as shown in Figure 6.5. The figure shows that the halfwave voltage (V_π) of our modulator is about 80 V. This number is unacceptably high for practical applications; however, there are several reasons for this high value. The practical figure of merit for electro-optic modulators is the halfwave voltage times the active length, $V_\pi L$. In our case this figure of merit is 0.16 Vm, corresponding to 8 V for a 2 cm active section. The voltage will also be proportionally reduced by reducing the overall film thickness. Optimized poling will further reduce V_π . Finally, using a

push-pull electrode configuration will result in another factor of two reduction in V_{π} . Accounting for these considerations, our results indicate that soft lithography is suitable for making low-cost, high fabrication throughput polymeric optical intensity modulators.

6.4 Low-Voltage Polymer Electro-Optic Modulator Fabricated by Soft-Stamp Replica Molding Using AJL8 Chromophore

In the previous section, a prototype of a polymer electro-optic modulator was fabricated using the rapid and simple procedure of soft-stamp replica molding. That a working modulator can be produced by this fabrication method was demonstrated. However, to truly demonstrate the usefulness of the method for devices useful in the telecommunications industry, a lower operating voltage device must be demonstrated. In what follows, a larger Mach-Zehnder interferometer modulator fabricated by soft-stamp replica molding is demonstrated. To further improve the properties of the device, a newly developed chromophore material – AJL8 shown in Figure 6.1 – is employed to enhance the low-voltage properties and the temperature stability of the device.

6.4.1 Fabrication and Measurement

The first portion in the replica molding process (shown in Figure 6.6 (a-c)) is the production of a mechanically flexible poly(dimethylsiloxane) (PDMS) stamp. Because of the low surface energy of the elastomer stamp material, the master device to be replicated can be made of many commonly used resist, glass, or semiconductor materials. Ultraviolet lithography of photoresist is frequently used for patterning the master device. For smaller and higher resolution structures, electron beam lithography can be used. Liquid PDMS is poured atop the master structure and cured for two hours at 80 °C. The cured PDMS stamp is peeled from the master device and diced to the required size. Since the curing and peeling of

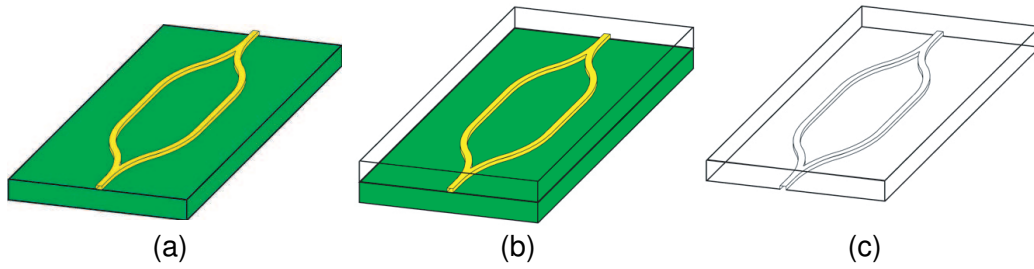


Figure 6.6: Fabrication of the PDMS stamp. A master MZI device (a) is patterned by photolithography of SU-8. PDMS is poured on the master device (b), cured, peeled, and diced (c).

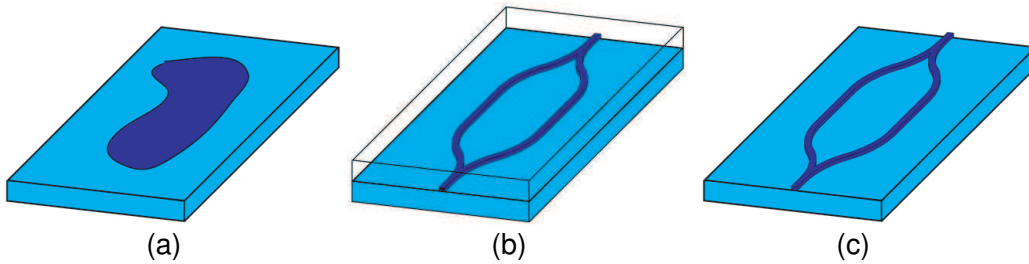


Figure 6.7: Procedure for making the replica from the mold. A drop of electro-optic core solution is placed on the appropriate substrate (a). The PDMS stamp is depressed (b) until the core polymer is cured. The stamp is peeled to reveal the high-fidelity replicated device (c).

the PDMS stamp does not alter the original master, the master can be used to make additional stamps by repeating the preceding steps.

The replication procedure is shown in Figure 6.7 (a-c). Similar to the case of the master device, the low surface adhesion and the chemical inertness of the PDMS allow virtually any polymer material in many solvents to be used for the replication. A droplet of the core polymer solution tens of μL in volume is placed on an appropriate substrate. The PDMS stamp is depressed on the solution/substrate, while monitoring the force with a force gauge. The force applied should be sufficient to ensure conformal contact between the stamp and the substrate; however,

previous results suggest that the molded features are relatively immune to variations in pressure, so the actual force beyond what is required for conformal contact is not relevant [19]. After the solvent of the core polymer solution has evaporated through the PDMS, the stamp is removed from the substrate, revealing a high-fidelity replica of the original master device.

The structure patterned by replica molding is a Mach-Zehnder interferometer (MZI), shown schematically in Figure 6.7(c). A Y-junction equally divides the input light between the two arms of the interferometer and another Y-junction combines the light having traversed two different optical path lengths. Each Y-junction consists of two S-shaped bends with bend radii of 1 mm, ensuring low radiation loss. The interferometer arms are 2 cm in length. The MZI masters are exposed by photolithography of SU-8 on a silicon substrate. The masters are baked at 150 °C for one hour to smooth nanometer scale sidewall and surface imperfections. Two complete MZI structures comprise each mold with a total mold size of 3.8×1.8 cm.

The core polymer is composed of the aforementioned AJL8 chromophore as the nonlinear optical dopant in amorphous polycarbonate (APC, Aldrich). APC has been shown to have excellent thermal stability as a polymer host material [107]. The ratio of chromophore to passive polymer was 20 wt.% as in Reference [108]. A final solution concentration of 1.6 wt.% was achieved by dissolving the solid in dibromomethane, yielding a solution with a moderate evaporation rate appropriate for the replica molding process.

The cross-sectional view of the replica molded electro-optic waveguide structure is shown in Figure 6.8. The silicon substrate is coated with Cr and Au, serving as the bottom electrode. A lower cladding layer is necessary to optically isolate the guided light from the metal electrode. The challenge in choosing low refractive index polymer for the lower cladding is that it must be chemically resistant to the core polymer solution solvent. There exists a similar difficulty with the upper cladding polymer as its solvent must dissolve neither the core polymer nor the lower cladding. A commercial ultraviolet-curable epoxy, WR-513 (Luvantix,

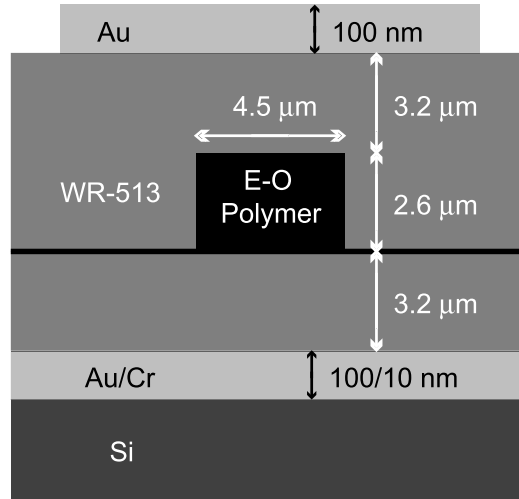


Figure 6.8: Cross sectional view of the electro-optic waveguide structure. The core electro-optic polymer is AJL8/APC and the upper and lower cladding materials are low refractive index epoxy WR-513.

$n=1.50$), is spun to a thickness of $3.2 \mu\text{m}$ for the lower cladding. The film is cured under an ultraviolet lamp for five minutes and baked at $100 \text{ }^\circ\text{C}$ for two hours to lattice-harden the film, ensuring resistance to the solvent of the electro-optic polymer solution. The MZI structure is molded as described above. The width and thickness of the molded waveguide core is $4.5 \mu\text{m}$ and $2.6 \mu\text{m}$, respectively. Due to the process of molding with a soft stamp, a thin residue of electro-optic polymer material is present; however, this residue can be controlled and maintained at a tolerable level [19]. The structure is baked at $100 \text{ }^\circ\text{C}$ for two hours to remove any remaining solvent. Another $3.2 \mu\text{m}$ thick WR-513 film is spun on as the upper cladding. Finally, 100 nm of Au is evaporated over one arm of the MZI, serving as the upper electrode.

The randomly oriented chromophores dispersed in the APC matrix must be aligned to result in a collective electro-optic effect. By heating the polymer film above its glassy temperature ($T_g \simeq 145 \text{ }^\circ\text{C}$ for AJL8/APC) while applying a strong electric field, the dipolar chromophores are aligned. We employ the corona poling method [109] with a needle-to-sample separation of 2 cm . The needle tip is biased

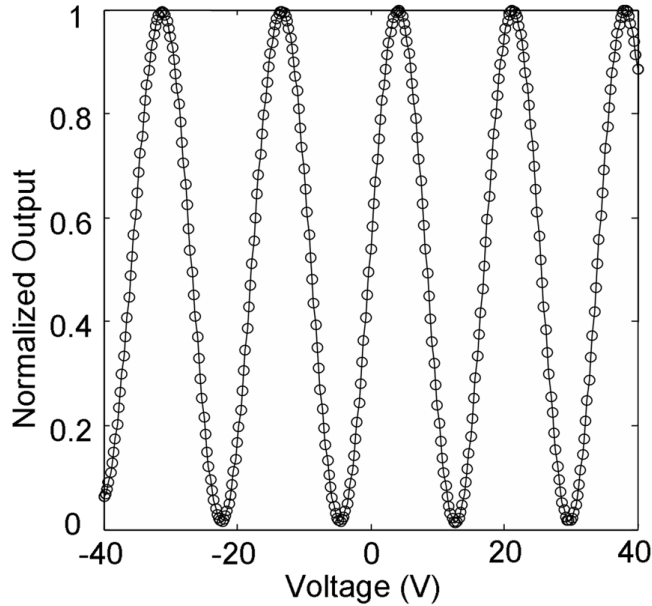


Figure 6.9: Measured modulator output as a function of applied voltage. An applied voltage of $V_{\pi}=8.4$ V renders the input 1600 nm light null.

to approximately 5.6 kV. As the sample is heated to 145 °C, the corona current is monitored by measuring the voltage drop across a 10 M Ω resistor and is limited to 2 μ A in an ambient air environment. The sample is poled for approximately 45 minutes, and then cooled while keeping the voltage applied. At \sim 40 °C, the voltage is turned off and the sample is removed.

To prepare for measurement, the substrate is cleaved and the waveguide end-facets are left unpolished. Laser light at 1600 nm wavelength is fed through a polarizer and input into the MZI through a tapered fiber. The output signal is collected using another fiber and is measured using a photodetector. The voltage is applied to the MZI using either a voltage source or a function generator. The entire setup is controlled by GPIB.

6.4.2 Results and Discussion

The measurement results are shown in Figure 6.9. Voltages ranging from -40 V to +40 V are sequentially applied in 0.25 V increments while monitoring the photodetector output signal. The measurement was also confirmed using a 1-kHz triangle wave and an oscilloscope. With no applied voltage, the output is approximately half its maximum, indicating that the two arms of the interferometer are of slightly different length. The half-wave voltage V_π , defined as the voltage required to switch the output from full-on to full-off, is found to be 8.4 V. This value is within a factor of two of the value that commercial devices exhibit. Several means can be employed to further reduce this value. First, thinning of the cladding layers would proportionally reduce V_π . Second, the voltage was applied to only one arm of the MZI – not to both arms in a “push-pull” fashion – which would result in a factor of two reduction in V_π . Finally, optimization of the poling efficiency is necessary to further reduce V_π . The total insertion loss was not measured since the waveguide end-facets were left unpolished and were not mode-matched to the input/output fibers.

While the halfwave voltage is indicative of the polymer nonlinearity and the electrode configuration, the on/off extinction ratio of the modulator signifies the quality and precision of the fabrication. In the MZI structure, light interferes after having traveled different optical path lengths and the degree of destructive interference depends on the quality of both the Y-junction splitter and combiner, and on any differential loss in the arms of the MZI. The extinction ratios of the nulls in the output shown in Figure 6.9 are better than 19 dB, similar to recent reports using traditional electro-optic polymer fabrication techniques [68]. The deep extinction of the nulls for the replica molded MZI suggests that the Y-junctions are of precise 3-dB splitting ratio and that there is very little differential loss in the interferometer arms. This demonstrates the accuracy of the replication process enabling high-resolution features of the Y-branch junction to be reproduced in the replica. The achieved low differential loss indicates that the replica molding process produces a low number of waveguide defects and good waveguide uniformity

over many square centimeters.

In summary, a Mach-Zehnder electro-optic polymer modulator was fabricated by soft-stamp replica molding. The core polymer incorporated state-of-the-art nonlinear optical chromophores that are highly nonlinear and show good thermal- and photo-stability. The resultant device was measured with 1600 nm incident light to have a halfwave voltage of 8.4 V and an extinction ratio better than 19 dB. These results establish that the replica molding process has the potential to meet the demanding requirements of high-resolution necessary for inexpensive mass production of electro-optic polymer modulators.

Chapter 7

Conclusions

7.1 Synopsis

In this thesis, the properties of polymers as differentiated from more traditional integrated optics materials have been described, and the manipulation of these properties have led to developments that could not be achieved as quickly, as easily, or at all in semiconductor or other inorganic materials. In what follows, a brief synopsis of the highlights of this thesis are given.

Because of the low material dispersion inherent to polymer optical materials, there was an interest in developing waveguide couplers that operate over wide wavelength ranges. Presented in Chapter 2 was a novel analysis tool based on the three-dimensional geometrical representation of the 2-by-2 coupled mode theory. The analysis of directional, adiabatic, and non-adiabatic mode evolution couplers evinced the utility of the geometrical representation. Further, the geometrical representation was applied as a design tool, allowing for the design of wide bandwidth non-adiabatic mode evolution couplers. These are couplers that exhibit performance similar to adiabatic couplers, but are of much smaller and more reasonable physical extent. The theoretical expectations from the geometrical representation were tested using beam propagation method simulations and excellent results were observed. The resultant design exhibited a flat 3-dB splitting ratio over operating wavelengths from 1300 nm to 1600 nm and little deviation in splitting ratio when

the waveguide widths were scaled from 0.8 to 1.2 times their intended widths. This type of wavelength-invariant and fabrication-error tolerant construction is of great utility for couplers in integrated optical circuits to be effectively used over a wide range of communications wavelengths.

Recent advances in fabrication methods for integrated optical devices have allowed the manufacture of devices that require extremely high precision. Passive polymer microring resonators were presented as examples of devices requiring high precision, whose fabrication has only become possible in recent years using, for example, electron beam lithography. Microring resonators are important as add/drop filters, modulators, switches, chemical or biological sensors, dispersion compensators and lasers. In Chapter 3, the general theory of microring resonators was examined, fleshing out the useful attributes and design rules. Using the high precision of electron beam lithography and the rapid prototyping ability of direct write polymer resists, polymer microring resonators were fabricated in SU-8 epoxy and optically characterized. The unique features of polymers allowed the fabrication of thin, flexible, all-polymer freestanding films containing many microring resonator optical filters. The measurements of these devices proved that freestanding devices performed comparably to similar devices with rigid crystalline substrates. This type of flexible all-polymer film may find use by adhesion of films of microoptical devices to non-flat surfaces, or to different functional structures such as electronic drive circuitry. Further, these films can be rolled up or folded for storage and unrolled for future deployment. The rapid prototyping ability of SU-8 was also applied to the fabrication of novel microring resonator-based inline reflectors. These devices are a unique alternative to inline reflectors such as dielectric mirrors or Bragg-grating reflectors.

Several of the individual microring resonators can be chained together to form a new class of waveguide termed the coupled resonator optical waveguide (CROW) – the subject of Chapter 4. The interest in these devices is primarily due to the means propagation; a portion of the photons in each microring essentially hops from one resonator to the adjacent resonator, and thus, an overall transmission

of the light down the chain is achieved. Comparing to a conventional waveguide of the same physical length, this can lead to a slower propagation through the CROW waveguide, with the group velocity determined by the coupling coefficient between the individual rings, enabling use as optical delay lines or pulse storage units. By virtue of the tailorable wavelength response, CROWs are also of interest as dispersion compensators and high-order optical filters. The two theoretical frameworks used to describe and design CROWs – the tight-binding method and the matrix method – were presented. To demonstrate the ability to fabricate and effectively characterize CROW devices in polymer, a CROW-Mach-Zehnder interferometer was demonstrated in SU-8 polymer. Using the matrix analysis method, very good agreement was observed between the measured interferometric response and the prediction of the matrix method. This agreement is particularly impressive because in the fitting, a single value of the coupling and a single value of the ring radius were assumed, thus demonstrating the extremely high precision of the direct electron beam fabrication. These results point toward the use of polymers for optical delay lines comprising many individual microrings, fabricated by direct electron beam patterning.

Although a variety of high performance polymer optical devices have been previously demonstrated by other research groups with impressive results, these devices almost universally were fabricated using traditional semiconductor fabrication technology. Addressed in Chapter 5 is the manipulation of the unique properties of optical polymer materials to enable a new means of fabrication. The novel fabrication method is based on the use of a soft PDMS rubber mold to form polymer waveguide devices. High-fidelity replicas of the original master devices are achievable using this molding method. Polymer materials can be patterned by the molding method because, unlike semiconductor or most inorganic optical materials, polymers can be dissolved in solution that can be molded into the desired shape while being cured. Because of the low surface energy of PDMS, the master devices used to make the mold can be fabricated in virtually any material and by virtually any means. Many PDMS molds can be made from each master, and

each mold can be used many times to make the replicas. This economy of scales furthers the cost advantages of polymers for industrial applications. To demonstrate the ability of the method for high-fidelity replication, a microring resonator was replicated and the optical response of the replica was compared to that of the original master device, both being fabricated in SU-8. Excellent agreement of the optical responses demonstrated that the soft-stamp replica molding fabrication method is capable of device fabrication with precision necessary for high quality polymer integrated optical components. A drawback of the use of soft PDMS as the mold material is the ubiquitous presence of a background residue of thin polymer material. It was shown that the thickness of the residue can be reduced to acceptable levels (as determined by numerical simulations) by careful choice of the solution concentration. Further, the residue was thinnest near the waveguides, thereby minimizing the deleterious effects of its presence. Finally, the replica molding technique can be sequentially repeated to form multilayer, three-dimensional integrated optical devices with each layer being separated by a polymer cladding layer. A multilayer device with two microring resonators on separate layers was fabricated and characterized to demonstrate this function of the replica molding technique.

Among the most promising applications of polymers for telecommunications-industry applications are electro-optic polymer modulators exhibiting exceptionally high operating bandwidth and low switching voltages. Demonstrated in Chapter 6 is the effort to further prove the utility of the replica molding technique for industry-grade optical devices by applying the method to the construction of electro-optic polymer modulators. Polymers are generally not natively electro-optic, so passive polymers are doped with chromophore molecules chemically engineered to exhibit extremely high nonlinearities. These dopant molecules must be aligned by high-voltage poling of the polymer films, resulting in a collective electro-optic effect. For a first proof-of-concept experiment, a short Mach-Zehnder modulator was fabricated by replication of a master device patterned by electron beam lithography. The properties of this device predicted good performance for a

full size Mach-Zehnder. To this end, a full size Mach-Zehnder modulator was fabricated by a modified replica molding technique, allowing molding over large areas of several square centimeters. Employing newly developed AJL8 chromophores, the resulting modulator exhibited a switching voltage of 8.4 V at 1600 nm with single arm modulation. Dual arm modulation in the push-pull format would result in a switching voltage of approximately 4 V, and further improvement of the poling would result in even lower values. The extinction ratio of the modulator was measured to be better than 19 dB, demonstrating high quality fabrication of the Y-junctions and low differential loss in the arms of the modulator. Together with the low switching voltages, these results prove the usefulness of the replica molding technique for the manufacture of high performance polymer modulators, with cost and time savings for both set up and fabrication.

7.2 Outlook

Polymer materials will be deployed in industrial telecommunications applications in the near future. There are simply too many useful attributes of the material for it not to be implemented. For instance, the low material costs compared to semiconductor or other crystalline materials make polymers especially attractive for industrial applications. The versatility and simplicity of the fabrication methods are an enticing attribute, further reducing manufacturing costs and enabling device architectures not possible with crystalline materials. Further, polymers can be doped with various functional molecules to exhibit, for instance, gain or the electro-optic effect. The electro-optic dopants can be designed and synthesized to have extremely high nonlinearities, much larger than those of crystalline materials such as lithium niobate.

Despite the attractive properties of polymer materials, there exists skepticism among photonic engineers due to the difficulties not overcome in the nearly two decades of research on optical polymers. Among the predominant concerns are the relatively high material loss, the temperature dependence of the refractive

index, and the long term stability of both the passive and doped materials. These limitations have prevented most polymer-based devices from passing Telcordia standards tests, a necessity for the serious consideration of polymers for various industrial applications.

The issue of loss in polymers has recently been of particular research interest resulting in several lower loss commercial materials. Since the loss in polymer waveguides is due to the absorption of molecular resonances, lower loss is achieved by substituting hydrogen atoms with fluorine atoms and hence, moving the absorption resonances outside the communications bands. This can result in polymer films with material losses on the order of 0.1 dB/cm. Addressing waveguide sidewall scattering loss, the plastic nature of polymers allows for post fabrication smoothing of defects by heating the materials to near the glass transition temperature. Finally, the refractive index of optical polymers is similar to that of silica, providing for potentially lower transition loss between the polymer waveguide device and the pigtailed fiber.

While it is true and unavoidable that polymers do not stand up well to very high temperatures, many are materially stable at sustained temperatures of 85 °C and humidity of 85 %. This stability includes electro-optic guest-host polymers that have been shown to retain approximately 80 % of the original nonlinearity after 500 hours at 85 °C. Clever engineering and future material advances can further reduce degradation with temperature. For instance, crosslinkable polymers incorporating electro-optic chromophores promise much better long term and environmental stability. In addition, hermetic packaging of polymer devices results in greatly improved long term stability. As for the temperature sensitivity of the refractive index, simple trimming circuits can be added to alleviate any response changes from the variation in refractive index.

The foremost issues preventing deployment of polymers in industrial settings are based primarily on longstanding and fundamental material shortcomings. There is clearly a need for the chemistry and materials community to design and synthesize new and better materials to address these issues. This rapid advance appears

to have begun in earnest, with new low-loss materials and more stable electro-optic polymers demonstrating improved performance and becoming more readily available with each year. In addition to the properties that make polymer materials advantageous in replacing semiconductor or other crystalline materials, there is a need to consider applications that are not possible with other materials. On this level, there is a need for close collaboration between the chemists and optical engineers. An application that necessitates polymer materials and is impossible with traditional optical materials may serve as a further catalyst towards future research on newer, better performing, and more stable materials with unique features.

Appendix A

Beam Propagation Method

The beam propagation method (BPM) is an especially valuable design and analysis tool for integrated optics. It is simple to understand and execute. As the name suggests, BPM simulates the propagation of an initial beam through some refractive index profile, prescribed in both cross-section and propagation direction. The method is especially useful for designing optical couplers and waveguide tapers. In what follows, the original formulation of Feit and Fleck [113] is followed closely. In brief, the initial electro-magnetic field is propagated through the waveguide structure approximated by consecutive discretized sections of free space propagation and lensing. The power can be plotted at each cross-section, giving a pictorial representation of the power flow in the device.

A.1 Conceptual Underpinnings

Light within a waveguide is described by the transverse electric field $E(\omega, x, y, z)$ that is a solution to the scalar Helmholtz equation

$$\left(\frac{\partial^2}{\partial x^2} + \frac{\partial^2}{\partial y^2} + \frac{\partial^2}{\partial z^2} + \frac{\omega^2}{c^2} n^2(\omega, x, y) \right) E(\omega, x, y, z) = 0 \quad (\text{A.1})$$

where ω is the radian frequency of the light, and the refractive index $n(\omega, x, y)$ is assumed to be independent of z .

At $z = \Delta z$, (A.1) can be written in terms of the electric field at $z = 0$ using

$$E(x, y, \Delta z) = \exp\left(\pm i\Delta z \left(\nabla_{\perp}^2 + \frac{\omega^2}{c^2}n^2\right)^{\frac{1}{2}}\right) E(x, y, 0) \quad (\text{A.2})$$

where $\nabla_{\perp}^2 = \frac{\partial^2}{\partial x^2} + \frac{\partial^2}{\partial y^2}$. The argument of the exponential in (A.2) is rewritten as

$$\left(\nabla_{\perp}^2 + \frac{\omega^2}{c^2}n^2\right)^{\frac{1}{2}} = \frac{\nabla_{\perp}^2}{\left(\nabla_{\perp}^2 + \frac{\omega^2}{c^2}n^2\right)^{\frac{1}{2}} + \frac{\omega}{c}n} + \frac{\omega}{c}n \quad (\text{A.3})$$

The refractive index n in the first term on the right-hand-side of (A.3) is replaced by a reference value, n_0 , typically taken to be the refractive index of the waveguide cladding. This approximation is valid for small variations in $n(x, y)$ and thus the BPM method must be used with care for high-index contrast waveguide systems. (A.3) then becomes

$$\left(\nabla_{\perp}^2 + \frac{\omega^2}{c^2}n^2\right)^{\frac{1}{2}} \cong \frac{\nabla_{\perp}^2}{\left(\nabla_{\perp}^2 + k^2\right)^{\frac{1}{2}} + k} + k + k \left[\frac{n}{n_0} - 1\right] \quad (\text{A.4})$$

where $k = \frac{\omega}{c}n_0$.

The time dependence of the solution appears in the field as $E(\omega, x, y, z) = E(x, y, z) \exp(i\omega t)$ and is assumed in what follows. The solution is taken to be that of a single wave propagating in the $+z$ direction, of the form $E(x, y, z) = \varepsilon(x, y, z) \exp(-ikz)$. Inserting this solution into (A.2), taking the negative sign and using (A.4), yields

$$\varepsilon(x, y, \Delta z) = \exp\left[-i\Delta z \left(\frac{\nabla_{\perp}^2}{\left(\nabla_{\perp}^2 + k^2\right)^{\frac{1}{2}} + k} + \chi(x, y)\right)\right] \varepsilon(x, y, 0) \quad (\text{A.5})$$

where $\chi(x, y) = k \left(\frac{n}{n_0} - 1\right)$.

We rewrite (A.5) in the split-symmetrized form

$$\begin{aligned} \varepsilon(x, y, \Delta z) = & \exp \left[-\frac{i\Delta z}{2} \left(\frac{\nabla_{\perp}^2}{(\nabla_{\perp}^2 + k^2)^{\frac{1}{2}} + k} \right) \right] \exp(-i\Delta z \chi(x, y)) \\ & \times \exp \left[-\frac{i\Delta z}{2} \left(\frac{\nabla_{\perp}^2}{(\nabla_{\perp}^2 + k^2)^{\frac{1}{2}} + k} \right) \right] \varepsilon(x, y, 0) \\ & + O(\Delta z)^3 \end{aligned} \quad (\text{A.6})$$

where the error $O(\Delta z)^3$ is due to the noncommutation of ∇_{\perp}^2 and $\chi(x, y)$.

To glean more physical insight into the meaning of (A.6), we view the operators in the following way. The term

$$\exp \left[-i\Delta z \left(\frac{\nabla_{\perp}^2}{(\nabla_{\perp}^2 + k^2)^{\frac{1}{2}} + k} \right) \right] \varepsilon(x, y, 0) \quad (\text{A.7})$$

represents a solution to the Helmholtz equation, with the initial condition $E(x, y, 0)$, in a homogeneous medium with refractive index n_0 . The operator

$$\exp(-i\Delta z \chi(x, y)) \quad (\text{A.8})$$

corresponds to transmission of a field $\varepsilon(x, y, 0)$ through a lens, imposing a phase $\phi(x, y) = \Delta z \chi(x, y)$. This term incorporates the information about the waveguide cross-section. Thus the field is built up by successive operations. The initial field is transported through a homogeneous medium for a distance $\frac{\Delta z}{2}$, then the field incurs the phase of a lens, then it propagates in homogeneous space a distance $\frac{\Delta z}{2}$ until the next lens, and the procedure repeats for as many partitions as is programmed.

A.2 Practical Application

The first step in the practical application of BPM is to decompose $\varepsilon(x, y, z)$ into its Fourier series

$$\varepsilon(x, y, z) = \sum_{m=-M/2+1}^{M/2} \sum_{n=-N/2+1}^{N/2} \varepsilon_{mn}(z) \exp\left(\frac{2\pi imx}{L_x} + \frac{2\pi imy}{L_y}\right) \quad (\text{A.9})$$

where L_x and L_y are the computational grid lengths in the x and y directions. The propagation of light through a homogeneous medium, with refractive index n_0 , over a distance Δz , can be calculated from the Fourier coefficients of the initial field by

$$\varepsilon_{mn}(\Delta z) = \exp\left[i\Delta z \left(\frac{k_x^2 + k_y^2}{\sqrt{-k_x^2 - k_y^2 + k^2 + k}}\right)\right] \quad (\text{A.10})$$

where k_x and k_y are the transverse wavenumbers given by $k_x = (2\pi m)/L_x$ and $k_y = (2\pi n)/L_y$, and as before $k = (2\pi/\lambda)n_0$. The lensing step that follows the propagation step is

$$\varepsilon(x, y)' = \exp(-i\Delta z\chi)\varepsilon(x, y, \Delta z) \quad (\text{A.11})$$

The fast Fourier transform (FFT) algorithm is a useful macro in many programming environments enabling fast and easy development of the BPM algorithm. One must begin with an initial field, which could be an approximate guess of the waveguide mode or of the excitation. The FFT of this field is multiplied by the homogeneous space propagation operator, as in (A.10). The resulting field is then inverse Fourier transformed (IFFT), and multiplied by the lensing operator as in (A.11). The preceding two steps are then repeated in a loop for each step Δz , until the extent of the computational grid is reached. The saved fields can then be displayed at any cross-section of the computational grid.

Due to aliasing problems commonly associated with the FFT procedure, one must include some sort of boundary conditions. By far the most simple is to employ slightly absorbing zones near the transverse edges of the computational field. This is done by adding a small (ca. 1%) imaginary component to the refractive index

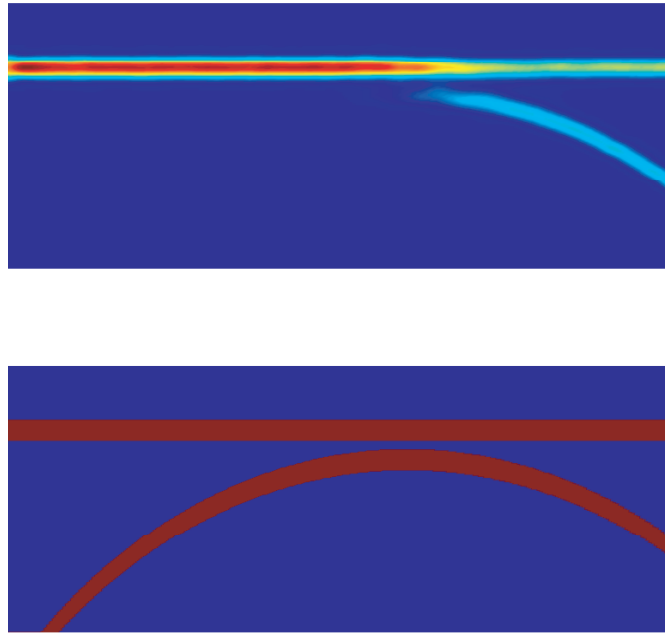


Figure A.1: 3-dimensional BPM simulation of a straight waveguide side-coupled to a microring resonator.

in the selected regions.

As an example, shown in Figure A.1 is a 3-dimensional BPM simulation of a straight waveguide side-coupled to a microring resonator with a $100\ \mu\text{m}$ radius. The calculation window is $125\ \mu\text{m}$ long, $20\ \mu\text{m}$ wide, and $7.5\ \mu\text{m}$ thick. The waveguides are $1.5\ \mu\text{m}$ square, with core refractive index 1.6 and cladding refractive index 1.5. The gap between the waveguide and the ring is $650\ \text{nm}$. Light, at $1550\ \text{nm}$, is input to the straight waveguide on the left side of the calculation window. The field propagates as a waveguide mode until reaching the coupling region, at which point a portion of the field couples into the resonator. The coupling ratio of a given structure can be estimated in this manner.

Appendix B

Finite Difference Mode Solver

For optical elements such as the ring resonators described in earlier chapters, it is important to carefully design the structures such that only a single mode is guided within the waveguide core. The semivectorial finite-difference method developed by Stern [114] enables the calculation of the mode for a given waveguide cross-section. This method is clearly outlined in Reference [115]. In brief, the electro-magnetic equations describing the mode of a waveguide are solved by discretizing the cross-section. The resulting solutions to an eigenvalue equation yield the modes corresponding to the propagation constant eigenvalues. For eigenvectors with propagation constants larger than the propagation constant for the bulk cladding, the modes are guided. This can be confirmed graphically by plotting the mode profiles.

B.1 Conceptual Underpinnings

As with any finite difference algorithm, the key to the method is the approximation that derivatives of a function can be replaced, for example, by a difference quotient

$$\frac{df(x_0)}{dx} = \frac{f(x_0 - h) - f(x_0 + h)}{2h}. \quad (\text{B.1})$$

Employing the difference quotients, the equations that we are to solve are the

semivectorial wave equations. Beginning with the vectorial wave equation

$$\nabla^2 \mathbf{E} + \nabla \left(\frac{\nabla \epsilon(\mathbf{r})}{\hat{\mathbf{r}}} \cdot \mathbf{E} \right) + k_0^2 \epsilon(\mathbf{r}) \mathbf{E} = 0 \quad (\text{B.2})$$

we first make the identification that $\frac{d\epsilon(\mathbf{r})}{dz} = 0$, since we are solving for a waveguide cross-section in the x - y plane. Rewriting the terms of (B.2) and substituting $\frac{\partial}{\partial z} = -i\beta$, the vectorial wave equations become

$$\frac{\partial^2 E_x}{\partial x^2} + \frac{\partial}{\partial x} \left(\frac{1}{\epsilon(\mathbf{r})} \frac{\partial \epsilon(\mathbf{r})}{\partial x} E_x \right) + \frac{\partial^2 E_x}{\partial y^2} + \left(k_0^2 \epsilon(\mathbf{r}) - \beta^2 \right) E_x + \frac{\partial}{\partial x} \left(\frac{1}{\epsilon(\mathbf{r})} \frac{\partial \epsilon(\mathbf{r})}{\partial y} E_y \right) = 0 \quad (\text{B.3})$$

for the x component, and

$$\frac{\partial^2 E_y}{\partial x^2} + \frac{\partial}{\partial y} \left(\frac{1}{\epsilon(\mathbf{r})} \frac{\partial \epsilon(\mathbf{r})}{\partial y} E_y \right) + \frac{\partial^2 E_y}{\partial y^2} + \left(k_0^2 \epsilon(\mathbf{r}) - \beta^2 \right) E_y + \frac{\partial}{\partial y} \left(\frac{1}{\epsilon(\mathbf{r})} \frac{\partial \epsilon(\mathbf{r})}{\partial x} E_x \right) = 0 \quad (\text{B.4})$$

for the y component.

To attain the semivectorial wave equations from the above, the terms representing the interactions between the x components and the y components are considered to be small in comparison with the other terms in (B.3) and (B.4). Therefore the terms

$$\frac{\partial}{\partial x} \left(\frac{1}{\epsilon(\mathbf{r})} \frac{\partial \epsilon(\mathbf{r})}{\partial y} E_y \right) \quad \text{and} \quad \frac{\partial}{\partial y} \left(\frac{1}{\epsilon(\mathbf{r})} \frac{\partial \epsilon(\mathbf{r})}{\partial x} E_x \right) \quad (\text{B.5})$$

are set to zero. The problem is now reduced to solving for a quasi-TE mode involving E_x or a quasi-TM mode for E_y .

B.2 Practical Application

We consider only the quasi-TE mode since we can solve for the quasi-TM mode by simply rotating space by 90 degrees. The basic semivectorial wave equation to

be discretized is

$$\frac{\partial^2 E_x}{\partial x^2} + \frac{\partial}{\partial x} \left(\frac{1}{\epsilon(\mathbf{r})} \frac{\partial \epsilon(\mathbf{r})}{\partial x} E_x \right) + \frac{\partial^2 E_x}{\partial y^2} + \left(k_0^2 \epsilon(\mathbf{r}) - \beta^2 \right) E_x = 0 \quad (\text{B.6})$$

Evaluation of the terms in (B.6) in terms of discretized quantities is achieved by formulating Taylor series expansions around nodes (x, y) of the field and dielectric constant. This process, found in Reference [115], is rather lengthy and its presentation here would be superfluous.

On a grid where the indices p and q give the node, the necessary identities are

$$E_{p,q} = E(x_p, y_q) \quad (\text{B.7})$$

$$\begin{aligned} n &= y_q - y_{q-1} & e &= x_{p+1} - x_p \\ s &= y_q + 1 - y_q & w &= x_p - x_{p-1} \end{aligned} \quad (\text{B.8})$$

The various n , s , e , and w are the nodal spacings. The finite difference representation of (B.6) is

$$\alpha_w E_{p-1,q} + \alpha_e E_{p+1,q} + \alpha_n E_{p,q-1} + \alpha_s E_{p,q+1} + (\alpha_x + \alpha_y) E_{p,q} + \left[k_0^2 \epsilon(p, q) - \beta^2 \right] E_{p,q} = 0 \quad (\text{B.9})$$

where

$$\begin{aligned} \alpha_w &= \frac{2}{w(e+w)} \frac{2\epsilon(p-1,q)}{\epsilon(p,q) + \epsilon(p-1,q)} \\ \alpha_e &= \frac{2}{e(e+w)} \frac{2\epsilon(p+1,q)}{\epsilon(p,q) + \epsilon(p+1,q)} \\ \alpha_n &= \frac{2}{n(n+s)} \\ \alpha_s &= \frac{2}{s(n+s)} \\ \alpha_x &= -\frac{4}{ew} + \alpha_e + \alpha_w \\ \alpha_y &= -\frac{2}{ns} \end{aligned} \quad (\text{B.10})$$

For programming, (B.9) is recast as an eigenvalue equation in the form

$$[A]\{\phi\} = \beta^2 \{\phi\} \quad (\text{B.11})$$

where β^2 is an eigenvalue, $\{\phi\}$ is the eigenvector represented by

$$\{\phi\} = \begin{pmatrix} \phi_1 & \phi_2 & \phi_3 & \dots & \phi_M \end{pmatrix} \quad (\text{B.12})$$

and $[A]$ is the matrix populated by the various coefficients in (B.9). The number of eigenvectors is $M = M_x \times M_y$ and $[A]$ is a $M \times M$ matrix.

Since the calculation grid is not infinite, some sort of artificial boundary conditions need to be applied. There are three types of boundary conditions applied to finite difference calculations. The first and simplest is the Dirichlet boundary condition, represented by

$$\phi_{outside} = 0 \quad (\text{B.13})$$

for nodes outside the calculation window. This forces the field to be zero at the edges of the analysis grid. The Neumann boundary condition requires that the field just outside the calculation window is equal to the field just inside the window. This is represented by

$$\phi_{outside} = \phi_{boundary} \quad (\text{B.14})$$

The third boundary condition is the analytical boundary condition, for which it is assumed that the field exponentially decays outside the calculation window according to

$$\phi_{outside} = \left(e^{-k_0 \sqrt{|n_{eff}^2 - \epsilon(p,q)|} \Delta} \right) \phi_{boundary} \quad (\text{B.15})$$

where Δ is the discretization width at the boundary.

As programmed in Matlab, the eigenvalues and eigenvectors of $[A]$ can be calculated with the function *eigs*. Several of the largest eigenvalues are found, giving the several largest effective mode indices. If these effective indices are larger than the refractive index of the bulk cladding material, the mode is guided. The corresponding eigenvectors are plotted, giving a pictorial representation of the first few mode profiles.

An example result is shown in Figure B.1. The waveguide dimensions are $2 \mu\text{m}$ wide, $2 \mu\text{m}$ thick at the waveguide core, and with a $1 \mu\text{m}$ core material background

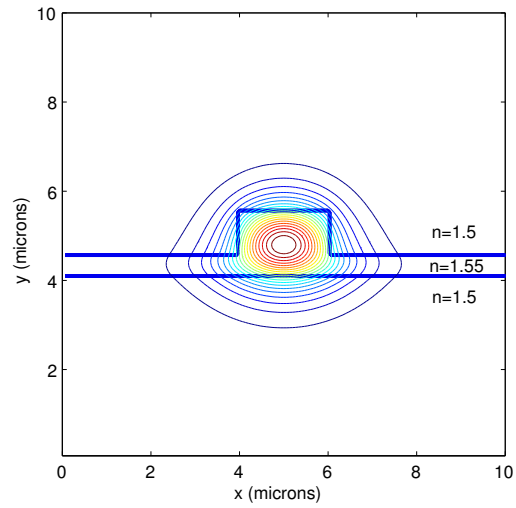


Figure B.1: Outline of waveguide cross-section, with power contours of the first order mode as calculated for a quasi-TE mode using the semivectorial finite difference method.

elsewhere. The first-order mode of a rib waveguide is displayed as a contour plot of the power in the waveguide cross-section. The core refractive index is 1.55 and the cladding 1.5. The effective index of this first order mode is 1.515 and no other modes are guided.

Appendix C

List of Publications

1. G. T. Paloczi, J. Scheuer, and A. Yariv, "Compact microring-based wavelength-selective inline optical reflector," *IEEE Photonics Technology Letters*, 17 (2): 390-392, 2005.
2. J. Scheuer, G. T. Paloczi, J. K. S. Poon, and A. Yariv, "Coupled Resonator Optical Waveguides: Towards Slowing and Storing of Light," *Optics and Photonics News*, 36-40, 2005.
3. J. K. S. Poon, Y. Y. Huang, G. T. Paloczi, A. Yariv, C. Zhang, and L. R. Dalton, "Wide-range tuning of polymer microring resonators by photobleaching CLD-1 chromophores," *Optics Letters*, 29 (22):2584-2586, 2004.
4. Y. Y. Huang, G. T. Paloczi, J. K. S. Poon, and A. Yariv, "Bottom-up soft-lithographic fabrication of three-dimensional multilayer polymer integrated optical microdevices," *Applied Physics Letters*, 85 (15): 3005-3007, 2004.
5. J. K. S. Poon, Y. Y. Huang, G. T. Paloczi, and A. Yariv, "Soft lithography replica molding of critically coupled polymer microring resonators," *IEEE Photonics Technology Letters*, 16 (11): 2496-2498, 2004.
6. G. T. Paloczi, Y. Y. Huang, A. Yariv, J. D. Luo, and A. K.-Y. Jen, "Replica molded electro-optic polymer Mach-Zehnder modulator," *Applied Physics Letters*, 85 (10): 1662-1665, 2004.

7. G. T. Paloczi, Y. Y. Huang, J. Scheuer, and A. Yariv, "Soft lithography molding of polymer integrated optical devices: reduction of background residue," *Journal of Vacuum Science and Technology B*, 22 (4): 1764-1769, 2004.
8. Y. Y. Huang, G. T. Paloczi, A. Yariv, C. Zhang, and L. R. Dalton, "Fabrication and replication of polymer integrated optical devices using electron-beam lithography and soft lithography," *Journal of Physical Chemistry B*, 108 (25): 8606-8613, 2004.
9. G. T. Paloczi, A. Eyal, and A. Yariv, "Wavelength-insensitive nonadiabatic mode evolution couplers," *IEEE Photonics Technology Letters*, 16 (2): 515-517, 2004.
10. J. K. S. Poon, J. Scheuer, S. Mookherjea, G. T. Paloczi, Y. Y. Huang, and A. Yariv, "Matrix analysis of microring coupled-resonator optical waveguides," *Optics Express*, 12 (1): 90-103, 2004.
11. Y. Y. Huang, G. T. Paloczi, J. K. S. Poon, A. Yariv, "Demonstration of flexible freestanding all-polymer integrated optical ring resonator devices," *Advanced Materials*, 16 (1): 44-, 2004.
12. G. T. Paloczi, Y. Y. Huang, and A. Yariv, "Free-standing all-polymer microring resonator optical filter," *Electronics Letters*, 39 (23): 1650-1651, 2003.
13. G. T. Paloczi, Y. Y. Huang, A. Yariv, and S. Mookherjea, "Polymeric Mach-Zehnder interferometer using serially coupled microring resonators," *Optics Express*, 11 (21): 2666-2671, 2003.
14. Y. Y. Huang, G. T. Paloczi, J. Scheuer, and A. Yariv, "Soft lithography replication of polymeric microring optical resonators," *Optics Express*, 11 (20): 2452-2458, 2003.

Bibliography

- [1] A. Yariv, **Optical Electronics in Modern Communications**. New York: Oxford University Press, 1997.
- [2] L. Eldada, "Optical communication components," *Review of Scientific Instruments*, 75 (3): 575-593, 2004.
- [3] R. G. Hunsperger, **Integrated Optics, Theory and Technology**. New York: Springer, 2002.
- [4] L. Eldada, and L. W. Shacklette, "Advances in polymer integrated optics," *IEEE Journal of Selected Topics in Quantum Electronics*, 6 (1): 54-68, 2000.
- [5] J. A. Rogers, Z. Bao, K. Baldwin, A. Dodabalapur, B. Crone, V. R. Raju, V. Kuck, H. Katz, K. Amundson, J. Ewing, and P. Drzaic, "Paper-like electronic displays: Large-area rubber-stamped plastic sheets of electronics and microencapsulated electrophoretic inks," *Proceedings of the National Academy of Sciences*, 98 (9): 4835-4840, 2001.
- [6] R. H. Friend, R. W. Gymer, A. B. Holmes, J. H. Burroughes, R. N. Marks, C. Taliani, D. D. C. Bradley, D. A. Dos Santos, J. L. Bredas, M. Logdlund, and W. R. Salaneck, "Electroluminescence in conjugated polymers," *Nature* 397 (6715): 121-128, 1999.
- [7] L. Eldada, R. Blomquist, L. W. Shacklette, and M. J. McFarland, "High-performance polymeric componentry for telecom and datacom applications," *Optical Engineering*, 39 (3): 596-609, 2000.

- [8] J. A. Rogers, M. Meier, and A. Dodabalapur, "Using printing and molding techniques to produce distributed feedback and Bragg reflector resonators for plastic lasers," *Applied Physics Letters*, 73 (13): 1766-1768, 1998.
- [9] L. H. Slooff, A. van Blaaderen, A. Polman, G. A. Hebbink, S. I. Klink, F. C. J. M. Van Veggel, D. N. Reinhoudt, and J. W. Hofstraat, "Rare-earth doped polymers for planar optical amplifiers," *Journal of Applied Physics*, 91 (7): 3955-3980, 2002.
- [10] L. R. Dalton, W. H. Steier, B. H. Robinson, C. Zhang, A. Ren, S. Garner, A. Chen, T. Londergan, L. Irwin, B. Carlson, L. Fifield, G. Phelan, C. Kincaid, J. Amend, and A. Jen, "From molecules to opto-chips: organic electro-optic materials," *Journal of Material Chemistry*, 9 (9): 1905-1920, 1999.
- [11] H.-C. Song, M.-C. Oh, S.-W. Ahn, W. H. Steier, H. R. Fetterman, C. Zhang, "Flexible low-voltage electro-optic polymer modulators," *Applied Physics Letters*, 82 (25): 4432-4434, 2003.
- [12] Y. Shi, C. Zhang, H. Zhang, J. H. Bechtel, L. R. Dalton, B. H. Robinson, and W. H. Steier, "Low (sub-1-volt) halfwave voltage polymeric electro-optic modulators achieved by controlling chromophore shape" *Science*, 288 (5463): 119-122, 2000.
- [13] M. Lee, H. E. Katz, C. Erben, D. M. Gill, P. Gopalan, J. D. Heber, and D. J. McGee, "Broadband modulation of light by using an electro-optic polymer," *Science*, 298 (5597): 1401-1403, 2002.
- [14] G. T. Paloczi, A. Eyal, and A. Yariv, "Wavelength-insensitive nonadiabatic mode evolution couplers," *IEEE Photonics Technology Letters*, 16 (2): 515-517, 2004.
- [15] G. T. Paloczi, Y. Huang, and A. Yariv, "Free-standing all-polymer microring resonator optical filter," *Electronics Letters*, 39 (23): 1650-1651, 2003.

- [16] Y. Y. Huang, G. T. Paloczi, J. K. S. Poon, A. Yariv, "Demonstration of flexible freestanding all-polymer integrated optical ring resonator devices," *Advanced Materials*, 16 (1): 44-, 2004.
- [17] G. T. Paloczi, J. Scheuer, and A. Yariv, "Compact microring-based wavelength-selective inline optical reflector," *IEEE Photonics Technology Letters*, 17 (2): 390-392, 2005.
- [18] G. T. Paloczi, Y. Y. Huang, A. Yariv, and S. Mookherjea, "Polymeric Mach-Zehnder interferometer using serially coupled microring resonators," *Optics Express*, 11 (21): 2666-2671, 2003.
- [19] G. T. Paloczi, Y. Y. Huang, J. Scheuer, and A. Yariv, "Soft lithography molding of polymer integrated optical devices: reduction of background residue", *Journal of Vacuum Science and Technology B*, 22 (4): 1764-1769, 2004.
- [20] Y. Huang, G. T. Paloczi, J. Scheuer, and A. Yariv, "Soft lithography replication of polymeric microring optical resonators," *Optics Express*, 11 (20): 2452-2458, 2003.
- [21] Y. Y. Huang, G. T. Paloczi, J. K. S. Poon, and A. Yariv, "Bottom-up soft-lithographic fabrication of three-dimensional multilayer polymer integrated optical microdevices," *Applied Physics Letters*, 85 (15): 3005-3007, 2004.
- [22] Y. Y. Huang, G. T. Paloczi, A. Yariv, C. Zhang, and L. R. Dalton, "Fabrication and replication of polymer integrated optical devices using electron-beam lithography and soft lithography," *Journal of Physical Chemistry B*, 108 (25): 8606-8613, 2004.
- [23] G. T. Paloczi, Y. Y. Huang, A. Yariv, J. D. Luo, and A. K.-Y. Jen, "Replica molded electro-optic polymer Mach-Zehnder modulator," *Applied Physics Letters*, 85 (10): 1662-1665, 2004.
- [24] J. D. Jackson, **Classical Electrodynamics**. New York: Wiley, 1999.

- [25] T. Tamir, Ed., **Guided-Wave Optoelectronics**. New York: Springer-Verlag, 1988.
- [26] W. P. Huang, "Coupled-mode theory for optical waveguides - an overview," *Journal of the Optical Society of America A*, 11 (3): 963-983, 1994.
- [27] R. P. Feynman, F. L. Vernon, Jr., and R. W. Hellwarth, "Geometrical representation of the Schrödinger wave equation for solving maser problems," *Journal of Applied Physics*, 28 (1): 49-52, 1957.
- [28] R. Ulrich, "Representation of codirectional coupled waves," *Optics Letters*, 1 (3): pp. 109-111, 1977.
- [29] N. J. Frigo, "A generalized geometrical representation of coupled mode theory," *IEEE Journal of Quantum Electronics*, 22 (11): 2131-2140, 1986.
- [30] S. K. Korotky, "Three-space representation of phase-mismatch switching in coupled two-state optical systems," *IEEE Journal of Quantum Electronics*, 22 (6): 952-958, 1986.
- [31] A. Syahriar, V. M. Schneider, and S. Al-Bader, "The design of mode evolution couplers," *Journal of Lightwave Technology*, 16 (10): 1907-1914, 1998.
- [32] W. K. Burns and A. F. Milton, "Waveguide Transitions and Junctions," in **Guided-wave optoelectronics**, T. Tamir, Ed. New York: Springer-Verlag, 1988.
- [33] Y. P. Li and C. H. Henry, "Silicon Optical Wavebench Technology," in **Optical Fiber Telecommunications IIIB**, I. P. Kaminow and T. L. Koch, Eds. San Diego: Academic Press, 1997.
- [34] J. P. Gordon, and H. Kogelnik, "PMD fundamentals: polarization mode dispersion in optical fibers," *Proceedings of the National Academy of Sciences*, 97 (9): 4541-4550, 2000.

- [35] Y. Shani, C. H. Henry, R. C. Kistler, R. F. Kazarinov, and K. J. Orlowsky, "Integrated optic adiabatic devices on silicon," *IEEE Journal of Quantum Electronics*, 27 (3): 556-566, 1991.
- [36] C. K. Madsen, and J. H. Zhao, **Optical Filter Design and Analysis**. New York: Wiley, 1999.
- [37] B. E. Little, and T. Murphy, "Design rules for maximally flat wavelength-insensitive optical power dividers using Mach-Zehnder structures," *IEEE Photonics Technology Letters*, 9 (12): 1607-1609, 1997.
- [38] R. R. A. Syms, "The digital directional coupler - improved design," *IEEE Photonics Technology Letters*, 4 (10): 1135-1138, 1992.
- [39] E. A. J. Marcatili, "Bends in dielectric optical waveguides," *Bell System Technical Journal*, 48 (7): 2103-, 1969.
- [40] R. Orta, P. Savi, R. Tascone, and D. Trincherro, "Synthesis of multiple-ring-resonator filters for optical systems," *IEEE Photonics Technology Letters*, 7 (12): 1447-1449, 1995.
- [41] B. E. Little, S. T. Chu, H. A. Haus, J. Foresi, and J.-P. Laine, "Microring resonator channel dropping filters," *IEEE Journal of Lightwave Technology*, 15 (6): 998-1005, 1997.
- [42] P. Rabiei, W. H. Steier, C. Zhang, and L. R. Dalton, "Polymer micro-ring filters and modulators," *IEEE Journal of Lightwave Technology*, 20 (11): 1968-1975, 2002.
- [43] T. A. Ibrahim, W. Cao, Y. Kim, J. La, J. Goldhar, P.-T. Ho, and C. H. Lee, "All-optical switching in a laterally coupled microring resonator by carrier injection," *IEEE Photonics Technology Letters*, 15 (1): 36-38, Jan. 2003.
- [44] G. Lenz, B. J. Eggleton, C. K. Madsen, and R. E. Slusher, "Optical delay lines based on optical filters," *IEEE Journal of Quantum Electronics*, 37 (4): 525-532, 2001.

- [45] S. L. McCall, A. F. J. Levi, R. E. Slusher, S. J. Pearton, and R. A. Logan, "Whispering gallery mode microdisk lasers," *Applied Physics Letters*, 60 (3): 289-291, 1992.
- [46] R. W. Boyd and J. E. Heebner, "Sensitive disk resonator photonic biosensor," *Applied Optics*, 40 (31): 5742-5747, 2001.
- [47] A. Yariv, "Universal relations for coupling of optical power between microresonators and dielectric waveguides," *Electronics Letters*, 36 (4): 321-322, 2000.
- [48] M. Born and E. Wolf, **Principles of Optics**. New York: Pergamon Press, 1970.
- [49] J. T. Verdeyen, **Laser Electronics**. New York: Prentice-Hall, 1981.
- [50] J. M. Choi, R. K. Lee, and A. Yariv, "Ring fiber resonators based on fused-fiber grating add-drop filters: application to resonator coupling," *Optics Letters*, 27 (18): 1598-1600, 2002.
- [51] D. Marcuse, **Light Transmission Optics**. New York: Van Nostrand Reinhold, 1972.
- [52] M. Heiblum and J. H. Harris, "Analysis of curved optical waveguides by conformal transformation," *IEEE Journal of Quantum Electronics*, 11 (2): 75-83, 1975.
- [53] D. Marcuse, "Bending losses of the asymmetric slab waveguide," *Bell Systems Technical Journal*, 50 (8): 2551-, 1971.
- [54] P. K. Tien, "Light waves in thin films and integrated optics," *Applied Optics*, 10 (11): 2395-2413, 1971.
- [55] R. J. Deri and E. Kapon, "Low-loss III-V semiconductor optical waveguides," *IEEE Journal of Quantum Electronics*, 27 (3): 626-640, 1991.

- [56] J. M. Shaw, J. D. Gelorme, N. C. LaBianca, W. E. Conley, and S. J. Holmes, "Negative photoresist for optical lithography," *IBM Journal of Research and Development*, 41 (1-2): 81-94, 1997.
- [57] W. H. Wong, and E. Y. B. Pun, "Exposure characteristics and three-dimensional profiling of SU8C resist using electron beam lithography," *Journal of Vacuum Science and Technology B*, 19 (3): 732-735, 2001.
- [58] M. Aktary, M. O. Jensen, K. L. Westra, M. J. Brett, and M. R. Freeman, "High-resolution pattern generation using the epoxy novolak SU-8 2000 resist by electron beam lithography," *Journal of Vacuum Science and Technology B*, 21 (4): L5-L7, 2003.
- [59] W. H. Wong, J. Zhou, and E. Y. B. Pun, "Low-loss polymeric optical waveguides using electron-beam direct writing," *Applied Physics Letters*, 78 (15): 2110-2112, 2001.
- [60] W. H. Wong, and E. Y. B. Pun, "Polymeric waveguide wavelength filters using electron-beam direct writing," *Applied Physics Letters*, 79 (22): 3576-3578, 2001.
- [61] M. Kuwata-Gonokami, R. H. Jordan, A. Dodabalapur, H. E. Katz, M. L. Schilling, R. E. Slusher, and S. Ozawa, "Polymer microdisk and microring lasers," *Optics Letters*, 20 (20): 2093-2095, 1995.
- [62] Y. Kawabe, Ch. Spiegelberg, A. Schulzgen, M. F. Nabor, B. Kippelen, E. A. Mash, P. M. Allemand, M. Kuwata-Gonokami, K. Takeda, and N. Peyghambarian, "Whispering-gallery-mode microring laser using a conjugated polymer," *Applied Physics Letters*, 72 (2): 141-143, 1998.
- [63] R. C. Polson, G. Levina, and Z. V. Vardeny, "Spectral analysis of polymer microring lasers," *Applied Physics Letters*, 76 (26): 3858-3860, 2000.
- [64] S. X. Dou, E. Toussaere, T. Ben-Messaoud, A. Potter, D. Josse, G. Kranzel-

- binder, and J. Zyss, "Polymer microring lasers with longitudinal optical pumping," *Applied Physics Letters*, 80 (2): 165-167, 2002.
- [65] H. Ma, A. K.-J. Jen, and L. R. Dalton, "Polymer-based optical waveguides: Materials, processing, and devices," *Advanced Materials*, 14 (19): 1339-1365, 2002.
- [66] S. R. Marder, B. Kippelen, A. K.-J. Jen, and N. Peyghambarian, "Design and synthesis of chromophores and polymers for electro-optic and photorefractive applications," *Nature* 388 (6645): 845-851, 1997.
- [67] R. Horvath, L. R. Lindvold, and N. B. Larsen, "Fabrication of all-polymer freestanding waveguides," *Journal of Micromechanics and Microengineering*, 13 (3): 419-424, 2003.
- [68] H.-C. Song, M.-C. Oh, S.-W. Ahn, W. H. Steier, H. Fetterman, and C. Zhang, "Flexible low-voltage electro-optic polymer modulators," *Applied Physics Letters*, 82 (25): 4432-4434, 2003.
- [69] B. E. Little, S. T. Chu, and H. A. Haus, "Second-order filtering and sensing with partially coupled traveling waves in a single resonator," *Optics Letters*, 23 (20): 1570-1572, 1998.
- [70] J. K. S. Poon, J. Scheuer, and A. Yariv, "Wavelength-selective reflector based on a circular array of coupled microring resonators," *IEEE Photonics Technology Letters*, 16 (5): 1331-1333, 2004.
- [71] A. Othonos, "Fiber Bragg gratings," *Review of Scientific Instruments*, 68 (12): 4309-4341, 1997.
- [72] M. H. Lim, T. E. Murphy, J. Ferrera, J. N. Damask, and H. I. Smith, "Fabrication techniques for grating-based optical devices," *Journal of Vacuum Science and Technology B*, 17 (6): 3208-3211, 1999.

- [73] Y. Yanagase, S. Suzuki, Y. Kokubun, and S. T. Chu, "Box-like filter response and expansion of FSR by vertically triple coupled microring resonator filter," *Journal of Lightwave Technology*, 20 (8): 1525-1529, 2002.
- [74] B. Liu, A. Shakouri and J. E. Bowers, "Passive microring-resonator-coupled lasers," *Applied Physics Letters*, 79 (22): 3561-3563, 2001.
- [75] K. Oda, N. Takato, and H. Toba, "A wide-FSR double-ring resonator for optical FDM transmission systems," *Journal of Lightwave Technology*, 9 (6): 728-736, 1991.
- [76] J. V. Hryniewicz, P. P. Absil, B. E. Little, R. A. Wilson, and P. -T. Ho, "Higher order filter response in coupled microring resonators," *IEEE Photonics Technology Letters*, 12 (3): 320-322, 2000.
- [77] A. Melloni, and M. Martinelli, "Synthesis of direct-coupled-resonators band-pass filters for WDM systems," *Journal of Lightwave Technology*, 20 (2): 296-303, 2002.
- [78] A. Yariv, Y. Xu, R. K. Lee, and A. Scherer, "Coupled resonator optical waveguide: a proposal and analysis," *Optics Letters*, 24 (11): 711-713, 1999.
- [79] Y. Xu, R. K. Lee, and A. Yariv, "Propagation and second harmonic generation of electromagnetic waves in a coupled-resonator optical waveguide," *Journal of the Optical Society of America B*, 17 (3): 387-400, 2000.
- [80] S. Mookherjea, and A. Yariv, "Kerr-stabilized super-resonant modes in coupled-resonator optical waveguides," *Physical Review E*, 66 (4): Art. No. 046610 Part 2, 2002.
- [81] J. K. S. Poon, J. Scheuer, S. Mookherjea, G. T. Paloczi, Y. Y. Huang, and A. Yariv, "Matrix analysis of microring coupled-resonator optical waveguides," *Optics Express*, 12 (1): 90-103, 2004.

- [82] A. Martinez, A. Griol, P. Sanchis, and J. Marti, "Mach-Zehnder interferometer employing coupled-resonator optical waveguides," *Optics Letters*, 28 (6): 405-407, 2003.
- [83] M. Bayindir, B. Temelkuran, and E. Ozbay, "Tight-binding description of the coupled defect modes in three dimensional photonic crystals," *Physical Review Letters*, 84 (10): 2140-2143, 2000.
- [84] J. K. S. Poon, J. Scheuer, Y. Xu and A. Yariv, "Designing coupled-resonator optical waveguide delay lines," *Journal of the Optical Society of America B*, 21 (9): 1665-1673, 2004.
- [85] Y. Xia, and G. M. Whitesides, "Soft lithography," *Angewandte Chemi - International Edition*, 37 (5): 551-575, 1998.
- [86] Y. Xia and G. M. Whitesides, "Soft lithography," *Annual Review of Materials Science*, 28: 153-184, 1998.
- [87] S. R. Quake and A. Scherer, "From micro- to nanofabrication with soft materials," *Science*, 290 (5496): 1536-1540, 2000.
- [88] X.-M. Zhao, S. P. Smith, S. J. Waldman, G. M. Whitesides, and M. Prentiss, "Demonstration of waveguide couplers fabricated using microtransfer molding," *Applied Physics Letters*, 71 (8): 1017-1019, 1997.
- [89] J. A. Rogers, M. Meier, and A. Dodabalapur, "Using printing and molding techniques to produce distributed feedback and Bragg reflector resonators for plastic lasers" *Applied Physics Letters*, 73 (13): 1766-1768, 1998.
- [90] M. Meier, A. Dodabalapur, J. A. Rogers, R. E. Slusher, A. Mekis, A. Timko, C. A. Murray, R. Ruel, and O. Nalamasu, "Emission characteristics of two-dimensional organic photonic crystal lasers fabricated by replica molding," *Journal of Applied Physics*, 86 (7): 3502-3507, 1999.
- [91] P. Yang, G. Wirnsberger, H. C. Huang, S. R. Cordero, M. D. McGehee, B. Scott, T. Deng, G. M. Whitesides, B. F. Chmelka, S. K. Buratto, and G. D.

- Stucky, "Mirrorless lasing from mesostructured waveguides patterned by soft lithography," *Science*, 287 (5452): 465-467, 2000.
- [92] B.-T. Lee, M.-S. Kwon, J.-B. Yoon, and S.-Y. Shin, "Fabrication of polymeric large-core waveguides for optical interconnects using a rubber molding process," *IEEE Photonics Technology Letters*, 12 (1): 62-64, 2000.
- [93] C. Chao, and L. J. Guo, "Polymer microring resonators fabricated by nanoimprint technique," *Journal of Vacuum Science and Technology B*, 20 (6): 2862-2866, 2002.
- [94] J. A. Rogers, M. Meier, A. Dodabalapur, E. J. Laskowski, and M. A. Capuzzo, "Distributed feedback ridge waveguide lasers fabricated by nanoscale printing and molding on nonplanar substrates," *Applied Physics Letters*, 74 (22): 3257-3259, 1999.
- [95] N. Sukanuma, A. Seki, Y. Tanaka, M. Ichikawa, T. Koyama, and Y. Taniguchi, "Organic polymer DBR laser by soft lithography," *Journal of Photopolymer Science and Technology*, 15 (2): 273-278, 2002.
- [96] D. Pisignano, M. Anni, G. Gigli, R. Cingolani, G. Barbarella, L. Favaretto, and G. Sotgiu, "Flexible organic distributed feedback structures by soft lithography," *Synthetic Metals*, 137 (1-3): 1057-1058 Part 2 Sp. Iss. SI, 2003.
- [97] M. V. Kunnavakkam, F. M. Houlihan, M. Schlax, J. A. Liddle, P. Kolodner, O. Nalamasu, and J. A. Rogers, "Low-cost, low-loss microlens arrays fabricated by soft-lithography replication process," *Applied Physics Letters*, 82 (8): 1152-1154, 2003.
- [98] H. Deng, G. H. Jin, J. Harari, J. P. Vilcot, and D. Decoster, "Investigation of 3-D semivectorial finite-difference beam propagation method for bent waveguides," *Journal of Lightwave Technology*, 16 (5): 915-922, 1998.
- [99] E. Delamarche, H. Schmid, B. Michel, and H. Biebuyck, "Stability of molded

- polydimethylsiloxane microstructures,” *Advanced Materials*, 9 (9): 741-746, 1997.
- [100] Y. S. Kim, J. Park, H. H. Lee, “Three-dimensional pattern transfer and nanolithography: modified soft molding,” *Applied Physics Letters*, 81 (6): 1011-1013, 2002.
- [101] A. Bietsch, and B. Michel, “Conformal contact and pattern stability of stamps used for soft lithography,” *Journal of Applied Physics*, 88 (7): 4310-4318, 2000.
- [102] S. M. Garner, S.-S. Lee, V. Chuyanov, A. Chen, A. Yacoubian, W. H. Steier, and L. R. Dalton, “Three-dimensional integrated optics using polymers,” *IEEE Journal of Quantum Electronics*, 35 (8): 1146-1155, 1999.
- [103] J. S. Kim, and J. J. Kim, “Stacked polymeric multimode waveguide arrays for two-dimensional optical interconnects,” *Journal of Lightwave Technology*, 22 (3): 840-844, 2004.
- [104] L.-R. Bao, X. Cheng, D. Huang, L. J. Guo, S. W. Pang, and A. F. Yee, “Nanoimprinting over topography and multilayer three-dimensional printing,” *Journal of Vacuum Science and Technology B*, 20 (6): 2881-2886, 2002.
- [105] J. Zaumseil, M. A. Meitl, J. W. P. Hsu, B. R. Acharya, K. W. Baldwin, Y.-L. Loo, and J. A. Rogers, “Three-dimensional and multilayer nanostructures formed by nanotransfer printing,” *Nano Letters*, 3 (9): 1223-1227, 2003.
- [106] W. Zhou, S. M. Kuebler, K. L. Braun, T. Yu, J. K. Cammack, C. K. Ober, J. W. Perry, and S. R. Marder, “An efficient two-photon-generated photoacid applied to positive-tone 3D microfabrication,” *Science*, 296 (5570): 1106-1109, 2002.
- [107] L. Dalton, “Nonlinear optical polymeric materials: From chromophore design to commercial applications,” *Advances in Polymer Science*, 158: 1-86 2002.

- [108] J. Luo, S. Liu, M. Haller, J.-W. Kang, T.-D. Kim, S.-H. Jang, B. Chen, N. Tucker, H. Li, H.-Z. Tang, L. R. Dalton, Y. Liao, B. H. Robinson, and A. K.-Y. Jen, *Proceedings SPIE* 5531: 36-, 2004.
- [109] F. Kajzar, K.-S. Lee, and A. K.-Y. Jen, "Polymeric materials and their orientation techniques for second-order nonlinear optics," *Advances in Polymer Science*, 161: 1-85, 2003.
- [110] C. Zhang, L. R. Dalton, M. C. Oh, H. Zhang, and W. H. Steier, "Low V- π electro-optic modulators from CLD-1: Chromophore desing and synthesis, material processing, and characterization," *Chemistry of Materials*, 13 (9): 3043-3050, 2001.
- [111] X. M. Zhao, Y. Xia, and G. M. Whitesides, "Soft lighographic methods for nano-fabrication," *Journal of Matererials Chemistry*, 7 (7): 1069-1074, 1997.
- [112] B. H. Robinson and L. R. Dalton, "Monte Carlo statistical mechanical simulations of the competition of intermolecular electrostatic and poling-field interactions in defining macroscopic electro-optic activity for organic chromophore/polymer materials," *Journal of Physical Chemistry A*, 104 (20): 4785-4795, 2000.
- [113] M. D. Feit and J. A. Fleck, Jr., "Light propagation in graded-index optical fibers," *Applied Optics*, 17 (24): 3990-3998, 1978.
- [114] M. S. Stern, "Semivectorial polarised finite difference method for optical waveguides with arbitrary index profiles," *IEE Proceedings*, 135 (1): 56-63, 1988.
- [115] K. Kawano, and T. Kitoh, **Introduction to optical waveguide analysis**. New York: Wiley, 2001.